# FIBER BRAGG GRATING-BASED MULTI-DIMENSIONAL SENSING AND THEIR APPLICATIONS USING MULTI-CORE FIBERS

**CUI JINGXIAN**

**PhD**

**The Hong Kong Polytechnic University**

**2021**

The Hong Kong Polytechnic University

Department of Electrical Engineering

# Fiber Bragg Grating-Based Multi-Dimensional Sensing and their Applications using Multi-Core Fibers

Cui Jingxian

A thesis submitted in partial fulfillment of the requirements for the degree of Doctor of Philosophy

May 2021

# CERTIFICATE OF ORIGINALITY

I hereby declare that this thesis is my own work and that, to the best of my knowledge and belief, it reproduces no material previously published or written, nor material that has been accepted for the award of any other degree or diploma, except where due acknowledgement has been made in the text.

…………                    …………….      (Signed)

…………CUI Jingxian ……………….      (Name of student)

# Abstract

The intrinsic characteristics of multi-core fibers (MCFs) comprising of several cores in a single cladding make them helpful in various applications due to spatial multiplexing capabilities, whilst making them promising candidates for the design of multi-dimensional sensors in fiber optic sensing. As a result of the development of multi-core fiber fan-out devices, it is possible to monitor individual cores inside the MCF separately. Therefore, fiber Bragg grating (FBG) based MCF is of great value which can be utilized as a two-dimensional or three-dimensional sensor, depending on the choice of a single set of gratings or an array of gratings inscribed in the fiber. This thesis focuses on inscribing FBGs in MCFs and developing them as multi-dimensional sensors suitable for various applications, such as vibration detection, inclination measurement, and displacement monitoring.

A novel orientation-sensitive two-dimensional accelerometer based on FBGs inscribed in a silica seven-core MCF was designed. Performance of the proposed accelerometer in terms of frequency, acceleration and vibration orientation were experimentally investigated. The designed two-dimensional accelerometer is capable of obtaining the vibration frequency, acceleration and orientation, simultaneously. A sensitivity which is strongly dependent on the orientation is achieved, with a best orientation accuracy of 0.127° over a range of 0-180°. In order to verify the stability of the performance, different sets of chosen outer cores were utilized to retrieve the

orientation.

An all-fiber two-dimensional inclinometer was proposed under the FBG-based MCF structure, with the capability of measuring the azimuthal angle and the inclination angle, simultaneously. The sensor performance was theoretically optimized and experimentally investigated. Excellent agreement between simulated and experimental results was achieved, with sensitivities of 3.42 and 3.41 pm/° for azimuthal and inclination angles, respectively. Through detection of the wavelength shifts of the FBGs inscribed in the central core and two outer cores of a silica seven-core MCF, a minimum error of 0.0056° for the azimuthal angle, and 0.025° for the inclination angle, were obtained. The detection range of the former ranges from 0 to 360°, while the latter ranges from 0 to 90°.

This thesis further elaborates on the development of a two-dimensional vector displacement sensor with the capability of distinguishing the direction and amplitude of the displacement simultaneously, while its performance was enhanced by machine learning algorithms. It was designed with a displacement direction range of 0-360°, and the amplitude range related to the length of the sensor body. The displacement information was obtained under a random circumstance, where the performance was investigated under the comparison of a theoretical model as well as a machine learning model. The maximum positive sensitivities are obtained as 11.47, 12.31, and 11.73 pm/mm. The validity of the theoretical model is limited to a linear range (from 0 to 9mm) whereas the sensor enhanced by machine learning model outperformed in two aspects, an enlarged measurement range (from 0 to 45mm) and a reduced measurement error of displacement. Mean absolute errors of direction and amplitude reconstruction were decreased by 60% and 98%, respectively with the help of the machine learning algorithm.

# Publications

## Journal:

1. **Jingxian Cui**, Zhengyong Liu, Dinusha Serandi Gunawardena, Zhiyong Zhao, and Hwa-Yaw Tam, “Two-dimensional vector accelerometer based on Bragg gratings inscribed in a multi-core fiber,” Optics Express 27(15), 20848-20856 (2019).
2. **Jingxian Cui**, Dinusha Serandi Gunawardena, Zhengyong Liu, Zhiyong Zhao, and Hwa-Yaw Tam, “All-Fiber Two-Dimensional Inclinometer Based on Bragg Gratings Inscribed in a Seven-Core Multi-Core Fiber,” Journal of Lightwave Technology, 38(8), 2516-2522 (2020).
3. **Jingxian Cui**, Huaijian Luo, Jianing Lu, Xin Cheng, and Hwa-Yaw Tam, "Random forest assisted vector displacement sensor based on a multicore fiber," Optics Express 29(10), 15852-15864 (2021).

## Conference paper:

1. **Jingxian Cui**, Zhengyong Liu, Dinusha Serandi Gunawardena and Hwa-Yaw Tam, “Omnidirectional vibration sensor based on fiber Bragg gratings in a seven-core fiber,” Seventh European Workshop on Optical Fibre Sensors, 111992P (2019).
2. **Jingxian Cui**, Dinusha Serandi Gunawardena, Zhengyong Liu and Hwa-Yaw Tam, “Self-Compensated Omnidirectional Tilt Sensor Using Multi-Core Fiber

Inscribed with Bragg Gratings," The 27th International Conference on Optical Fiber Sensors (2020).

# Acknowledgements

First and foremost, I would like to express my sincerest gratitude to my supervisor, Prof. Hwa-Yaw Tam, for his expertise in the fiber-optic research and application realm, and all his guidance and support throughout my Ph.D. study. It has been a great honor to be under the supervision of such an extraordinary advisor. Also, I would like to thank Prof. Chao Lu for his continuous assistance. In addition, without his kindly recommendation, I would not start my Ph.D. study in PolyU.

Furthermore, I am ever grateful to Dr. Zhengyong Liu and Dr. Dinusha Serandi Gunawardena, for all their continuous help, sharing, and collaboration that have helped me in many ways during the whole research study. My deepest gratitude to Dr. Zhiyong Zhao for his extraordinary intuition and fruitful discussion. Many thanks to our group members, Dr. Xin Cheng, Dr. Jijun He, Dr. Jitendra Narayan Dash, Dr. Lin Htein, Dr. Julien Bonefacino, Mrs. Yuk-Ting Ho, Mr. Chern Yang Leong, Mr. Linyue Lu, and Mr. On Kit Law for their kind support in the laboratory. Special thanks to Dr. Zhongwei Tan, Mr. Jianing Lu, Mr. Zhuo Wang and Mr. Huaijian Luo for their suggestions and enjoyable research life. I gratefully acknowledge all the other colleagues from the Photonics Research Center and the Department of Electrical Engineering staff.

Finally, I must express my heartfelt gratitude to my parents for their unconditional love in achieving my goals. My sincere appreciation goes to my husband, Dr. Xi Chen, for his endless love and encouragement. Their support will always be a valuable asset to me.

May 2021

# Table of Contents


**Abstract** ..... i

**Publications** ..... v

**Acknowledgements** ..... vii

**Table of Contents** ..... ix

**List of Abbreviations** ..... xi

**List of Notations** ..... xiii

**List of Figures** ..... xv

**List of Tables** ..... xx

**Chapter 1 Introduction** ..... 1

1.1 Background and Research Motivation ..... 1

1.2 Research Objectives ..... 5

1.3 Outline of the Thesis ..... 6

**Chapter 2 Background Review and Principle of Fiber Bragg Gratings (FBGs) in Multi-Core Fibers (MCFs)** ..... 9

2.1 Multi-Dimensional Fiber-Optic Sensors ..... 9

2.2 MCF-based Fiber-Optic Sensors ..... 14

2.3 FBG Inscription Technology and Characterization ..... 23

2.4 FBG Inscription in MCFs ..... 32

2.4.1 Characteristics of MCF-based FBGs ..... 33

2.4.2 Lensing Effect ..... 40

2.4.3 Shadowing Effect ..... 40

2.4.4 Uniformity of Cores in MCF ..... 41

2.5 FBG-based MCFs for Multi-Dimensional Sensing ..... 42

2.5.1 Two-Dimensional Vector Sensing ..... 42

2.5.2 Three-Dimensional Shape Sensing ..... 46

2.6 Summary ..... 52

**Chapter 3 Two-Dimensional Accelerometer** ..... 53

3.1 Overview on Fiber-Optic Accelerometers ..... 53

3.2 Principle of the Two-Dimensional Accelerometer ....................................56

3.3 Characterization of the Two-Dimensional Accelerometer ............................60

3.4 Orientation Discrimination ....................................................................65

3.5 Summary ...........................................................................................69

**Chapter 4 Two-Dimensional Inclinometer ......................................................71**

4.1 Overview on Fiber-Optic Inclinometers .....................................................71

4.2 Principle of the Two-Dimensional Inclinometer ..........................................73

4.3 Theoretical Model of the Two-Dimensional Inclinometer ...........................77

4.4 Characterization of the Two-Dimensional Inclinometer ..............................81

4.5 Orientation Discrimination ....................................................................85

4.6 Summary ...........................................................................................90

**Chapter 5 Two-Dimensional Displacement Sensor Assisted with Machine Learning Algorithms ........................................................................................92**

5.1 Overview on Displacement Sensors ...........................................................92

5.2 Machine Learning in Fiber-Optic Sensors ..................................................94

5.3 Theoretical Model of the Two-Dimensional Displacement Sensor ..............96

5.4 Two-Dimensional Displacement Sensor under Random Forest ..................103

5.4.1 Principle of Random Forest Regression ..............................................103

5.4.2 Random Forest-based Displacement Sensor .......................................105

5.5 Experiment Setup of the Two-Dimensional Displacement Sensor .............107

5.6 Displacement Reconstruction ...............................................................111

5.6.1 Theoretical Model .............................................................................111

5.6.2 Random Forest Model .......................................................................116

5.7 Summary ..........................................................................................119

**Chapter 6 Conclusion and Future Work ........................................................121**

6.1 Conclusion .......................................................................................121

6.2 Future Work .....................................................................................123

**Reference ..........................................................................................125**

# List of Abbreviations

**A**

| | |
|---|---|
| ANN | Artificial neural network |
| AWG | Arrayed waveguide grating |

**B**

| | |
|---|---|
| BGS | Brillouin gain spectrum |
| BOTDR | Brillouin optical time domain reflectometry |
| B | Boron |

**C**

| | |
|---|---|
| CFBG | Chirped fiber Bragg grating |
| CNN | Convolutional neural network |

**D**

| | |
|---|---|
| DCF | Depressed-cladding fiber |

**F**

| | |
|---|---|
| FBG | Fiber Bragg grating |
| FPI | Fabry-Pérot interferometer |
| F | Fluorine |
| FFT | Fast Fourier transform |

**G**

| | |
|---|---|
| Ge | Germanium |
| GPR | Gaussian process regression |

**L**

| | |
|---|---|
| LPG | Long-period grating |
| LCF | Lorentzian curve fitting |
| LP | Linearly polarized |

**M**

| | |
|---|---|
| MZI | Mach-Zehnder interferometer |
| MCF | Multi-core fiber |
| MMF | Multimode fiber |
| MI | Michelson interferometer |

| | |
|---|---|
| MAE | Mean absolute error |

**N**

| | |
|---|---|
| N | Nitrogen |

**O**

| | |
|---|---|
| OFDR | Optical frequency domain reflectometry |
| OTDR | Optical time domain reflectometry |
| OOB | Out-of-bag |

**P**

| | |
|---|---|
| PCF | Photonic crystal fiber |
| PMF | Polarization maintaining fiber |
| POF | Polymer optical fiber |
| PSFBG | Phase-shifted fiber Bragg grating |
| PCA | Principal component analysis |
| Pb | Lead |

**R**

| | |
|---|---|
| RI | Refractive index |
| RMSE | Root mean squared errors |

**S**

| | |
|---|---|
| SMF | Single mode fiber |
| SI | Sagnac interferometer |
| SDM | Space division multiplexing |
| SEM | Scanning electron microscopic |
| SVM | Support vector machine |

**T**

| | |
|---|---|
| TFBG | Tilted fiber Bragg grating |
| Ti | Titanium |

**U**

| | |
|---|---|
| UV | Ultraviolet |

# List of Notations

| | |
|---|---|
| $n_0$ | refractive index of the fiber core |
| $\Lambda$ | grating period |
| $\Delta n(z)$ | index change spatially averaged over a grating period |
| $n_{eff}$ | effective refractive index |
| $\lambda_B$ | Bragg wavelength |
| $p_e$ | effective photo-elastic coefficient |
| $\Delta T$ | temperature variation at the specific FBG |
| $I(y,z)$ | laser intensity |
| $f(y,z)$ | shaping function for the profile of the interference pattern |
| $w_0$ | waist of the laser beam |
| $d_0$ | diameter of the core |
| $D$ | diameter of the cladding |
| $d$ | pitch between two adjacent cores |
| $\Delta\lambda$ | Bragg wavelength shift |
| $\lambda_i$ | Bragg wavelength in each core $i$ |
| $\varepsilon_i$ | strain applied on each core $i$ |
| $R$ | strain-induced bending radius |
| $T(s)$ | tangent unit vector |
| $N(s)$ | normal unit vector |
| $B(s)$ | binormal unit vector |
| $\kappa(s)$ | curvature function |
| $\tau(s)$ | torsion function |
| $K(s)$ | vector sum of the curvature vectors |
| $\theta_i$ | angular position of core $i$ |
| $\theta_v$ | vibration orientation |

| | |
|---|---|
| $L$ | free-fiber length |
| $a$ | acceleration value |
| $f$ | vibration frequency |
| $D_i$ | distance from the core of interest to the neutral plane |
| $\varphi$ | azimuthal angle |
| $\theta$ | inclination angle |
| $R_{Mass}$ | mass-induced bending radius |
| $R_{Fiber}$ | free-fiber-induced bending radius |
| $E$ | Young's modulus of the fiber |
| $I$ | second moment of the cross-sectional area |
| $x_g$ | distance between the grating and the fixed point |
| $w$ | fiber weight per unit length |
| $m$ | weight of the applied mass |
| $\delta$ | displacement applied on the free-fiber end |
| $\theta_D$ | displacement angle |
| $M(x)$ | bending moment at a specific position of the free-fiber |
| $F$ | applied force at the free fiber end. |
| $R^2$ | coefficient of determination (score) |

# List of Figures


Figure 1.1. Schematic figure of operation principles for fiber-optic sensors......... 3

Figure 2.1. Cross-sectional images of reported MCFs with different number of cores and fiber structures. ............................................................................ 16

Figure 2.2. Talbot interferometer technique for FBG inscription. ....................... 26

Figure 2.3. Phase mask technique for FBG inscription. ...................................... 28

Figure 2.4. Point-by-point technique for FBG inscription.................................. 29

Figure 2.5. Reflection and transmission spectra of an FBG. ............................... 29

Figure 2.6. Schematic figure of using UV exposure to inscribe FBGs in MCF... 33

Figure 2.7. SEM image of the homogeneous seven-core MCF. .......................... 34

Figure 2.8. Reflection spectra of the FBGs inscribed in seven-core MCF using 193 nm laser. ............................................................................................ 35

Figure 2.9. Reflection spectra of the FBGs inscribed in seven-core MCF using 248 nm laser. ............................................................................................ 37

Figure 2.10. Reflection spectra of the FBGs inscribed in seven-core MCF using 213 nm laser. ............................................................................................ 38

Figure 2.11. Reflection spectra of the FBG array inscribed in the seven-core MCF. ................................................................................................................ 39

Figure 2.12. Refractive index difference of individual cores in MCF. ................ 42

Figure 2.13. Schematic of the cross-section for a seven-core MCF..................... 43

Figure 2.14. Schematic figure of the FBG-based MCF under bending. .............. 44

Figure 2.15. The schematic figure of a three-dimensional shape sensor based on an MCF-based FBG array. ............................................................................ 47

Figure 3.1. Cross-section of the fiber cores with the defined geometrical parameters. ............................................................................................ 57

Figure 3.2. Reflection spectra of the FBGs written in core 1, 2, 4 and 6. ............58

Figure 3.3. (a) Definition of distance $D$ from the core of interest to the neutral plane and (b) detailed illustration of the free-fiber with length $L$; (c) schematic setup for the vibration test of the two-dimensional vibration sensor. ........................................................................................................60

Figure 3.4. (a) Real-time wavelength shifts of FBGs in core 1, 2, 4 and 6 with the following values: $L$ = 45.5 mm, $f$ = 40 Hz, $\theta_v$ = 90° and $a$ = 10 g. The corresponding (b) FFT spectrum with $a$ = 10 g, and (c) wavelength shifts versus applied acceleration with values from 0 g to 10 g............................61

Figure 3.5. (a) Real-time wavelength shifts of FBGs in core 1, 2, 4 and 6 with the following values: $L$ = 66 mm, $f$ = 20 Hz, $\theta_v$ = 90° and $a$ = 10 g. The corresponding (b) FFT spectrum with $a$ = 10 g, and (c) wavelength shifts versus applied acceleration with values from 1 g to 10 g............................62

Figure 3.6. Sensitivity-frequency responses of the FBG in core 2 when $\theta_v$ = 90°, $L$ = 66, 45.5 and 25 mm with or without a glue mass. Inset shows the theoretical resonance frequencies under different fiber lengths. .................64

Figure 3.7. Orientation dependence of the sensitivities of FBGs in core 1, 2, 4 and 6 under different conditions. (a) $L$ = 66 mm and $f$ = 20 Hz; (b) $L$ = 45.5 mm and $f$ = 40 Hz. .........................................................................................66

Figure 3.8. Input and measured orientation values under specific orientations from 0 to 180° when $L$ = 45.5 mm and $f$ = 30 Hz. Inset shows the corresponding accuracy ranges...................................................................68

Figure 3.9. (a) Orientation accuracy under different combinations of outer cores when fiber length $L$ = 66 mm. (b) Measured orientations applied with different accelerations when $\theta_v$ = 20° under different combinations of outer cores.........................................................................................................69

Figure 4.1. (a) Definition of the geometrical parameters from the cross-section of the MCF and (b) reflection spectra of the FBGs inscribed in fiber cores. ...74

Figure 4.2. Schematic illustration of the inclinometer under different inclinations. (a) $\varphi$ = 0° and $\theta$ = 0°, (b) $\varphi$ = 0° and $\theta$ = 20°, and (c) $\varphi$ = 0° and $\theta$ = 60°....75

Figure 4.3. Simulation results of wavelength shift versus $\varphi$ for (a) core 2 and (b) core 4 with $\theta$ over a range from 0 to 90° in steps of 10°. ............................ 78

Figure 4.4. Simulation results of wavelength shift versus $\theta$ for (a) core 2 and (b) core 4 with $\varphi$ over a range from 0 to 330° in steps of 30°. .......................... 79

Figure 4.5. Simulation results of wavelength shift versus $\varphi$ with $\theta$ fixed at 60° under varying conditions of (a) pitch $d$, (b) Young's modulus $E$, and (c) weight of mass $m$. (d) Wavelength shift comparison among three parameters. ........................................................................................................ 81

Figure 4.6. (a) Illustration of the tilt sensor, including a fiber rotator and a 6-axis kinematic mount introducing $\varphi$ and $\theta$ respectively, to the MCF inscribed with FBGs. (b) Schematic setup of the two-dimensional inclinometer system used for the tilt measurement. .................................................................... 82

Figure 4.7. Raw data of the Bragg wavelength shifts in (a) core 2, (b) core 4, and (c) core 6, and self-compensated data of the Bragg wavelength shifts in (d) core 2, (e) core 4, and (f) core 6, with $\varphi$ varying from 0 to 360° in steps of 10°, and $\theta$ varying from 0 to 90° in steps of 10°. ....................................... 83

Figure 4.8. Compensated experimental results of wavelength shift versus $\theta$ for (a) core 2 and (b) core 4 with $\varphi$ in the range from 0 to 330° in steps of 30°. .... 85

Figure 4.9. Input and measured azimuthal angles at specific orientations from 0 to 360° with the use of wavelength shifts in core 2 and 4. .......................... 86

Figure 4.10. Orientation error of azimuthal angle over the range from 0-360°, under three different combinations of the used fiber core, including (a) core 2 and 4, (b) core 2 and 6, and (c) core 4 and 6. ........................................... 87

Figure 4.11. Orientation error of inclination angle over the range from 10-90°, under three different combinations of the used fiber core, including (a) core 2 and 4, (b) core 2 and 6, and (c) core 4 and 6. .......................................... 89

Figure 5.1. (a) Geometrical definition of parameters based on the cross-section of the MCF. (b) Schematic structure demonstration of the FBG and MCF in the displacement sensor design, with the FBGs inscribed in MCF shown in the expanded view. ......................................................................................... 97

Figure 5.2. Simulation results of wavelength shift versus displacement direction varying from 0 to 360° in steps of 10° for (a) core 3 and (b) core 5, with displacement amplitude fixed at 0, 3, 6, and 9 mm. ..................................100

Figure 5.3. Simulation results of wavelength shift versus displacement amplitude changing from 0 to 9 mm in steps of 1 mm for (a) core 3 and (b) core 5, with displacement direction varying from 0 to 330° in steps of 30°. .........102

Figure 5.4. Simulation results of displacement sensitivity as a function of different free fiber length. Inset shows the displacement sensitivity response with respect to the position of FBG along the fiber length. .......................103

Figure 5.5. Flow chart of random forest algorithm in displacement sensor. ......106

Figure 5.6. Schematic experimental setup for the two-dimensional vector displacement sensor. ........................................................................108

Figure 5.7. Experimental results of wavelength shift versus displacement direction in the two-dimensional range in (a) core 3 and (b) core 5 with displacement amplitude changing from 0 to 9 mm in steps of 1 mm.........109

Figure 5.8. Experimental results of wavelength shift versus displacement amplitude in linear range of (a) core 3, (b) core 5, (c) core 7, and wavelength response of (d) core 3 in full range. The displacement direction varies from 0 to 330° in steps of 30°, with the dots indicating the experimental results while the lines in (a)-(c) representing the fitting ones, and (d) representing the connecting curves. ....................................................................110

Figure 5.9. Experimental results of sensitivity-direction response in core 3, 5 and 7, with displacement direction changing from 0 to 360° in steps of 10°.... 111

Figure 5.10. Absolute errors of displacement direction based on different combinations of the outer cores using theoretical model, with the direction and displacement ranges of 0-360° and 1-9 mm, respectively. ..................113

Figure 5.11. Absolute errors of displacement amplitude based on different combinations of the outer cores using theoretical model, with the direction and displacement ranges of 0-360° and 1-9 mm, respectively. ..................115

Figure 5.12. Absolute errors of displacement (a) direction and (b) amplitude

using random forest, with the direction and displacement ranges of 0-360° and 1-45 mm, respectively. ........................................................................ 117

Figure 5.13. Procedure of 5-fold cross-validation. ............................................ 118

# List of Tables

Table 5.1. Results of 5-fold cross-validation ....................................................... 118

Table 5.2. Comparison between reconstructed results using two models .......... 119

# Chapter 1 Introduction

## 1.1 Background and Research Motivation

Multi-dimensional (Vector) detection is essential in industrial applications, such as in petroleum industry, seismic exploration, robotic arms and structural health monitoring [1-4], where sensing technology is an effective method to determine the information of both direction and amplitude. Traditional electrical sensors have several disadvantages, such as large transmission loss, poor multiplexing capability, and are easily susceptible to external electromagnetic fields, making them inconvenient to be applied in strong radiation and high electromagnetic interference environments, which extremely limit their applications. However, the fiber-optic sensors can be an excellent candidate under these special environments. Optical fiber sensing technology is an increasingly popular sensing technology developed in the late 1970s. It has made great progress over the past few decades due to their intrinsic properties, including small and compact size, light weight, immunity of electromagnetic interference, corrosion resistance, and long-term stability. Commonly, fiber-optic sensors are designed based on fiber interferometry, fiber Bragg gratings and fiber backscattering. Optical fiber interferometers have a variety of structures, providing the possibility for measurement of numerous parameters. Usually, fiber interferometers are of high sensitivity. For fiber grating sensors, they have a stable response to strain and temperature, suitable for point-based or quasi-distributed optical sensing systems. In addition, fiber backscattering enables high spatial resolution and high sensitivity, which is applied in long distance distributed optical sensing systems.

There are two major issues in the development process of the fiber-optic sensors, one is the higher sensitivity or resolution, and the other is the sensor miniaturization or integration. Basically, optical sensing can be considered as the detection of different physical properties of the optical field. Therefore, according to the operating principle, fiber-optic sensors are able to detect the phase, intensity, wavelength, frequency and polarization. During the sensing process, all these parameters are needed to be monitored as the optical fiber is subjected to external perturbations. For example, most of the phase modulated sensors have interferometric structure and through phase detection before and after the sensor, they are supposed to achieve monitoring of physical parameters. For the intensity modulated sensors, they operate based on the detection of optical power difference before and after the measurement. When it comes to the wavelength modulated sensors, we are mainly referring to the fiber grating sensors, where wavelength shift is used for detection. Also, for the frequency modulated sensors, the fiber backscattering is majorly concerned, where frequency is the parameter used for sensing. Finally, for polarization modulated sensors, variation in the polarization state is demodulated for operation. Schematic figure of the operation principle for the fiber-optic sensors is shown in Figure 1.1. Therefore, through detection of the changes of these parameters, external perturbations can be analyzed.

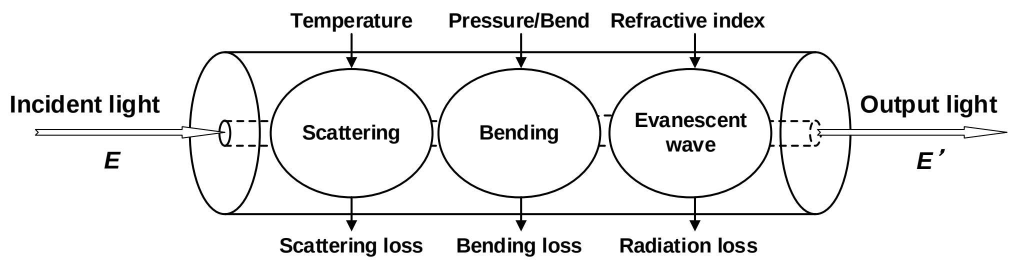


Figure 1.1. Schematic figure of operation principles for fiber-optic sensors.

Although, there are different kinds of fiber-optic sensors, some of them are inconvenient to be integrated as a multi-dimensional or a multi-parameter sensor, due to the complexity of multiplexing [5-7], such as fiber interferometers, which limit the capability of time and spatial multiplexing. Since the late 1970s, Hill et al. first demonstrated the photosensitivity of the optical fiber and periodically changed the refractive index along the fiber core [8], fiber Bragg grating (FBG) has been commonly applied in optical communication as fiber laser, filter, dispersion compensator, as well as in the optical sensing industry. Due to the Bragg wavelength dependency on the external perturbation, FBGs are effectively applied for the environment variation detection. Meanwhile, they are possible to be wavelength division multiplexed through the integration of several FBGs for multi-parameter sensing. However, for the conventional FBG in the commercial single mode fiber (SMF), the grating structure is located in the fiber core, which is the center of a cylindrical waveguide, causing directional insensitivity. Additionally, the guided mode is confined in the fiber core, which is insensitive when implementing multi-dimensional measurements. Recently, a number of methods, including specialty fibers and different grating structures have been introduced to grating-based multi-dimensional sensing. However, there still remains the problem of cross-sensitivity, such as temperature. Noticeably, most of the multi-dimensional sensors are developed only to be directional sensitive, instead of obtaining the actual directional information. From this point of view, the multi-core fiber (MCF) together with the fan-in/out, a commercially available device, are great candidates to solve these complications. The spatial diversity inherent to MCFs due to the presence of several individual cores in a single cladding makes it helpful to achieve multi-dimensional sensing, together with performance improvement of the existing sensors.

In this thesis, the study of inscribing FBGs in MCFs and applying them to different multi-dimensional sensing applications are presented. The FBG-based MCF sensors are used to detect two-dimensional sensing characteristics. Through investigation of the theoretical models and conduction of the experiments, the sensors are applied in the measurements of acceleration, inclination and displacement. In the aspect of signal reconstruction, direction and other physical parameters are retrieved based on the theoretical models and machine learning models. The proposed sensors can reconstruct the original signals under unknown scenarios, without the cross-sensitivity of other physical parameters such as temperature, refractive index etc., representing their potential applicability in multi-dimensional sensing applications.

## 1.2 Research Objectives

Research objectives of this study are summarized as follows:

- To develop and characterize a two-dimensional vibration sensor using an FBG-based seven-core MCF, with simultaneous determination of the vibration orientation, frequency and acceleration in a single measurement, when the source of vibration is unknown.
- To study and demonstrate an all-fiber two-dimensional inclination sensor based on FBGs in an MCF, with the capability of measuring two directional angles, including the azimuthal angle and the inclination angle, simultaneously with the utilization of a mechanical model to theoretically and experimentally investigate the performance of the sensor, through simulations of the MCF-based inclination sensor and the optimization of the sensing parameters using experimental approaches.
- To investigate and analyze a two-dimensional displacement sensor with the capability of distinguishing both the direction and amplitude of the displacement, through proposition of a theoretical model to develop the displacement sensor and implementation of the theoretical model and a random forest model, one of the machine learning algorithms, to help during the retrieval process. And to compare the retrieval performance under these two models, in terms of the

displacement direction and amplitude.

## 1.3 Outline of the Thesis

The research contributions of this thesis contain 6 chapters.

Chapter 1 gives an introduction to the thesis, including a brief overview on the fiber-optic sensors, motivation for carrying out multi-dimensional sensing investigations, research objectives and outline of the thesis.

Chapter 2 reviews the background of the fiber-optic multi-dimensional sensors, together with the MCF-based fiber-optic sensors. Previous research of the related sensors are concluded. Emphasis is put on the MCF-based FBG. A brief introduction on different FBG inscription technology is provided, with highlighting the results and characteristic of the MCF-based FBGs. Theories of MCF-based FBGs to be applied for both two-dimensional and three-dimensional sensing applications are investigated as well.

Chapter 3 describes the application of MCF in the two-dimensional vibration sensing area. Previous research on both one-dimensional and two-dimensional vibration sensors are investigated and summarized. An orientation-sensitive two-dimensional vibration sensor based on the FBG inscribed in the seven-core MCF is proposed. Detailed performance in terms of length of the sensor body, frequency, acceleration and vibration orientation are investigated, with information on vibration orientation as well as acceleration are obtained simultaneously within a single measurement. Orientation sensitivity, together with the vibration performance reconstructed under various scenarios is analyzed as well.

Chapter 4 is a discussion on an all-fiber two-dimensional inclination sensor based on MCF-based FBGs. A brief introduction on earlier related research of fiber-optic inclination sensors is firstly presented. Then, the theoretical model of the MCF-based inclination sensor is investigated, through the simulation of the MCF-based inclinometer and the optimization of the sensing parameters. Conduction of the experiment and the experimental results are illustrated, while an excellent agreement is shown between the experimental results and the simulated ones. Sensing capability of retrieving the two directional angles including the azimuthal angle and the inclination angle, simultaneously is investigated when the inclination source is unknown.

Chapter 5 presents a two-dimensional displacement sensor, with the sensing performance assisted by random forest, a powerful machine learning algorithm. A short overview on multi-dimensional displacement sensor is introduced, as well as the application of machine learning algorithms on fiber-optic sensors. Theoretical model of the proposed two-dimensional displacement sensor is studied, through the simulation and optimization of the sensing performance. The introduction of random forest algorithm and its application on the displacement sensor are provided. Experiment is conducted, with retrieval of results for the direction and amplitude of the displacement under random circumstances. A comparison between the displacement reconstruction of two models is analyzed as well.

Chapter 6 summarizes the thesis with highlights of the current research results and possible suggestions for the following work in terms of grating fabrication technologies, grating categories, potential sensing applications and machine learning-based retrieval methods.

# Chapter 2 Background Review and Principle of Fiber Bragg Gratings (FBGs) in Multi-Core Fibers (MCFs)

## 2.1 Multi-Dimensional Fiber-Optic Sensors

Multi-dimensional sensors (vector sensors) are desirable in many structural applications, where more than one axis of information at a single point can be measured. A multi-dimensional sensor enables simultaneous measurement for direction and amplitude, which can accordingly reconstruct the original signal. In general, multi-dimensional sensing involves two major parts, including the strain measurement along the axial direction and the bending-induced measurement in the radial direction. The sensing performance is usually achieved based on an asymmetric structure in the fiber. Due to diverse responses in different directions, directional sensing is performed.

There are many multi-dimensional sensors designed to measure various parameters, such as curvature, magnetic field, vibration [9-11], etc. Commonly, most of the multi-dimensional sensors are designed based on interferometric structure due to their advantages of high sensitivity and easy configuration. According to the working principles, four types of interferometric sensors exist, namely Fabry-Pérot interferometer (FPI), Mach-Zehnder interferometer (MZI), Michelson interferometer (MI), and Sagnac interferometer (SI). The sensors use the interference between two beams that propagate through different optical paths of a single fiber or two different fibers, with one of the paths easily affected by external perturbations [12]. Therefore, sensing indicators including phase, intensity, bandwidth, etc. are sensitive to the environmental change, bringing remarkable performance to the sensor. Additionally, when specific configurations are introduced to interferometers, such as offset splicing and asymmetric structures, the sensors are supposed to be directional sensitive.

For example, in 2012, Zhang et al. proposed an MZI based on up-taper and lateral-offset splicing for curvature measurement, where interference happened between the core and cladding modes. The interference pattern's red and blue shifts indicated the directional sensitivity in a pair of opposite directions, with a maximum bending sensitivity of 11.987 $nm/m^{-1}$ [13]. In 2015, they introduced another MZI for vector curvature sensor through cascading two hump-shaped tapers. It was achieved by offset splicing two single mode fibers (SMFs), which broke the symmetric structure and brought the directional sensitivity in two directions. Except for the SMF, specialty fibers such as photonic crystal fiber (PCF) were also utilized for multi-dimensional sensing [14]. It was obtained based on PCF and SMF interrogation, with small voids of the PCF collapsed. The propagating beam diffracted in the collapsed zone, resulting in the excitation of different PCF modes, where the interference occurred. The refractive index along the fiber core was changed during bending, causing the interferometer sensitive along a specific direction. In addition to offset-splicing, tapering, and specialty fibers, researchers fabricate microstructures inside the fiber for the design of multi-dimensional sensors. For instance, an offset hollow ellipsoid was fabricated in SMF with the usage of the femtosecond laser micromachining and fusion splicing techniques [15]. Due to the asymmetric position of the elliptical hole, the fabricated MZI was enabled for bending measurement in two principal axes of the hole. Chen et al. also applied the femtosecond laser to off-axially modify the refractive index in an SMF core [16]. The fundamental mode in SMF excited a new fundamental and a higher-order mode in the modified zone, where the interference happened. Wavelength and intensity of the interference pattern were monitored in the MZI for curvature detection, bringing a direction response in two orthogonal axes. In 2019, Li et al. sandwiched a side polished no core fiber between two SMFs to measure the magnetic fluid [17]. The side polished fiber brought the axially asymmetry in the sensor structure, which helped achieve the magnetic fluid sensing in different directions. Apart from the popular MZI, there are other structures such as FPI designed for multi-dimensional sensing. In 2016, Liu et al. used four silicon FPIs to build a vector flow sensor, with one situated in the center and the other three equally arranged around [18]. Through the temperature distribution on different FPIs, the direction of the flow was detected. Although interferometers bring a lot of advantages when designing multi-dimensional sensors, a number of limitations still remain. The most frequent drawback is the cross-sensitivity. Interferometers may be responsive to other physical parameter, when monitoring the target parameter such as temperature. Besides, the configuration is usually fragile, and has weak mechanical strength and long-term durability. The interferometer's performance could be influenced during long time measurement. Additionally is the insertion loss. The sensor's structure is sometimes highly complex, and a high insertion loss is possible to be introduced during the fabrication process, i.e., offset splicing, tapering, side polishing etc. The complexities in multiplexing can be considered as another challenge. Due to the difference between modulation and demodulation process, it is inconvenient to apply them in long-distance sensing scenarios.

On the other hand, a grating-based fiber-optic sensor is more suitable to be incorporated as multi-dimensional sensors, owing to their advantages of easy fabrication, low loss and multiplexing capabilities. In 2000, Udd et al. proposed inscribing FBGs in the birefringent fiber, such as polarization maintaining fiber (PMF) [19]. Two gratings dependent on the effective refractive index of the guided modes in PMF were obtained, resulting the sensor being responsive along the polarization axes. Strain responses in both the axial and transverse directions were investigated. Other fibers, such as D-shaped fiber, polymer optical fiber (POF), multimode fiber (MMF), depressed-cladding fiber (DCF) [9, 20-22], etc. were also demonstrated for FBG-based multi-dimensional sensors. Zhu et al. fabricated the Bragg grating off the fiber center based on the femtosecond laser and near-field phase mask method [9]. Since FBGs in different modes were activated, they experienced a uniform wavelength shift under the thermal effect, whilst the bending responses were different. Owing to the off-center position of the FBGs, they showed the directional sensing capability in two orthogonal directions. In 2009, Chen et al. inscribed FBG in an off-centered core of the POF for curvature sensing [21]. Wavelength response was investigated in two orthogonal directions, with a higher sensitivity than the silica fiber. In 2018, Bao et al. used femtosecond laser together with the phase mask method to inscribe an FBG in a DCF for three-dimensional displacement measurement [22]. Due to the special profile of the DCF, consisting of a dip in the fiber core and a depressed layer in the cladding, the grating inscribed in the entire core region generated a fundamental core mode and several high-order modes. Sensing performance including the two-dimensional radial bending and one-dimensional longitudinal strain were investigated, from which the three-dimensional displacement was reconstructed. In addition to normal FBGs, other gratings such as tilted fiber Bragg grating (TFBG) and long-period grating (LPG) have also been proposed for multi-dimensional sensing [10, 23-25]. In 2012, Guo et al. inscribed a TFBG in an MMF, and spliced it with an SMF [23]. Because of the polarization orientation sensitivity of the asymmetric linearly polarized (LP) modes during vibration, the sensor was proposed as a vector vibroscope. In 2013, Lin et al. immersed a TFBG in magnetic fluid to achieve a two-dimensional magnetic field sensor [10]. While for the LPG, Wang et al. utilized a high-frequency $CO_2$ laser to inscribe an LPG array in an SMF [26]. The side incident $CO_2$ laser pulse caused an asymmetric index modulation in the LPFG, made the sensor sensitive in a 360° range. In 2015, Feng et al. inscribed two orthogonal TFBGs in the SMF for three-dimensional sensing [27]. The coupling of cladding modes in each TFBG was different under bending condition, while the core modes in two gratings performed similarly under axial strain. Through the combination of two-dimensional bending and one-dimensional strain response, three-dimensional sensing was achieved. There are also researchers writing uniform FBGs in the off-center region. In 2016, Feng et al. used ultraviolet (UV) irradiation to inscribe FBGs in the off-axis portion of the core, causing a similar resonance to the TFBG [28]. Amplitude of the cladding mode resonance varied under bending in different directions, while wavelength response was investigated for temperature calibration. As a result, bending measurement in a two-dimensional range was achieved with thermal insensitivity. Although various methods, including specialty fibers and different grating structures are introduced to the grating-based multi-dimensional sensing, there still remains the issue of cross-sensitivity of temperature. Another inevitable complication is, for most of the exiting multi-dimensional sensors, they are only demonstrated to be direction sensitive in two orthogonal directions while the actual direction during the measurement still remains unknown.

## 2.2 MCF-based Fiber-Optic Sensors

It is worth mentioning that in conventional SMF, the area of the fiber core accounts for less than one percent of the cross-sectional area of the fiber, meaning the spatial dimension of the fiber waveguide is not fully utilized. Over the past decade, multi-core fiber (MCF) based space division multiplexing (SDM) technology has been intensively studied in the field of high-capacity optical communication [29] and has been considered as one of the most competitive methods in the next generation communication system for capacity expansion [30]. Meanwhile, in the optical sensing area, due to the limitation of the simple structure of the SMF, it is inconvenient to implement the multi-dimensional measurement and multi-functional signal processing. There are two reasons that limit the conventional FBG sensors for multi-dimensional measurement. One is that the grating structure usually being located symmetrically in the fiber core, which is in the central region of the cylindrical waveguide, causing directional insensitivity. Another is the confinement of guided modes in the fiber core, making it insensitive to bending. However, the inherent spatial diversity of having several individual cores in a single fiber provided by MCF makes it possible for the implementation of the multi-dimensional and multi-parameter sensing, together with the performance improvement of existing sensors. Here, the multi-dimensional is defined in a spatial aspect, including two-dimensional and three-dimensional. Specifically, different cores in a single MCF perform individually, which can be considered as individual channels during measurement. Hence, through detecting the information transmitted in the different cores of the MCF, multi-dimensional sensing can be achieved.

Obviously, MCF represents an optical fiber consisted of several cores inside one fiber cladding. Figure 2.1 represents a few cross-section images of the reported MCFs with different number of cores and fiber structures [31-38]. The introduction of MCF into the optical sensing industry makes it possible for the SDM technology to be applied in fiber-optic sensors. Common choices of MCFs are twin-core, three-core, four-core and seven-core fiber.

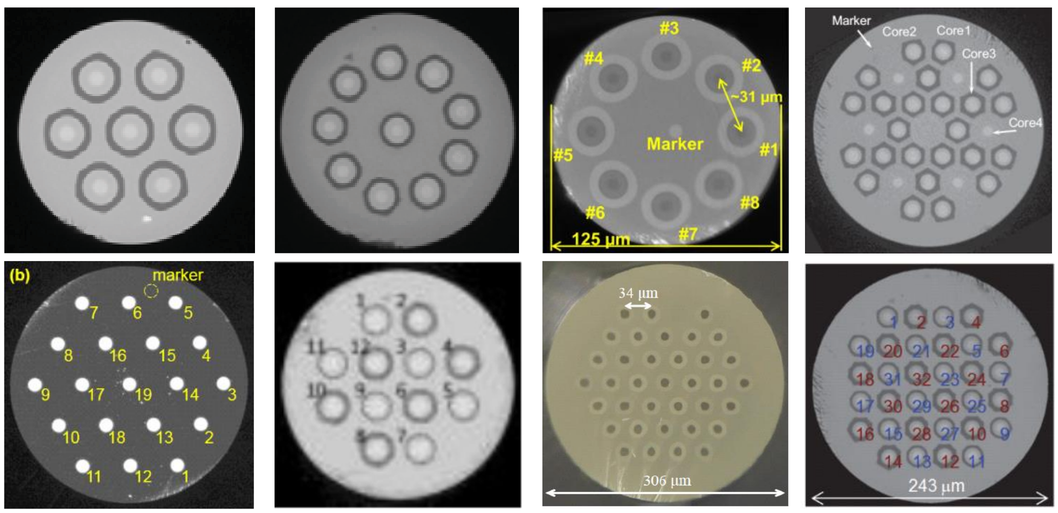


Figure 2.1. Cross-sectional images of reported MCFs with different number of cores and fiber structures.

Normally, there are two categories of the MCF-based fiber-optic sensors, including MCF-based mode interferometric sensor and MCF-based FBG sensor. These MCF-based sensors are mostly used for the implementation of strain sensing, or the improved measurements of the stain-induced bend, curvature, acceleration, etc. Also, some of them have reported applications of MCF-based temperature, force and refractive index measurements. Except for these point based sensing technologies, MCF-based distributed sensing has also raised research interest.

In 2006, Yuan et al. reported an in-fiber MI using the twin-core fiber, based on the detection of the variation of the output laser intensity. Due to the bending-induced phase difference between the two arms of the MI, the sensor was designed to be of bending sensitivity. However, the actual bending direction was not able to be confirmed. Furthermore, they also proposed a flow velocity sensor [39] and an accelerometer [40] based on the twin-core fiber MI. The cantilever-based flow velocity sensor was sensitive to the flow-induced strain, causing a phase difference in two cores of the twin-core fiber. However, due to the periodic output of the signal, the linear dynamic range was limited. Additionally, Peng et al. fabricated an accelerometer using MI, with the measurement of the phase difference for the definition of the acceleration. The limitation was that it needed another accelerometer for calibration during the mounting process. In 2011, Zhou et al. reported a refractive index sensor using the MI structure based on a different twin-core fiber, where the symmetric twin-core fiber was changed to an asymmetric one, with one of them located in the center of the fiber and the other located with an offset [41]. Through chemical etching of the cladding, the side core was exposed, causing the effective refractive index of the fundamental mode in the side core sensitive to the variation of the environmental refractive index. In 2020, Chu et al. from the same research group used the symmetric twin-core fiber as a phase shifter by side polishing one of the two cores and coating with graphene [42]. Due to the photothermal effect produced by the laser, the refractive index was influenced under the ohmic heating of the graphene, causing a phase shift in the MI. Twin-core fiber was also used for the biomedical sensing. In 2019, Tan et al. used a twin-core fiber based MZI for respiration and heartbeat measurements [43]. Through sandwiching the twin-core fiber in between two SMFs, mode coupling between two adjacent cores was obtained for vital signs signal detection.

Apart from research on the twin-core fiber, interferometer was also proposed with other kinds of fibers. There is research on the three-core fiber. In 2015, Newkirk et al. proposed a bending sensor based on the combination of the strongly coupled three-core fiber with the mode selective photonic lantern [44]. The bending was directional sensitive through measuring the variation of the energy of different output modes. After that, Villatoro et al. used the same fiber for a curvature sensor based on the reflection super-modes excited in the three-core fiber [45]. Through the measurement of the wavelength shift of the interference pattern, the sensor was found to be sensitive in different directions. Concerning the research on the four-core fiber, Li et al. spliced a segment of the fiber between two SMFs and designed the interference fringe to be sensitive to the variation of curvature, temperature and refractive index [46]. At the same time, they demonstrated a fiber ring cavity laser using the similar structure, through detecting the wavelength of the fiber laser, strain, refractive index and curvature were monitored [47].

Furthermore, researchers have also paid their attention on the seven-core fiber. Zhao et al. reported a multipath MZI based on the usage of the weakly coupled seven-core fiber for the temperature sensing while it was kept stain insensitive [48]. The sensor was designed under the configuration of a MCF off-center spliced with two segments of SMF. The multipath interference made the sensor to be more sensitive compared with a two-path interference. Similarly, Duan et al. represented a multipath MI based on the same structure [49], however, one of the SMF ends was converted to a specially tailored spherical end in order to enhance the extinction ratio of the interfered spectrum. The sensor was also designed for high temperature measurements. Moreover, Gan et al. demonstrated an MZI using the same seven-core fiber with two ends of the fiber having tapered regions, for a simultaneous measurement of strain and temperature [50]. In 2011, Silva et al. used a suspended MCF for curvature measurement. The interference between the propagation modes guided in cores contributed to the simultaneous measurement of strain and curvature [51]. In 2015, the strongly coupled seven-core MCF was used by Salceda-Delgado et al. for curvature sensing using the super-mode interference excited in the fiber [52]. But the sensor was designed to be sensitive to bending under different curvatures in only one dimension. And in 2017, Villatoro et al. used this fiber for an interferometric vibration sensor [53]. The strongly coupled seven-core fiber was spliced to the SMF, and the other end of the MCF was cleaved and placed in a cantilever position. Through monitoring the intensity of the reflection mode, the vibration-induced strain was detected. Moreover, Zhang et al. twisted the seven-core fiber into a helical structure and spliced it in between two sections of multimode fibers [54]. The proposed MZI was designed for the simultaneous measurement of the strain and temperature. In 2018, Tan et al. fabricated the MZI-based torsion sensor through tapering the seven-core fiber [55]. The clockwise and counterclockwise direction can be discriminated by the blue or red shifts of the interference pattern.

The interferometric MCF sensors have shown their great advantages on the small and compact size, high sensitivity and easy fabrication, while most of the interferometers are sensitive in only one direction for the strain, curvature, acceleration and flow velocity measurement. In other words, these interferometers are mainly designed as one-dimensional sensor. In order to achieve a multi-dimensional sensing, several interferometric sensors can be integrated. However, the number of the integrated sensors are limited, and the complexity of the sensor system is enhanced. Under this circumstance, the introduction of FBG technique into the MCF application can be of great value to achieve multi-dimensional sensing in a single fiber, due to the intrinsic spatial multiplexing of the MCF. Also, different cores in the MCFs are possible to be considered as individual transmission channels, with the help of fan-in/out devices. The investigation of FBG-based four-core fiber was as early as 2003 [56]. At that time, Flockhart et al. reported a two-axis curvature measurement. FBGs were inscribed in three of the four cores simultaneously, and the curvature can therefore be determined in two-axis range through measuring the strain difference applied on different FBGs in individual cores. However, the results only showed the direction related characteristics, the bending radius and direction were not retrieved exactly. After that, in 2006, Fender et al. used the FBG integrated with arrayed waveguide gratings (AWGs) in MCF for the two-axis curvature analysis [57].

Through monitoring the Bragg wavelength of the FBG during the fabrication process, it was designed to be located in between two AWG channels. As a result, the measurement of wavelength shift could be converted to the intensity analysis. The differential strain in orthogonal pairs of FBGs were able for the curvature retrieve. They also used the same four-core fiber for the design of the two-axis vibration sensor, inclination sensor and displacement sensor [58-60]. These sensors demonstrated a good direction-related response and sensitivity, but the actual orientations were not obtained. In 2015, a four-core based two-dimensional curvature sensor was proposed by Barrera et al. [61]. Two different sets of FBG arrays were prepared for the uniform and non-uniform curvature measurement, respectively. Size of the FBG array decided the spatial resolution of the designed curvature sensor. Zhang et al. used a specially designed seven-core MCF for the vector bend sensing, with the refractive index of the central core being a little lower than the six outer cores [62]. FBGs were written in all seven cores simultaneously, and the reflection spectrum of the FBG in the center core is separated from those in the outer cores due to this difference. As a result, the bending response can be analyzed. Apart from the previous research study, Hou et al. also used the FBG-based seven-core MCF for a two-dimensional bend sensing in 2018 [63]. At this time, the result represented not only a direction dependent response, the bending direction and curvature value can be confirmed simultaneously.

While the research on MCF-based two-dimensional sensors attracting great interests, the MCF-based three-dimensional sensing, which is also called the shape sensing has also raised concern. And this technology is not only essential for the physical parameter detection, but they have also been widely investigated in medical and biomedical areas. Duncan et al. from Luna Innovations Incorporated used an FBG array inscribed in a three-core fiber for shape reconstruction [64]. By using the position of the fiber end as the initial coordinate, the travelled distance by the fiber together with the strain measurements in the first FBG triplet allow the position and direction of the next triplet to be determined with optical frequency domain reflectometry (OFDR) technology. Moore et al. from NASA Langley research center, also reported their three-dimensional shape sensing works using FBG array in a three-core fiber [65]. The FBG array was inscribed along the three-core fiber. Through monitoring of Bragg wavelength shifts at different positions, together with the OFDR and Frenet-Serret formulas, the shape of the object was finally achieved. In 2014, Ryu et al. reported the use of three FBGs mounted to a polymer tube as a shape sensor, with an optimized strain transfer model between the fiber and tube to improve the sensor accuracy [66]. Westbrook et al. from OFS labs utilized twisted seven-core MCF grating arrays for the shape reconstruction [67, 68]. In Westbrook's works, in addition to the shape, the twist induced Bragg wavelength shift can also be distinguished because a permanent twist was added to the outer cores. Meanwhile, the FBG-based MCF shape sensing is also applied to reconstruct the shape of medical instruments. Recently, the FBG-based MCF shape sensing is also applied to reconstruct the shape of medical instruments. In 2019, Khan et al. validated the usage of a four-core MCF to calculate the shape of the catheter, with four MCFs inscribed with FBGs connected with the catheter [69]. Curvature and torsion at each FBG position were retrieved with small errors. Except for the FBG-based shape sensing technology, the distributed shape sensing is also investigated based on the Brillouin scattering, Brillouin optical time domain reflectometry (BOTDR) and optical time domain reflectometry (OTDR) in MCF [70-72], which has greatly enhanced the shape sensing distance.

The aforementioned investigations indicate a great research value for MCF to be developed in multi-dimensional sensing applications, including the design of both the two-dimensional and three-dimensional sensors. However, most of the reported MCF-based research are aimed at interferometric structures. For those FBG-based MCF sensors, the intrinsic advantage of having several individual transmission channels in the MCF is not fully developed, causing mainly of those reported two-dimensional sensors just represented the orientation related response, without retrieving the actual direction. Also, for the three-dimensional shape sensing devices, usually the results only showed the curvature and torsion at testing points, the real shape for the objects undertest is not yet achieved.

## 2.3 FBG Inscription Technology and Characterization

FBG is an essential technique applied in the fiber-optic devices, which is a permanent and periodical refractive index variation in the core along the fiber length. The generation of Bragg gratings was firstly observed by Hill et al. in 1978 [8], through exposure of the germanosilicate fiber to an argon-ion laser at a wavelength of 488 nm. Generally, the periodical structure is caused by the high-power UV, which is induced by the fiber photosensitivity phenomenon. Over the past decades, a considerable effort, such as hydrogen loading, high concentration rare earth dopants and flame brushing has been put to investigate the enhancement of fiber photosensitivity.

Among them, hydrogen loading is the most common technique to obtain a high photosensitivity level, which was first discovered by Lemaire et al. in 1993 [73]. Prior to UV exposure, the fiber is supposed to be immersed in the hydrogen chamber at a temperature of 25 to 80 °C and a pressure of 150 atm for one week (a shorter immersion time at higher temperature). This process introduces a diffusion of the hydrogen molecules into the fiber. When the fiber is UV exposed, the hydrogen molecules react to Si-O-Ge bonds and formatting the OH absorbing species, leading to the localized index increase. Another common method to enhance the photosensitivity is the rare earth doping in the fiber, such as Germanium (Ge), Boron (B), Nitrogen (N), Lead (Pb), Titanium (Ti), and Fluorine (F) etc. [74-77], with each dopant having its own characteristics. For example, $GeO_2$ is the most widely applied dopant in fiber, while an increased photosensitivity is observed with $B_2O_3$ co-doped. And $TiO_2$ is usually doped in the outer-cladding of the fiber due to the higher mechanical strength. In addition to dopants, flame brushing is also an effective technique to enhance the photosensitivity, where a hydrogen flame together with a limited amount of oxygen is used to brush the specific region of the waveguide at a temperature of 1700 °C [78].

Basically, only if the fiber has the characteristic of photosensitivity, it is possible to inscribe FBGs by refractive index modulation using a UV excimer laser with specific wavelengths, such as 193 nm, 248 nm and solid-state laser at 213 nm, 266 nm. However, the necessity of photosensitivity feather is removed under different laser sources. For example, FBGs are also supposed to be fabricated with the help of the femtosecond laser. It needs no more photosensitivity [79], which is caused by the interaction between the femtosecond laser and the dielectric material with nonlinear photoionization mechanisms [80, 81]. In most cases, femtosecond laser causes a physical damage to the fiber and forms the grating structure [82]. The laser pulse has a high energy without too much thermal effect, making the femto-inscribed FBGs a high thermal robustness [83]. In addition, the $CO_2$ laser irradiation is an alternative method for grating inscription, especially for LPG, due to the relaxation of residual-stress induced during fiber drawing [84]. Usually, for the silica fiber, shorter wavelength lasers, e.g., 193 nm, 213 nm, 248 nm and 266 nm are used due to their higher energy. Meanwhile, for polymer fibers, such as the PMMA-based polymer fiber, the 325 nm laser is a typical choice for FBG fabrication [85], while 248 nm laser is an another great candidate for the ZEONEX-based polymer fibers [86].

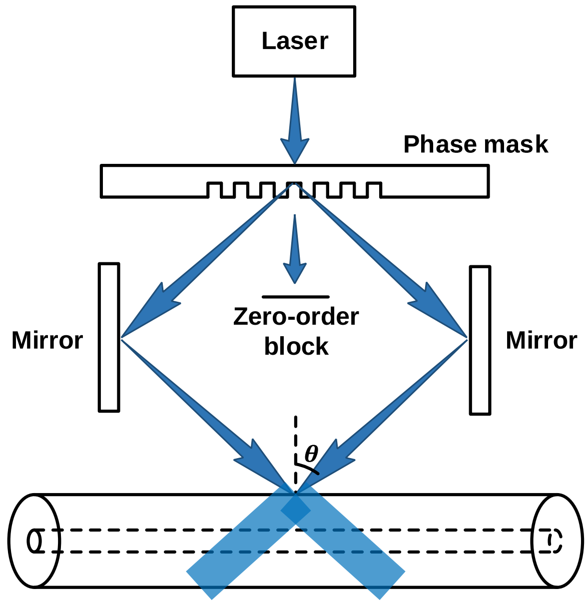


Figure 2.2. Talbot interferometer technique for FBG inscription.

There are several techniques widely used for the FBG inscription, such as the Talbot interferometer, the phase mask technique, and the point-by-point inscription technique. Schematic figure of the Talbot interferometer technique is represented in Figure 2.2. Laser beam which transmits after the phase mask is diffracted into different directions, with the main energy concentrated on the +1 and -1 orders of the diffraction beam. Generally, phase mask is fused silica substrate with a one-dimensional pattern etched into the surface, which splits the laser beam into several diffractive beams [87]. The phase mask maximizes energy in +1 and -1 orders, with each containing approximately 35% of the transmitted power and suppresses the zero order below 3% at the targeted wavelength. After reflection of two mirrors, the ±1 order beams are recombined and focused on the fiber. Changing of the recombining angle $\theta$ will leads to the variation on the period of the interference fringe, which is influenced by rotating the mirror direction. Correspondingly, the interference pattern and the period of the FBG are changed. The Talbot interferometer method requires a UV source with good spatial coherence, while the interference fringe is highly sensitive to the alignment of the optical system. Furthermore, the maintenance of a good fringe contrast requires high mechanical stability and isolation from the ambient vibration, which enhance the requirement of the system.

Figure 2.3 depicts the schematic representation of the typical set up for the phase mask based FBG inscription technology. Laser beam transmits through the phase mask, after which the interference pattern between various orders is focused on the fiber and creates the periodical change of the refractive index. The laser is placed on the translation stage, which helps conduct the beam scanning during the inscription process. The phase mask technology is simple for implementation, and far less sensitive to vibrations and system alignment, which makes it generally more suitable for the FBG fabrication. However, the Bragg wavelength depends greatly on the period of the phase mask, causing the demand for different phase masks.

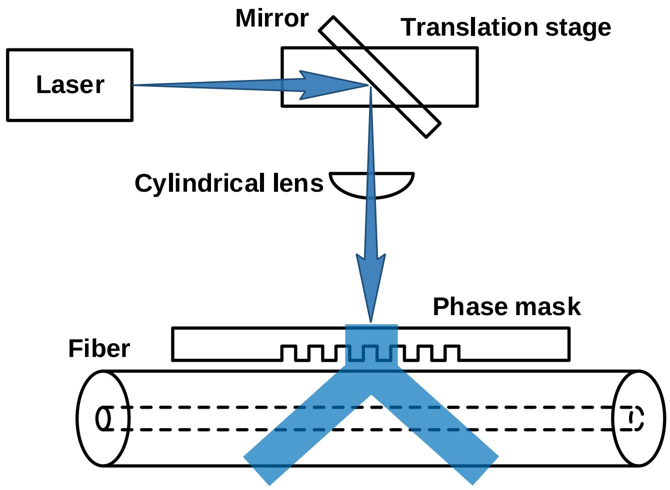

Figure 2.3. Phase mask technique for FBG inscription.

Different from the aforementioned two methods, the point-by-point irradiation method requires neither phase masks nor photosensitivity. It is performed through collimating the laser beam on the fiber after intensity modulation and collimation, and then modulate the refractive index of the fiber. The point-by-point inscription method enables the advantages of high flexibility and short time consuming. Generally, there are two types, including the femtosecond laser-based and $CO_2$ laser-based technology. Figure 2.4 describes the system of a femtosecond laser based FBG inscription technology. Laser beam is firstly focused by microscopic objectives and then to the fiber. The fiber is placed on a stable and high precision translation stage, with the capability of movement along the fiber axis at a constant speed. Therefore, each laser pulse produces a grating pitch at the focal point of the beam in the fiber core [88].

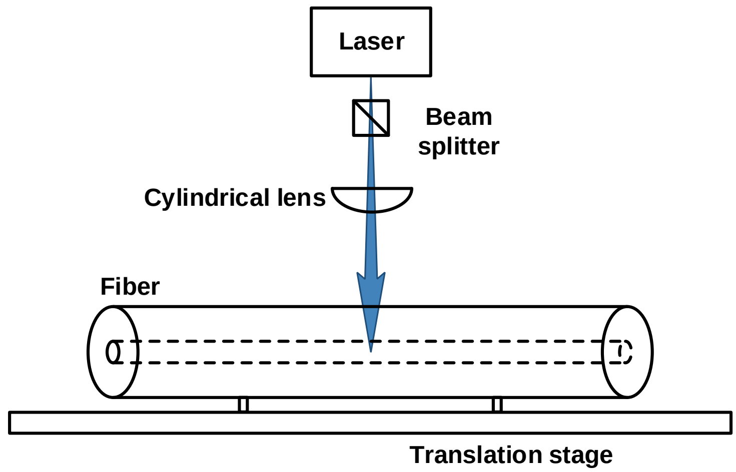

Figure 2.4. Point-by-point technique for FBG inscription.

After the FBG fabrication, when a broadband source is launched into the fiber and reaches the FBG position, part of the light with specific wavelength is reflected, which is named as Bragg wavelength. As is shown in Figure 2.5, there is a reflective peak in the reflection spectrum, and a corresponding dip in the transmission spectrum.

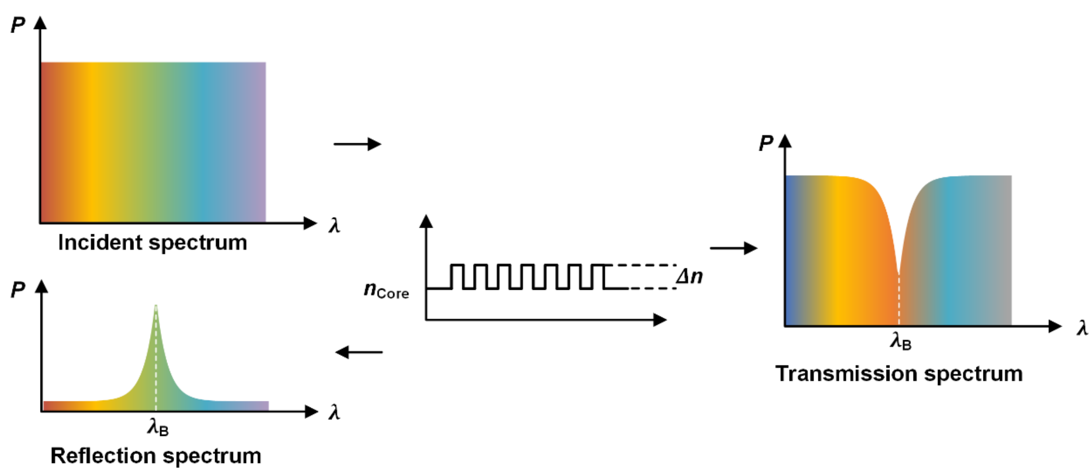

Figure 2.5. Reflection and transmission spectra of an FBG.

The FBG is resulted from the permanent index perturbation, and the refractive index along the fiber ( $z$ direction) can be expressed as [89]:

$$n(z) = n_0 + \overline{\delta n}(z) = n_0 + \Delta n(z)\left[1 + \gamma \cos(\frac{2\pi}{\Lambda} z + \phi(z))\right], \tag{2.1}$$

where $n_0$ represents the refractive index of the fiber core, $\Lambda$ is the grating period, $\Delta n(z)$ is the index change spatially averaged over a grating period, $\varphi(z)$ describes the grating chirp and $\gamma$ is the fringe visibility of the index change. The intensity of FBG is proportion to the index modulation. Due to the index modulation, the effective refractive index $n_{eff}$ of the guided mode in the fiber is changed. Based on the couple-mode theory, which is an effective tool for the quantitative information on the diffraction efficiency of the grating, the coupling equations of the optical field in the Bragg grating can be written as [89]:

$$\begin{cases} \frac{dR}{dz} = i\hat{\sigma}R(z) + i\kappa S(z) \\ \frac{dS}{dz} = -i\hat{\sigma}S(z) - i\kappa^* R(z) \end{cases}. \tag{2.2}$$

Here, $R$ and $S$ represents the reflection mode and counter-propagating mode, respectively, where the amplitude can be expressed as [89]:

$$\begin{cases} R(z) = A(z)\exp(i\delta z - \phi/2) \\ S(z) = B(z)\exp(-i\delta z + \phi/2) \end{cases}. \tag{2.3}$$

Also in Equation (2.2), $\kappa$ is the coupling coefficient, while $\hat{\sigma}$ is the self-coupling coefficient and $\delta$ is the detuning, which are determined through:

$$\begin{cases} \hat{\sigma} = \delta + \sigma - \dfrac{1}{2}\dfrac{d\phi}{dz} \\ \delta = \beta - \dfrac{\pi}{\Lambda} = \dfrac{2\pi n_{eff}}{\lambda} - \dfrac{\pi}{\Lambda} \end{cases}. \tag{2.4}$$

As a result, in Equation (2.4), the specific wavelength has a maximum reflectivity when $\delta$ equals to 0, which is named as Bragg wavelength $\lambda_B$,

$$\lambda_B = 2 n_{eff} \Lambda. \tag{2.5}$$

The Bragg wavelength is also determined by phase-match condition in [90].

Based on Equation (2.5), $\lambda_B$ is dependent on two parameters, including the effective refractive index of the guided modes $n_{eff}$ and the period of the grating $\Lambda$, which are influenced when environmental variation happens, such as strain and temperature. Changes of them induce a red or blue shift of the Bragg wavelength, which relates to a longer or shorter wavelength shift, and can be expressed as follows [91]:

$$\Delta\lambda_B = 2 n_{eff} \Lambda \left( \left\{ 1 - \frac{n^2}{2}\left[ P_{12} - \nu\left( p_{11} + p_{12} \right) \right] \right\} \varepsilon + \left[ \alpha + \frac{1}{n_{eff}} \frac{dn_{eff}}{dT} \right] \Delta T \right), \tag{2.6}$$

where $\varepsilon$ is the strain applied along the fiber, $p_{11}$ and $p_{12}$ are the Pockel's coefficients; $\nu$ is the Poisson's ratio, $\alpha$ is the thermal expansion coefficient of the fiber material, e.g. silica, which may be effected according to the different dopants in the fiber core, and $\Delta T$ is the temperature variation at the specific FBG. According to [91], the factor

$$p_e = \frac{n^2}{2}\left[p_{12} - \nu\left(p_{11} + p_{12}\right)\right], \tag{2.7}$$

is also considered as the effective photo-elastic coefficient, while the factor

$$\gamma = \frac{1}{n_{eff}}\frac{dn_{eff}}{dT}, \tag{2.8}$$

is the thermal-optic coefficient.

Hence, the strain and temperature influence on the Bragg wavelength shift can be rewritten individually as:

$$\begin{cases} \Delta\lambda_B = \lambda_B\left(1 - p_e\right)\varepsilon \\ \Delta\lambda_B = \lambda_B\left(\alpha + \gamma\right)\Delta T \end{cases}, \tag{2.9}$$

where there is a numerical value of 0.22 for $p_e$ in silica fiber. For the conventional SMF, the measured strain response at a constant temperature and thermal responsivity at constant strain are summarized as [91]:

$$\begin{cases} \frac{1}{\lambda_B}\frac{\delta\lambda_B}{\delta\varepsilon} = 0.78\times10^{-6}\ \mu\varepsilon^{-1} \\ \frac{1}{\lambda_B}\frac{\delta\lambda_B}{\delta T} = 6.67\times10^{-6}\ {}^{\circ}C^{-1} \end{cases}. \tag{2.10}$$

The strain and temperature sensitivity are also measured in the silica fiber, with a wavelength resolution of 1 $pm$ required to resolve a temperature variation of 0.1 $^{\circ}C$, or a strain variation of 1 $\mu\varepsilon$.

## 2.4 FBG Inscription in MCFs

For a weakly-coupled MCF with low core-to-core crosstalk, FBGs inscribed in all the fiber cores are possible to be monitored individually with the help of a fan-in/out device, which is named as the MCF coupler. The FBG inscription process in the MCF is similar compared with the SMF. All the inscription techniques, including the Talbot interferometer, side-writing phase mask and point-to-point can help achieve the MCF-based FBG. Usually, prior to the FBG inscription process, the fiber is loaded in the hydrogen chamber at the temperature of ~80 $^{\circ}C$ under a pressure of ~100 bar for 3 days to enhance the photosensitivity, and all the MCFs used in this work are hydrogen loaded. Figure 2.6 depicts the schematic figure of using UV exposure and phase mask technology to inscribe FBGs in MCF.

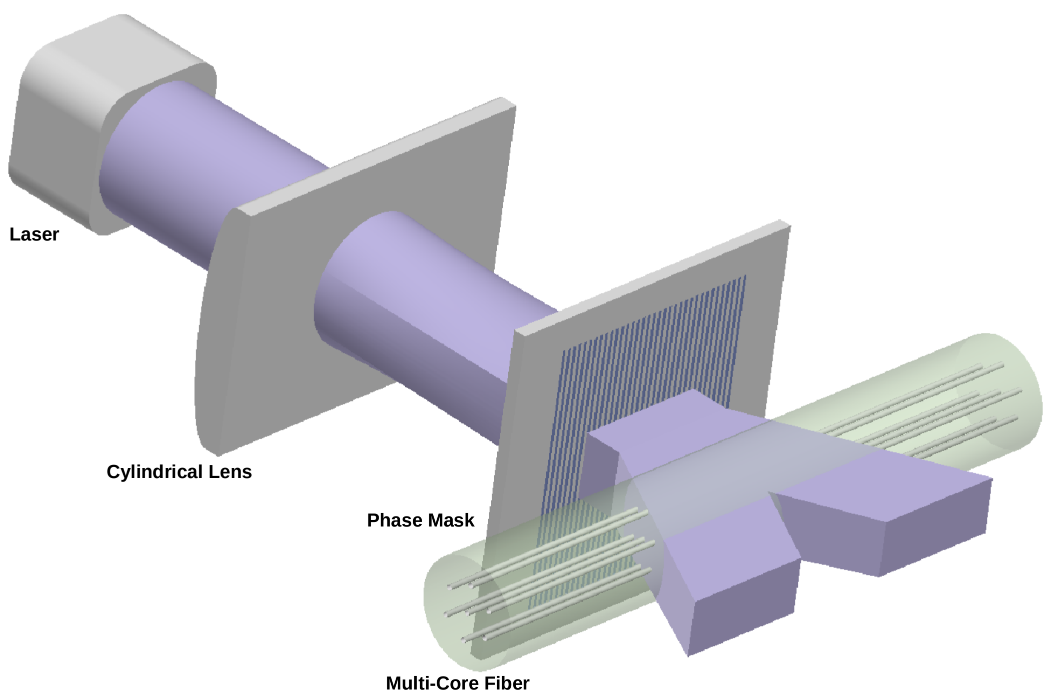


Figure 2.6. Schematic figure of using UV exposure to inscribe FBGs in MCF.

### 2.4.1 Characteristics of MCF-based FBGs

During inscription, the laser is focused onto the MCF. Here we consider the fiber direction as $z$ axis, and the distance from the phase mask to the fiber as $y$ axis, the intensity of the interference pattern is concluded as [92]:

$$I(y,z) = f(y,z)\left[u(z-ay) - u(w_0 - z - ay)\right]e^{-\alpha y}e^{-i\frac{2\pi}{\Lambda}z}, \tag{2.11}$$

where $I(y,z)$ is the laser intensity, $f(y,z)$ is a shaping function representing the profile of the interference pattern, $u(z)$ is the step function that confines the interference pattern within the laser beam size, $a$ is a reduction constant of interference length related to the distance from fiber to the phase mask, $w_0$ is the waist of the laser beam, $\alpha$ is the attenuation and $\Lambda$ is the period of interference pattern (half of the period of the phase mask). Based on Equation (2.11), the power efficiency degrades when the fiber to phase mask distance gets larger.

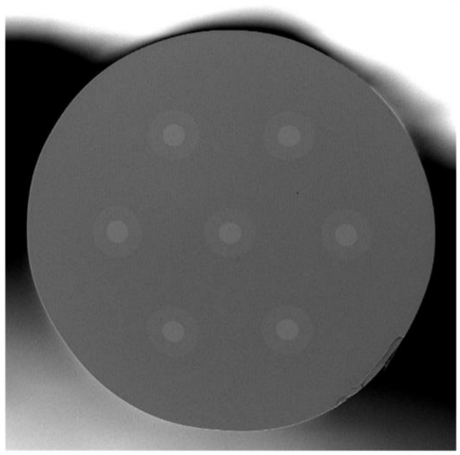

Figure 2.7. SEM image of the homogeneous seven-core MCF.

In this work, a seven-core MCF (YOFC, China) is used to demonstrate the inscription of a single FBG set, together with the phase mask technology using different UV lasers, including 193 nm, 248 nm and 213 nm laser. Figure 2.7 shows the scanning electron microscopic (SEM) image of the seven-core MCF, including its central core and six outer cores. The diameters of the cores and cladding are ~8 and ~150 μm, respectively. In order to make the fiber bend insensitive and reduce the crosstalk among cores, the low-index trench structure is added surrounding each core. The pitch between two adjacent cores is ~42 μm. The splicing between the MCF and the MCF coupler can be completed with the help of a polarization maintaining splicer, under the mode of "End View" to adjust the rotation angle.

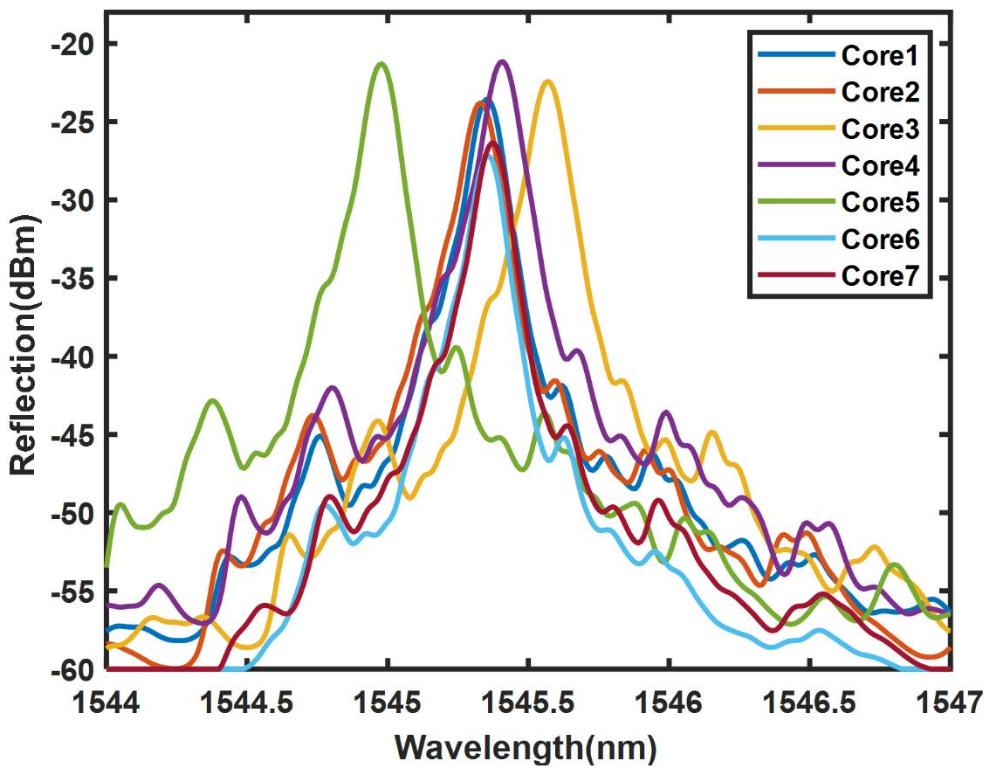


Figure 2.8. Reflection spectra of the FBGs inscribed in seven-core MCF using 193 nm laser.

According to Equation (2.5), the Bragg wavelength of each core in the MCF is dependent on the period of phase mask and the guided modes in individual cores. First, we used an 193 nm ArF excimer laser (Coherent) and phase mask (Bragg Photonics) to write FBGs in the MCF. The laser power was 100 mJ and the pitch of phase mask was 1068 nm. In order to obtain a stable FBG response, the beam scanning technology with a scanning speed of 0.1 mm/s was adopted. After inscription, the MCF was firstly spliced to the MCF coupler (YOFC, China) with the help of a polarization maintain fiber fusion splicer (Fujikura, LZM-100), after which an interrogator (Micron Optics, si155) was used to analyze the reflection and transmission spectra of different cores. Reflection spectra of 10-mm long gratings are shown in Figure 2.8. Bragg wavelengths for cores from 1 to 7 (except 3 due to the breakage of the MCF coupler) are 1545.35, 1545.33, 1545.57, 1545.41, 1544.98, 1545.36 and 1545.37 nm, respectively.

Furthermore, a 248 nm KrF excimer laser (Coherent) was used to inscribe FBGs in MCF, with a phase mask (Ibsen Photonics) period of 1065.42 nm. The spectra of the 10-mm long gratings are represented in Figure 2.9. The laser pulse energy was 85 mJ, with a scanning speed of 0.1 mm/s. Bragg wavelengths for cores from 1 to 7 are 1541.55, 1541.77, 1541.7, 1541.24, 1541.67, 1541.71, and 1541.54 nm, respectively.

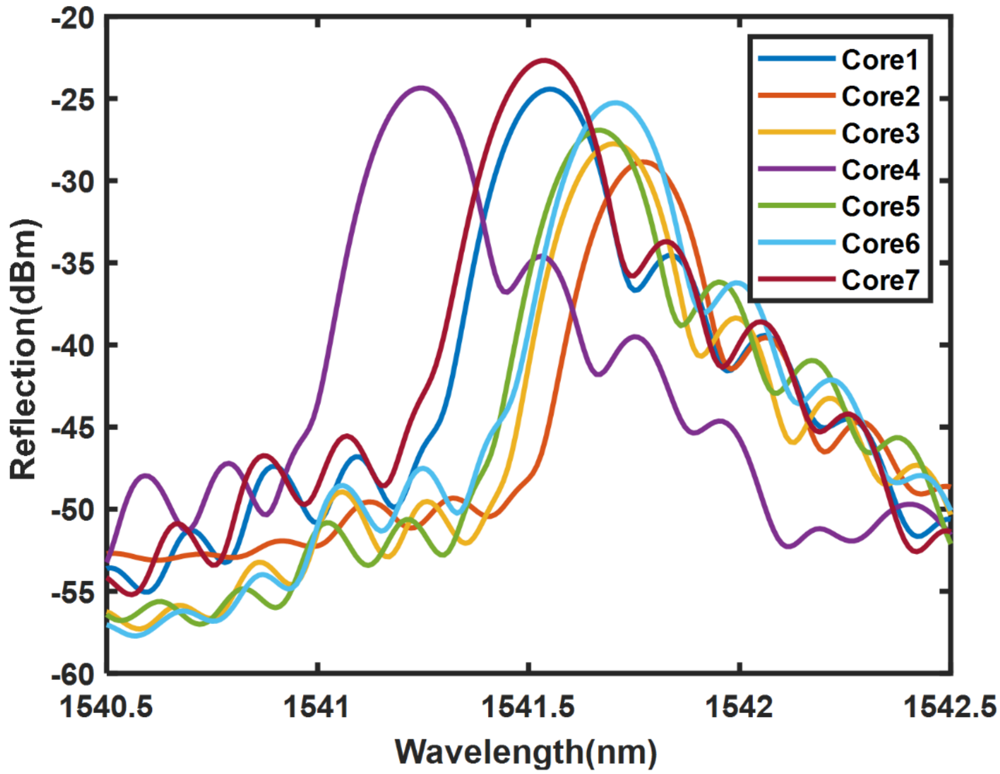

Figure 2.9. Reflection spectra of the FBGs inscribed in seven-core MCF using 248 nm laser.

In addition, a 213 nm solid-state laser (Xiton Photonics, Impress 213) and a phase mask (Ibsen Photonics) with a period of 1061.97 nm were used to inscribe FBGs in MCF. The laser power was 95 mW and the scanning speed was of 0.1 mm/s. Figure 2.10 shows the reflection spectra of the 10-mm gratings, with the Bragg wavelengths for core 1 to 7 of 1537.26, 1537.24, 1537.41, 1537.24, 1537.27, 1537.4 and 1537.48 nm, individually.

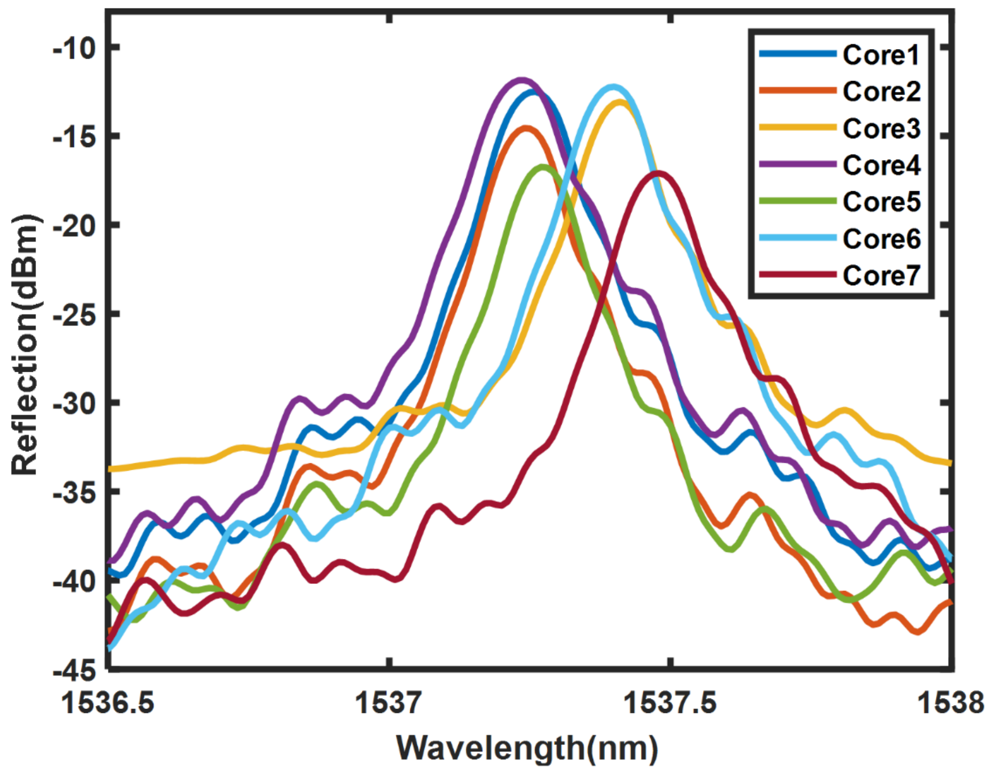


Figure 2.10. Reflection spectra of the FBGs inscribed in seven-core MCF using 213 nm laser.

In an MCF, except for the central core as the SMF's, there are cores sitting away from the center of the cylindrical waveguide, which brings an asymmetric structure into the fiber. Besides, with the help of a MCF coupler, FBG signals in the cores that off the center are monitored, which causes a directional sensitivity. As a result, the FBG set module is capable of distinguishing the orientation in the two-dimensional range due to the spatial distribution of individual cores.

Except for a single FBG set, an FBG array with several FBG sets could be managed on the MCF based on the aforementioned technology. The only difference is, in the single FBG set inscription process, only one phase mask with a fixed pitch length is needed, while in the FBG array several phase masks are applied, which is dependent on the number of the grating sets. Figure 2.11 represents the reflection spectra of FBGs in all cores of the MCF. The length of each grating is 10 mm, with 15 mm space between two adjacent ones. FBGs were inscribed using the 213 nm solid-state laser, together with four phase masks (Canada Limited), with periods of 1057.94, 1064.86, 1075.23 and 1082.15 nm, respectively. It is obvious that the FBG array can be inscribed in all the cores at the same time, with little Bragg wavelength difference between individual cores at each FBG point. Compared with the one FBG set scenario, the MCF-based FBG array introduces a new dimension, which is along the fiber axis. As a result, the MCF-based FBG array can be designed for the three-dimensional sensing applications.

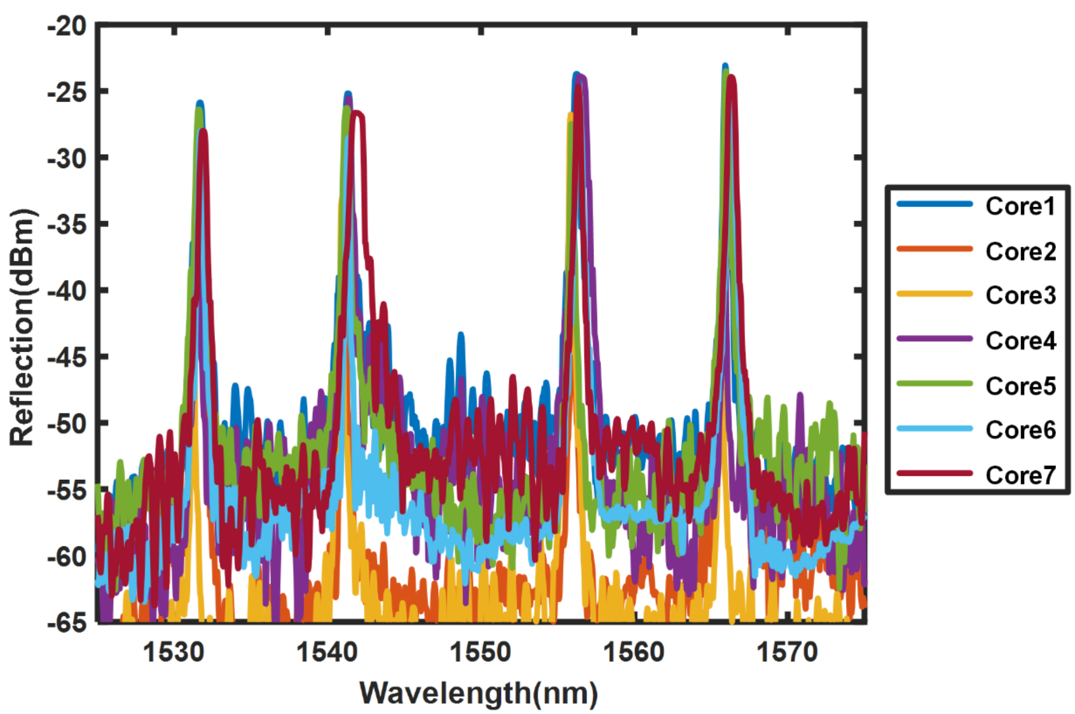


Figure 2.11. Reflection spectra of the FBG array inscribed in the seven-core MCF.

### 2.4.2 Lensing Effect

An apparent slight difference in the Bragg wavelengths of individual cores exists in one FBG set. Due to the spatial distribution of different cores in the MCF, using side illumination to inscribe gratings simultaneously in the fiber bring several issues to the nonuniformity in gratings. Since the fiber is a cylindrical waveguide, the glass fiber acts as a converging lens which narrows the incident beam when it passing through the air-cladding interface [93]. As a result, for cores that are out of the beam range, reduced illumination occurs on them, where the incident beam power varies from each other.

There are researchers trying to overcome the lensing effect during MCF inscription, through putting a lens in front of the fiber to diverge the beam before it encounters the fiber interface [93, 94]. The MCF was placed into a side polished capillary tube, with laser liquid filled in the cavity. Under the circumstance, the flat surface and index matching oil helped the achievement of a better uniformity in illumination theoretically.

### 2.4.3 Shadowing Effect

There is another factor that reduces the uniformity of the MCF-based FBGs, which is the shadowing effect that causes the shadowing of the nearest cores on the furthest cores in the illumination axis [93]. However, a slight rotation can result in a significant variation of the laser intensity on individual cores. For example, in [95], Idrisov et al. theoretically and experimentally investigated the influence of orientation on the illumination intensity. Result comes that when the core is aligned in the illumination axis, a rotation within -2° and +2° is enough for a full illumination of all the cores, and exceeding this range may cause the shadowing effect.

### 2.4.4 Uniformity of Cores in MCF

Another element that influence the uniformity of the MCF-based FBGs is the imperfections in the cores during fiber production [96]. In order to check the fiber characterization, we used the equipment from Interfiber Analysis (IFA-100) to measure the refractive index (RI) difference profile of the MCF used in this work, as shown in Figure 2.12. The RI is measured under the wavelength of 633 nm, with a RI for the matching oil of 1.4587. The maximum RI differences compared with the cladding in cores from 1 to 7 are 0.00422, 0.00273, 0.00302, 0.00339, 0.00277, 0.00326 and 0.00312, with a maximum difference of 0.00149 among cores. The refractive index in each core may also bring Bragg wavelength variation during FBG inscription.

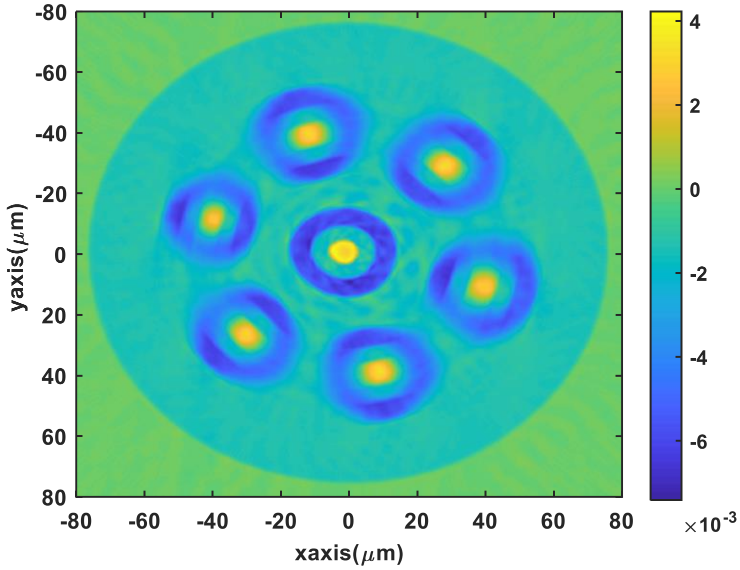


Figure 2.12. Refractive index difference of individual cores in MCF.

However, there are several factors causing Bragg wavelength difference for FBGs in individual cores. In this work, we used the MCF coupler to demodulate separate FBGs in each core. Since the fiber in this work is a weakly-coupled MCF with core-to-core pitch up to 42 μm, crosstalk among cores is small enough for isolation [97]. When the MCF is designed for multi-dimensional sensing applications, only the Bragg wavelength shifts in individual cores are monitored, the absolute values of the Bragg wavelength in specific cores at the starting point are not concerned.

## 2.5 FBG-based MCFs for Multi-Dimensional Sensing

### 2.5.1 Two-Dimensional Vector Sensing

When the MCF is applied for the sensing applications, the fiber experiences the change of physical environment, which is reflected in the variation of these essential parameters in fiber-optic sensors. Under the FBG structure, the Bragg wavelength of FBG is changed due to the environment change. For the MCF-based FBG sensors, the outside changes directly induce the wavelength shifts of all the cores in MCF at the same time. Detection of the physical environment changes can be converted to the monitoring of strain applied on the fiber, except the detection of temperature. However, when the strain is applied, the FBG response in separate cores are different from each other.

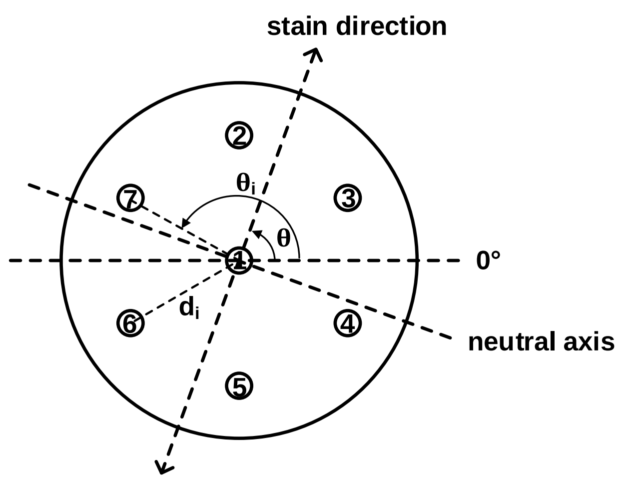


Figure 2.13. Schematic of the cross-section for a seven-core MCF.

For example, in the seven-core MCF, with the cross-section figure shown in Figure 2.13, the outer cores (e.g., core 2-7) are sensitive to the applied strain, while the central one (e.g., core 1) is insensitive. The schematic figure of the FBG-based MCF under bending situation is shown in Figure 2.14. In other words, if the fiber experiences a uniform strain, Bragg wavelengths in the outer cores are shifted, while the Bragg wavelength in the central core is kept unchanged. Also, based on the theory of the wavelength shift, a blue shift occurs when the core is compressed, while a red shift appears when the core is stretched. However, due to the symmetric structure of a cylindrical fiber, one side of the fiber is stretched while the other side compressed, causing different FBG responses of separate outer cores.

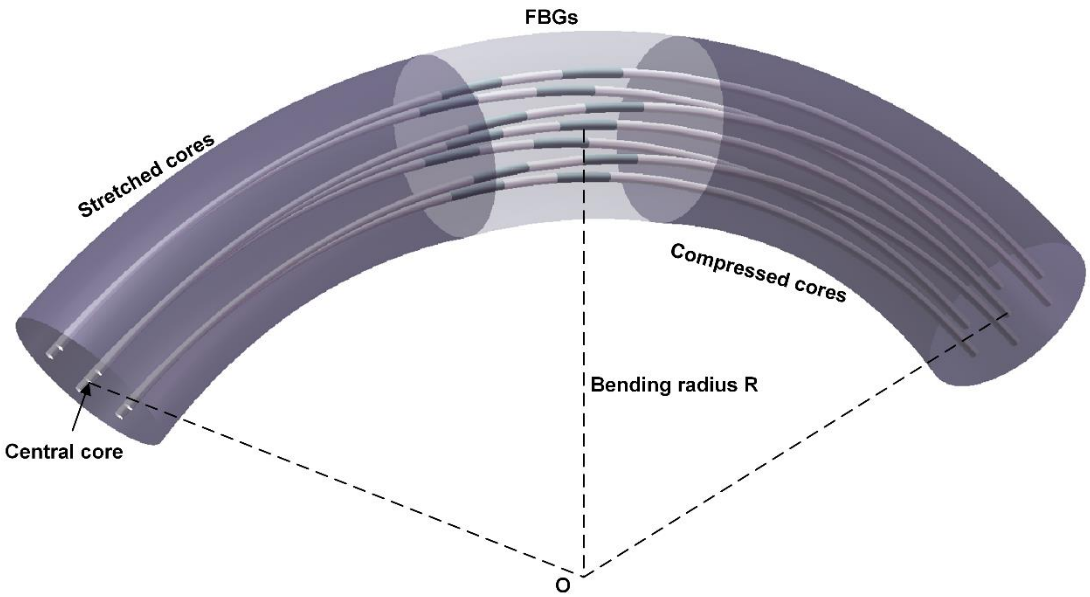


Figure 2.14. Schematic figure of the FBG-based MCF under bending.

The Bragg wavelength shift $\Delta\lambda$ can be expressed by [91]:

$$\Delta\lambda_i = \left(1 - p_e\right)\lambda_i \cdot \varepsilon_i, \tag{2.12}$$

where $\lambda_i$ is the Bragg wavelength in each core $i$, and $\varepsilon_i$ is the strain applied on the corresponding core, which can be described as [66]:

$$\varepsilon_i = \frac{d_i}{R}\sin\left(\theta + \theta_i\right), \tag{2.13}$$

where $d_i$ is the distance between the outer core $i$ and the core 1. $\theta$ and $\theta_i$ represent the orientation of the applied strain and angular position of each outer core $i$, respectively, and $R$ is the strain-induced bending radius.

During the measurement, the Bragg wavelength shift $\Delta\lambda$ is obtained through the usage of interrogator, while $\lambda_i$ is confirmed in advance. As a result, Equation (2.12) can be revised as follows:

$$\frac{\Delta\lambda_i}{\lambda_i} = \left(1 - p_e\right)\frac{d_i}{R}\sin\left(\theta + \theta_i\right), \tag{2.14}$$

and the strain is related to the wavelength shift via:

$$\varepsilon_i = \frac{\Delta\lambda_i}{\lambda_i}\frac{1}{1 - p_e}. \tag{2.15}$$

It is noticeable that in Equation (2.14), $\theta_i$ for each core $i$ can be determined from Figure 2.13 since the angular position is fixed when the fiber direction is confirmed. Also, pitch $d$ remains the same for all cores, while $R$ is much larger than $d$. If two of the six outer cores are taken for the calculation, through the ratio of two equations, the strain direction can be derived as:

$$\theta = \tan^{-1}\left(\frac{\frac{\Delta\lambda_i}{\lambda_i}\sin\theta_j - \frac{\Delta\lambda_j}{\lambda_j}\sin\theta_i}{\frac{\Delta\lambda_j}{\lambda_j}\cos\theta_i - \frac{\Delta\lambda_i}{\lambda_i}\cos\theta_j}\right), \tag{2.16}$$

where $i$ and $j$ are two different outer cores. From Equation (2.16) it is apparent that the phase difference between $\theta_i$ and $\theta_j$ could be any value except $\pi$, which means the value 0 cannot appear in the denominator. In other words, when choosing the two outer cores, they should not be aligned in a straight line together with the central core. The physical explanation is also straightforward, for those two cores that are central symmetric by the central core, e.g., core 3 and 6 in Figure 2.13, the FBG responses share the same information except for the blue or red shift under strain, meaning the which is not helpful when retrieving an orientation-related parameter.

Based on the two-dimensional operation principles, the MCF inscribed with FBGs is capable of being designed as accelerometers, inclinometers and several other fiber-optic sensors. More details of these applications are introduced in the following chapters.

### 2.5.2 Three-Dimensional Shape Sensing

In order to conduct the shape sensing in a three-dimensional space, the most essential parameters are the curvature and torsion, which determine the bend and twist phenomenon in a shape of the fiber. Different from the two-dimensional measurement, an FBG array is necessary in the three-dimensional sensors. Curvature and torsion in the three-dimensional space can be described through the famous Frenet-Serret formulas [98]. Firstly, we determine the point $r$ in the three-dimensional space as follows:

$$r(s) = x(s)\hat{i} + y(s)\hat{j} + z(s)\hat{k}, \tag{2.17}$$

where $\hat{i}$, $\hat{j}$ and $\hat{k}$ are the unit vectors in the $R^3$ space along the $x$, $y$ and $z$ coordinate, respectively. The Frenet-Serret frame is defined by three-unit vectors, including tangent $\boldsymbol{T}(s)$, normal $\boldsymbol{N}(s)$ and binormal $\boldsymbol{B}(s)$, and according to the

Frenet-Serret formulas they are related to each other, which can be summarized as:

$$\begin{cases} \boldsymbol{T}'(s) = \kappa(s)\boldsymbol{N}(s) \\ \boldsymbol{N}'(s) = -\kappa(s)\boldsymbol{T}(s) + \tau(s)\boldsymbol{B}(s), \\ \boldsymbol{B}'(s) = -\tau(s)\boldsymbol{N}(s) \end{cases} \tag{2.18}$$

where $\kappa(s)$ and $\tau(s)$ are the scalar-valued curvature and torsion functions. The schematic figure of a three-dimensional shape sensor based on the MCF-based FBG array is shown in Figure 2.15.

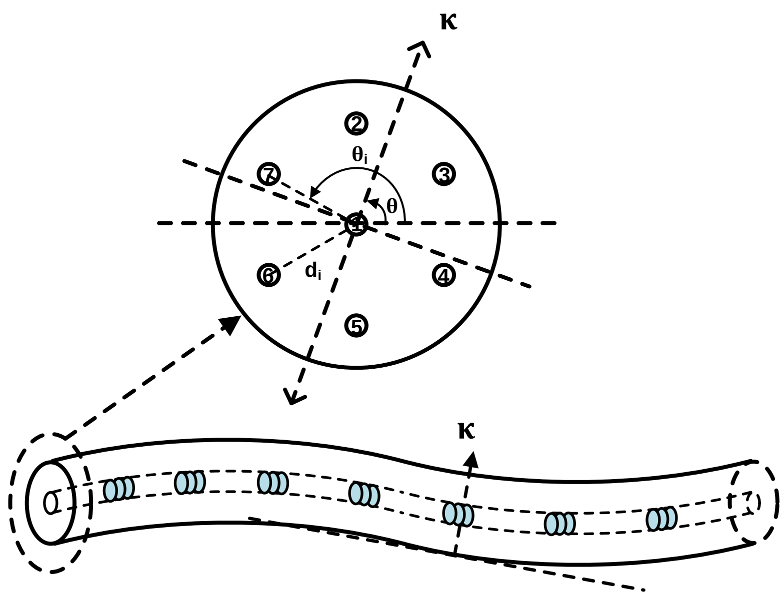


Figure 2.15. The schematic figure of a three-dimensional shape sensor based on an MCF-based FBG array.

In order to calculate the curvature using the information obtained from the FBG in individual cores, we define a curvature vector of core $i$, where the value is dependent on the strain applied on the $i^{th}$ core and the distance between the specific core to the fiber center, while the direction is related to the direction from the fiber center to the $i^{th}$ core.

$$\boldsymbol{K}_i(s) = -\frac{\varepsilon_i(s)}{d_i}\left(\cos\theta_i \hat{i} + \sin\theta_i \hat{j}\right). \tag{2.19}$$

In Equation (2.19), $\hat{i}$ and $\hat{j}$ are the unit vectors align with the local x- and y-axes. Considering $N$ cores used in the calculation, the vector sum of the curvature vector is:

$$\boldsymbol{K}(s) = -\sum_{i=1}^{N}\frac{\varepsilon_i(s)}{d_i}\cos\theta_i \hat{i} - \sum_{i=1}^{N}\frac{\varepsilon_i(s)}{d_i}\sin\theta_i \hat{j}, \tag{2.20}$$

where the local bending direction $\theta$ is defined as

$$\theta(s) = \tan^{-1}\left(\frac{\boldsymbol{K}_{\hat{j}}(s)}{\boldsymbol{K}_{\hat{i}}(s)}\right) = \sin^{-1}\left(\frac{\boldsymbol{K}_{\hat{j}}(s)}{|\boldsymbol{K}(s)|}\right) = \cos^{-1}\left(\frac{\boldsymbol{K}_{\hat{i}}(s)}{|\boldsymbol{K}(s)|}\right). \tag{2.21}$$

When take Equation (2.13) into Equation (2.20), together with the relationship between curvature $\kappa$ and bending radius $R$, which is:

$$\kappa = \frac{1}{R}, \tag{2.22}$$

the curvature vector is described as:

$$\boldsymbol{K}(s) = -\sum_{i=1}^{N}\kappa\sin(\theta+\theta_i)\cos\theta_i \hat{i} - \sum_{i=1}^{N}\kappa\sin(\theta+\theta_i)\sin\theta_i \hat{j}. \tag{2.23}$$

As a result, the value of the curvature vector is given as:

$$|\boldsymbol{K}(s)| = \kappa\sqrt{\left(\sum_{i=1}^{N}\sin(\theta+\theta_i)\cos\theta_i\right)^2 + \left(\sum_{i=1}^{N}\sin(\theta+\theta_i)\sin\theta_i\right)^2}. \tag{2.24}$$

Based on Equation (2.24), curvature $\kappa$ is described as:

$$\kappa = \frac{\left|\boldsymbol{K}(s)\right|}{\sqrt{\left(\sum_{i=1}^{N}\sin(\theta+\theta_i)\cos\theta_i\right)^2+\left(\sum_{i=1}^{N}\sin(\theta+\theta_i)\sin\theta_i\right)^2}}, \tag{2.25}$$

where $\left|\boldsymbol{K}(s)\right|$ is derived based on Equation (2.20) by:

$$\left|\boldsymbol{K}(s)\right| = \sqrt{\left(\sum_{i=1}^{N}\frac{\varepsilon_i(s)}{d_i}\cos\theta_i\right)^2+\left(\sum_{i=1}^{N}\frac{\varepsilon_i(s)}{d_i}\sin\theta_i\right)^2}, \tag{2.26}$$

which means $\kappa$ is expressed via:

$$\kappa = \frac{\sqrt{\left(\sum_{i=1}^{N}\frac{\varepsilon_i(s)}{d_i}\cos\theta_i\right)^2+\left(\sum_{i=1}^{N}\frac{\varepsilon_i(s)}{d_i}\sin\theta_i\right)^2}}{\sqrt{\left(\sum_{i=1}^{N}\sin(\theta+\theta_i)\cos\theta_i\right)^2+\left(\sum_{i=1}^{N}\sin(\theta+\theta_i)\sin\theta_i\right)^2}}. \tag{2.27}$$

It is worth mentioning that Equation (2.27) is a general solution for all kinds of core distributions. However, for those symmetric MCFs, it can be simplified.

Firstly, full expression of Equation (2.24) is:

$$\left|\boldsymbol{K}(s)\right| = \kappa\sqrt{\begin{aligned}&\left(\sin\theta\sum_{i=1}^{N}\cos\theta_i\cos\theta_i+\cos\theta\sum_{i=1}^{N}\sin\theta_i\cos\theta_i\right)^2\\&+\left(\sin\theta\sum_{i=1}^{N}\cos\theta_i\sin\theta_i+\cos\theta\sum_{i=1}^{N}\sin\theta_i\sin\theta_i\right)^2\end{aligned}}. \tag{2.28}$$

Then with the usage of the relationship for $\sin 2\theta = 2\sin\theta\cos\theta$ and $\cos 2\theta = \cos^2\theta - \sin^2\theta$, the Equation (2.28) can be converted to:

$$\left|\boldsymbol{K}(s)\right| = \kappa\sqrt{\begin{aligned}&\left(\sin\theta\sum_{i=1}^{N}\frac{1}{2}(1+\cos 2\theta_i)+\cos\theta\sum_{i=1}^{N}\frac{1}{2}\sin 2\theta_i\right)^2\\&+\left(\sin\theta\sum_{i=1}^{N}\frac{1}{2}\sin 2\theta_i+\cos\theta\sum_{i=1}^{N}\frac{1}{2}(1-\cos 2\theta_i)\right)^2\end{aligned}}. \tag{2.29}$$

For the reason that in the symmetric distributed MCF, angular position of the outer cores $\theta_i$ can be described as:

$$\theta_i = \theta_1 + \frac{2\pi}{N}(i-1). \tag{2.30}$$

Therefore, $\sum_{i=1}^{N} \cos 2\theta_i$ is written by:

$$\begin{aligned}
\sum_{i=1}^{N} \cos 2\theta_i &= \cos 2\theta_1 + \cos 2\theta_2 + \cdots + \cos 2\theta_N \\
&= \cos 2\theta_1 + \cos 2\left(\theta_1 + \frac{2\pi}{N}\right) + \cdots + \cos 2\left(\theta_1 + \frac{2\pi(N-1)}{N}\right) \\
&= \frac{\left[\cos 2\theta_1 + \cos 2\left(\theta_1 + \frac{2\pi}{N}\right) + \cdots + \cos 2\left(\theta_1 + \frac{2\pi(N-1)}{N}\right)\right]\sin\frac{2\pi}{N}}{\sin\frac{2\pi}{N}} \\
&= \frac{\sin\left(2\theta_1 + \frac{2\pi(2N-1)}{N}\right) - \sin\left(2\theta_1 - \frac{2\pi}{N}\right)}{2\sin\frac{2\pi}{N}} \\
&= \frac{2\cos\left(2\theta_1 + \frac{2\pi(N-1)}{N}\right)\sin(2\pi)}{2\sin\frac{2\pi}{N}} = 0.
\end{aligned} \tag{2.31}$$

Similarly, $\sum_{i=1}^{N} \sin 2\theta_i$ is written as:

$$\sum_{i=1}^{N} \sin 2\theta_i = \frac{2\sin\left(2\theta_1 + \frac{2\pi(N-1)}{N}\right)\sin(2\pi)}{2\sin\frac{2\pi}{N}} = 0. \tag{2.32}$$

Based on Equations (2.31) and (2.32), the value of the curvature vector is simplified to:

$$\left|\boldsymbol{K}(s)\right| = \kappa\sqrt{\left(\sin\theta\frac{N}{2}\right)^2 + \left(\cos\theta\frac{N}{2}\right)^2}, \tag{2.33}$$

which represents the curvature:

$$\kappa = \frac{2\left|\boldsymbol{K}(s)\right|}{N}. \tag{2.34}$$

Based on Equation (2.15), the Equation (2.26) can be revised to the expression related to the wavelength shift in an FBG sensor:

$$\left|\boldsymbol{K}(s)\right| = \sqrt{\left(\sum_{i=1}^{N}\frac{\Delta\lambda_i}{\lambda_i}\frac{1}{(1-p_e)d_i}\cos\theta_i\right)^2 + \left(\sum_{i=1}^{N}\frac{\Delta\lambda_i}{\lambda_i}\frac{1}{(1-p_e)d_i}\sin\theta_i\right)^2}, \tag{2.35}$$

with the curvature expressed by:

$$\kappa = \frac{2}{N}\sqrt{\left(\sum_{i=1}^{N}\frac{\Delta\lambda_i}{\lambda_i}\frac{1}{(1-p_e)d_i}\cos\theta_i\right)^2 + \left(\sum_{i=1}^{N}\frac{\Delta\lambda_i}{\lambda_i}\frac{1}{(1-p_e)d_i}\sin\theta_i\right)^2}, \tag{2.36}$$

where $N$ is the number of symmetric core used for shape reconstruction. Hence, Equations (2.21) and (2.36) give the measurement of curvature and bend direction. Meanwhile, the torsion function is obtained from differentiating the bend direction with respect to the fiber length, which is expressed by:

$$\tau(s) = \frac{d\theta(s)}{ds}. \tag{2.37}$$

With the combination of curvature, bend direction and torsion, the origin shape is retrieved with the help of Frenet-Serret formulas.

## 2.6 Summary

In this chapter, a comprehensive review of different types of multi-dimensional fiber-optic sensors, including both interferometric and grating-based sensors are introduced. With a brief introduction to the characteristic of MCFs, fiber-optic sensors using different MCFs are reviewed, as well as the MCF-based multi-dimensional sensors. For the purpose of using MCF-based FBGs for multi-dimensional sensing, three main grating inscription technologies are presented, with emphasis on the phase mask technology to inscribe FBGs in the MCF. Characteristic of MCF-based FBGs is investigated, together with the factors that cause the nonuniformity of Bragg wavelengths in a single FBG set. In order to utilize the MCF-based FBGs for multi-dimensional sensing, theories of both two-dimensional vector sensing and three-dimensional shape sensing are demonstrated.

# Chapter 3 Two-Dimensional Accelerometer

## 3.1 Overview on Fiber-Optic Accelerometers

Accelerometers (vibration sensors) have been widely incorporated in numerous applications such as in seismic exploration [99], navigation systems [100] and in industrial and health monitoring applications [101]. A variety of them exist and are specialized on specific applications. For example, accelerometers used in the detection of seismic waves are required to be sensitive to low frequencies (<100 Hz) [2] and in mechanical equipment such as rotating machinery and aero-engines, sensitive to high frequencies is required [102]. Besides the frequency factor, information on the orientation is another critical detail in vibration systems, such as cantilevered microwire [103]. Various approaches have been reported to achieve a high sensitivity and a dynamic range of frequency responses. However, mechanical measurements in an acceleration system capable of distinguishing vector orientations remain challenging [104]. Generally, multiple single-axis accelerometers have been used to map the vibration directions, thereby, increasing the system complexity.

During the past two decades, fiber-optic accelerometers have attracted widespread interests. Generally, acceleration measurements can be carried out by detection of strain or displacement induced by the movement of the inertial mass attached to the sensor body. In the process of orientation determination, accelerometers vary according to their respective axes of vibration. The most fundamental accelerometers are single-axis, denoting their sensitivity to a single direction of vibration. For example, Cranch et al. reported an accelerometer comprising of a fiber coil embedded in an epoxy disk [105]. Using this design, the strain caused by acceleration has been measured by a Michelson interferometer. However, only the vibration which was vertical to its plane caused the disk to flex. Villatoro et al. has introduced another interferometric sensor through splicing a segment of a strongly-coupled multi-core fiber (MCF) to a conventional single-mode fiber (SMF) [106]. The vibration waves have induced local pressure in the MCF, leading to a periodic shift of the interference pattern. Moreover, Rong et al. has demonstrated a fiber Bragg grating (FBG) based accelerometer in a depressed-cladding fiber [107] where acceleration measurements have been achieved from power detection of the fundamental core mode resonance.

In addition, there are several sensors designed as two-axis optical accelerometers, based on deflection of the sensing element, with its axis perpendicular to the applied acceleration. Fender et al. has proposed an accelerometer using FBGs inscribed in a four-core MCF to sense the strain difference between two cores [58]. When the vibration was normal to the plane formed by the two cores, FBGs in these two cores can only detect acceleration in a certain direction while the other two FBGs remained insensitive, and vice versa. Thus, such a sensor requires two pairs of FBGs to detect accelerations in two orthogonal directions. However, the actual vibration angle during random accelerations remains unexplored. Li et al. has combined two vibration sensors for detection of acceleration sensitivity in two dimensions [108], where a cantilever has been directly fabricated on the SMF itself to measure the deflection caused by vibration. Besides, Linessio et al. has implemented a biaxial optical accelerometer based on four FBGs placed in opposite positions [109], capable of detecting acceleration in two orthogonal directions, simultaneously. However, these structures are sophisticated to fabricate and control, and are sensitive only in two directions.

Recently, the fiber-optic two-dimensional vector accelerometers have greatly raised research interests. The accelerometer can discriminate orientation in 360°, providing more directional information during vibration, especially when the vibration source is unknown [110]. In order to distinguish the vibration direction, Rong et al. has introduced an orientation-sensitive fiber-optic accelerometer based on tilted FBGs (TFBGs) inscribed in the cladding of a thin-core fiber [110]. Strong orientation dependent vibration measurements have been achieved by power detection of the cladding resonance. Moreover, Bao et al. has demonstrated another vector accelerometer based on output power detection of orthogonal FBGs in a multi-clad fiber [104]. However, both of these accelerometers indicate only an orientation dependent acceleration response over a range of 0-360° with the absence of actual vibration orientation at random accelerations. As a result, distinguishing both the orientation as well as the acceleration simultaneously, using a two-dimensional vector accelerometer remains challenging. In other words, information on both parameters should be obtained with the use of a two-dimensional accelerometer under random circumstances.

## 3.2 Principle of the Two-Dimensional Accelerometer

In order to solve the problem of obtaining vibration orientation and acceleration simultaneously in a vibration sensor, a seven-core MCF with FBGs inscribed is used to fabricate a two-dimensional accelerometer. The fiber is the same as the one introduced in Chapter 2, with the geometrical parameters represented in Figure 3.1. Prior to FBG inscription, the seven-core MCF was loaded in a chamber with hydrogen under a pressure of 100 bar at a temperature of ~80 °C for 3 days to enhance its photosensitivity. FBGs were then inscribed in all seven cores simultaneously through laser beam scanning method, using a 248 nm KrF excimer laser (Coherent) together with the phase mask (Ibsen Photonics, 1065.4 nm) technique. The scanning speed and the grating length were 0.01 mm/s and 10 mm, respectively. Schematic illustration of the FBGs inscribed in the seven core MCF is shown in Figure 3.3(b).

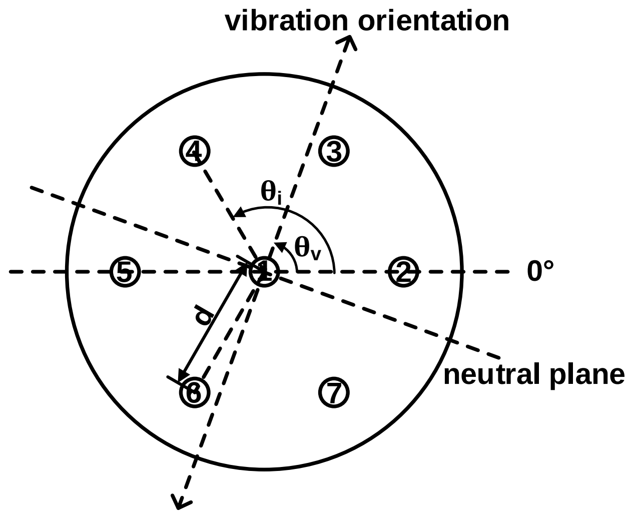


Figure 3.1. Cross-section of the fiber cores with the defined geometrical parameters.

After FBG inscription, the MCF was connected to a 7-to-1 MCF coupler (YOFC) with the help of a polarization maintaining fiber fusion splicer (Fujikura, LZM-100). When the MCF in the fan-out device and the tested MCF are placed together at the two sides of the splicer, they can be spliced through monitoring each of the end-view figure with the help of an "End View" program. As a result, FBGs in each core can be monitored individually during the experiment. An interrogator (Micron Optics, sm130) was used to analyze the reflection spectra. Due to the symmetrical geometry of the cores in MCF, FBGs in three cores including the central core, together with two outer cores, which are not aligned in a straight line are sufficient to develop the vibration sensor. Under this condition, at least three cores are enough to help design the vibration sensor, with the capability of obtaining the vibration orientation, frequency and acceleration at the same time. Figure 3.2 shows the individual reflection spectra of the FBGs in the cores 1, 2, 4 and 6.

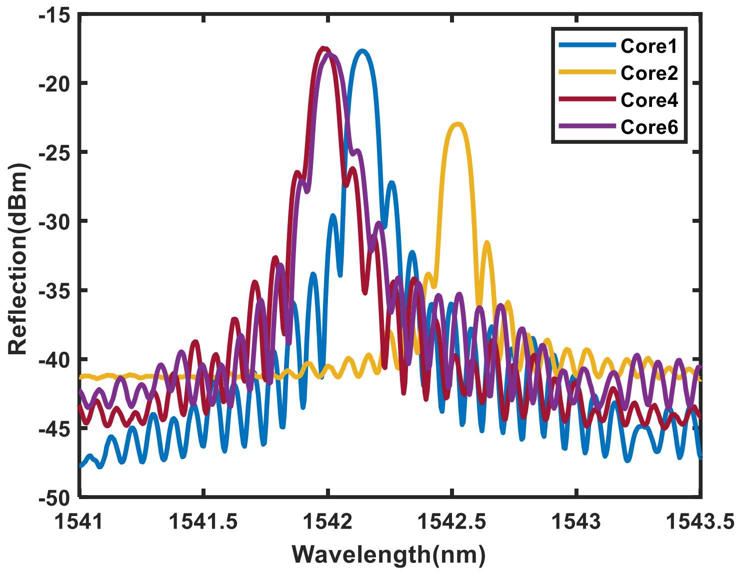


Figure 3.2. Reflection spectra of the FBGs written in core 1, 2, 4 and 6.

The basic principle of the FBG based vibration sensor is to monitor the Bragg wavelength shifts of the gratings inscribed in different cores when vibration occurs. During the vibration process, the outer cores of the MCF, indicate a red shift in the Bragg wavelength when the fiber is stretched. On the contrary, a blue shift occurs when the core is compressed. However, the central core (i.e. core 1) is insensitive to vibration since its transversal position is located on the strain neutral plane at all times. Thus, the FBG in core 1 can be used for temperature compensation. According to Chapter 2.3 , the Bragg wavelength shift of each FBG is dependent on the strain applied on it, while the strain is induced by the vibration in the vibration sensor. As a result, Equation (2.13) is changed to:

$$\varepsilon_i = \frac{d_i}{R}\sin\left(\theta_v + \theta_i\right), \tag{3.1}$$

where $\theta_v$ indicates the vibration orientation.

Since three individual cores, i.e. core 1, 2 and 4, were used to record the periodic change in strain during vibration. For vibrations that occur in random directions, the wavelength shifts of core 2 and 4 appear to have an opposite trend, if they are arranged at opposite sides of the neutral plane, which means one of them experiences a blue shift whereas the other experiences a red shift and vice versa. The wavelength shifts can be formulated as follows.

$$\begin{cases} \dfrac{\Delta\lambda_2}{\lambda_2} = (1-p_e)\dfrac{d_2}{R}\sin(\theta_v+\theta_2) \\ \dfrac{\Delta\lambda_4}{\lambda_4} = (1-p_e)\dfrac{d_4}{R}\sin(\theta_v+\theta_4) \end{cases}. \tag{3.2}$$

In these equations, $\theta_2$ and $\theta_4$ are obtained from Figure 3.1 as 0 and 2π/3, respectively, while it is -2π/3 for core 6. Pitch $d$ remains the same for both cores, while $R$ is much larger than $d$. It is also noticeable that the choice of the set for core 2 and 4 can be any two from the six outer cores, except for those who are central symmetric to the central core. For example, they can be the set of core 2 and 4, or the set of core 2 and 6. Thereby, taking into account the values of maximum wavelength shifts of these FBGs at a certain acceleration, vibration orientation can be calculated from the following equation.

$$\theta_v = \tan^{-1}\left( \frac{\dfrac{\Delta\lambda_2}{\lambda_2}\sin\theta_4 - \dfrac{\Delta\lambda_4}{\lambda_4}\sin\theta_2}{\dfrac{\Delta\lambda_4}{\lambda_4}\cos\theta_2 - \dfrac{\Delta\lambda_2}{\lambda_2}\cos\theta_4} \right) \tag{3.3}$$

Once the orientation of vibration is determined, using the measured sensitivities under varying orientations, together with the wavelength shifts of the corresponding fiber cores, the acceleration value is identified. As a result, orientation and acceleration can be obtained simultaneously in a two-dimensional range.

## 3.3 Characterization of the Two-Dimensional Accelerometer

The experimental setup of the two-dimensional accelerometer is depicted in Figure 3.3(c). The seven-core MCF with the inscribed FBGs is used as the sensing probe, which is fixed on a fiber rotator (Thorlabs, HFR007) to tune the vibration orientation from 0 to 180° in steps of 10°. A detailed illustration of the free-fiber is shown in Figure 3.3(b), where the grating end is placed 2 mm away from the fixed point of the rotator.

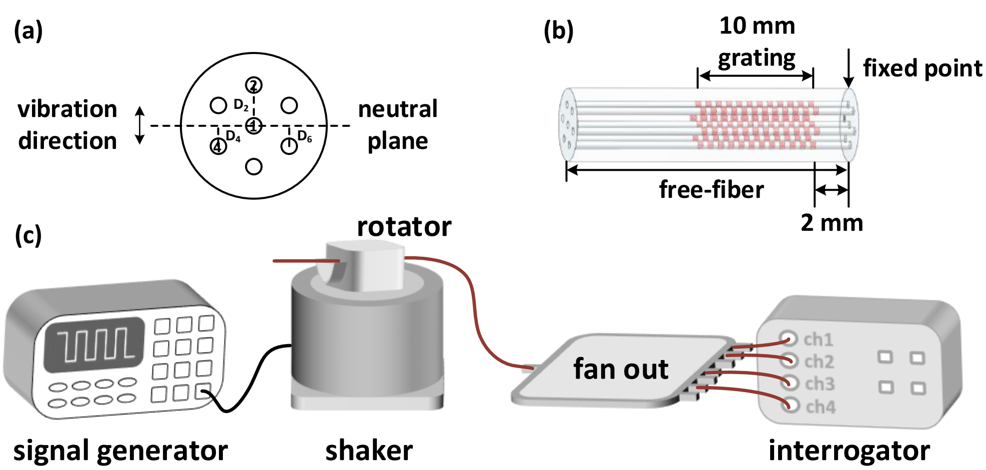


Figure 3.3. (a) Definition of distance *D* from the core of interest to the neutral plane and (b) detailed illustration of the free-fiber with length *L*; (c) schematic setup for the vibration test of the two-dimensional vibration sensor.

Here, we define the orientation of 0° when core 2, 1 and 5 are maintained horizontal as shown in Figure 3.1. According to the structure, length of the suspended fiber is vital, since it behaves as an inertial mass, which determines the resonance frequency. In our experiments, different fiber lengths, including 66, 44.5 and 25 mm were detected under the same structure. Afterwards, the accelerometer was mounted on the top of a shaker (Bruel & Kjaer, Type 4808) to characterize its performance. During the experiment, the shaker was excited by a sinusoidal-signal generator. For the length of 45.5 mm scenario, the acceleration was increased up to 10 g (g = 9.8 m/s$^2$) with vibration frequencies ranging from 5 to 160 Hz. A high-resolution interrogator with a data acquisition rate of 2000 Hz was used to record the wavelength shifts of the four FBGs. Consequently, the vibration measurements were carried out under the conditions with various orientations, frequencies and acceleration values.

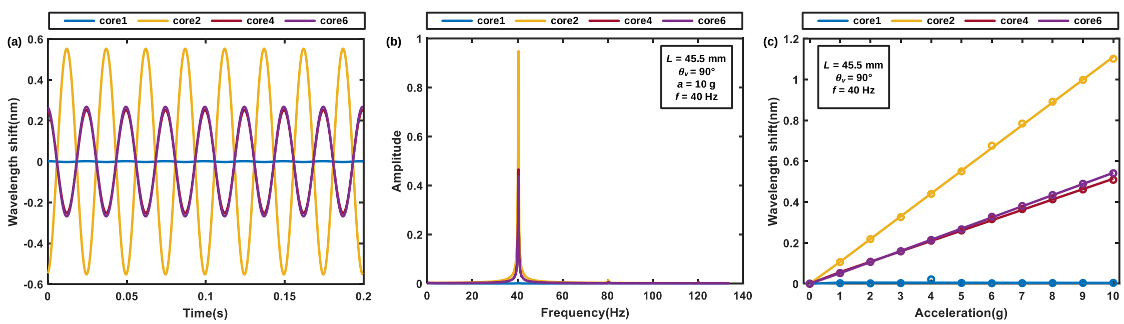


Figure 3.4. (a) Real-time wavelength shifts of FBGs in core 1, 2, 4 and 6 with the following values: $L$ = 45.5 mm, $f$ = 40 Hz, $\theta_v$ = 90° and $a$ = 10 g. The corresponding (b) FFT spectrum with $a$ = 10 g, and (c) wavelength shifts versus applied acceleration with values from 0 g to 10 g.

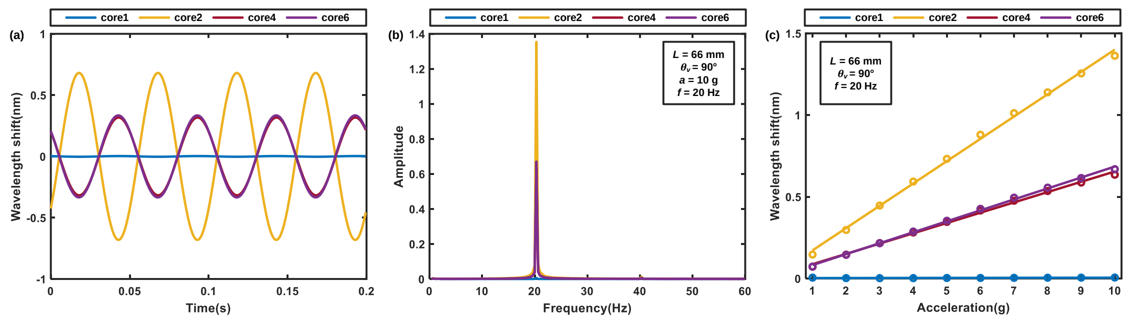


Figure 3.5. (a) Real-time wavelength shifts of FBGs in core 1, 2, 4 and 6 with the following values: $L$ = 66 mm, $f$ = 20 Hz, $\theta_v$ = 90° and $a$ = 10 g. The corresponding (b) FFT spectrum with $a$ = 10 g, and (c) wavelength shifts versus applied acceleration with values from 1 g to 10 g.

In the experiment, a series of sine vibration waves with various vibration frequencies was applied to the accelerometer. When the fiber length $L$ was 66 mm, the applied range was from 8 to 60 Hz, while it converted to 8-35 Hz when the fiber was shortened to 45.5 mm. Curves in Figure 3.4(a) present the wavelength shifts of the FBGs in core 1, 2, 4 and 6 in time domain, at vibration frequency $f$ of 40 Hz, vibration orientation $\theta_v$ of 90° and acceleration value $a$ of 10 g. During the test, the acceleration was increased from 0.2 g to 10 g for each frequency. From the results, it can be observed that the FBGs in core 2 and 4 experience an opposite wavelength shift since the neutral plane is located in between them, while it remains the same between core 4 and 6, since they are located at the same side of the neutral plane which is different from core 2, under a vibration orientation of 90°. In addition, amplitude of the wavelength shift is dependent on the strain $\varepsilon_i$ applied to each FBG during vibration, which is proportional to the distance $D_i$ (i.e. $i$ = 2 and 4) from the core of interest to the neutral plane, as shown in Figure 3.3(a). When the vibration orientation is set to be 90°, $D_4$ and $D_6$ have the same value due to their angular positions. As a result, they share a similar curve in the time domain waveforms. In contrast to the vibration responses of the outer cores, FBG inscribed in the central core shows insensitivity to vibration because it lies on the neutral plane. Figure 3.4(b) demonstrates the fast Fourier transfer (FFT) spectra of the time-domain results shown in Figure 3.4(a). The measured frequency matches well with the excited frequency from the signal generator. Furthermore, the maximum wavelength shifts as a function of the applied accelerations are plotted for the scenario where, $L = 45.5mm$, $f = 40Hz$ and $\theta_v = 90^\circ$, and the results are shown in Figure 3.4(c). Slopes of the linear responses represent the measurement sensitivities under this condition for the four cores, which are 0.17 pm/g, 111.51 pm/g, 50.78 pm/g and 54.11 pm/g for core 1, 2, 4 and 6, respectively. Similarly, Figure 3.5 displays the vibration information of the FBGs in core 1, 2 ,4 and 6 at $f$ of 20 Hz, $\theta_v$ of 90° and $a$ of 10 g when $L$ was 66 mm, with the sensitivity of 0.27, 136.48, 63.58 and 67.55 pm/g for core 1, 2, 4 and 6, respectively. It is noted that, there is slight difference between the sensitivity for core 4 and 6, which may result from the installation error when mounting the fiber on the shaker, possibly due to a minute tilt of core 2, 1 and 5 which are supposed to be horizontal.

In order to further investigate the performance of the accelerometer, the sensitivity-frequency response was considered, which can reflect the resonance frequency and the flat response range. Basically, the free-fiber length $L$ can influence the resonance frequency significantly as the additional weight of the fiber functions as the inertial mass. The responses for three different $L$, i.e. 66, 45.5 and 25 mm, were characterized accordingly. The length between the grating end and the fixed point was kept at 2 mm for consistency during all the tests, as shown in Figure 3.3(b), and $L$ was shortened by cutting the free-fiber end.

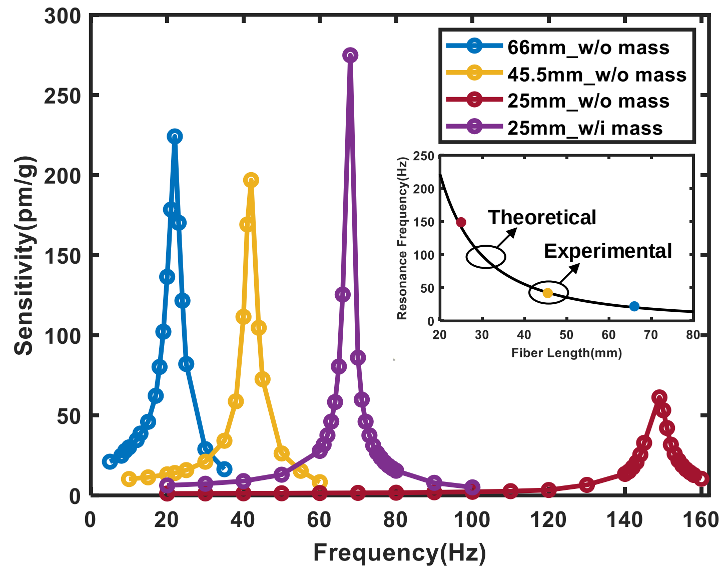


Figure 3.6. Sensitivity-frequency responses of the FBG in core 2 when $\theta_v$ = 90°, $L$ = 66, 45.5 and 25 mm with or without a glue mass. Inset shows the theoretical resonance frequencies under different fiber lengths.

Figure 3.6 displays the vibration sensitivity versus the exciting frequency for the FBG in core 2 when $\theta_v$ is 90° under different $L$. When $L$ is 66 mm as shown in the blue curve, a resonance frequency of 22 Hz appears in the range from 5 to 35 Hz, with a peak sensitivity of 224.1 pm/g. To increase the resonance frequency, $L$ was shortened to 45.5 and then 25 mm. As a result, the resonance frequency appears at 42 and 149 Hz, with the peak sensitivities reduced to 196.9 and 61.19 pm/g, respectively.

Meanwhile, theoretical resonance frequencies under different fiber lengths are plotted as shown in the inset in Figure 3.6, together with the experimental results represented in corresponding colors. It is clearly observed that the experimental results of the resonance frequency measurements match well with the theoretically obtained results. However, there is a tradeoff between the sensitivity and the resonance frequency, which can be tuned according to the requirement of the application. One approach to increase the sensitivity at a relatively high frequency is to attach additional mass on the end of the free-fiber. As a demonstration, a small amount of glue was attached to the end of the free-fiber to increase the weight of the inertial mass. The sensitivity curve under same conditions under $L = 25mm$ condition is plotted in Figure 3.6, which has a resonance frequency of 68 Hz and a peak sensitivity of 274.8 pm/g.

## 3.4 Orientation Discrimination

The capability of orientation discrimination for the proposed two-dimensional vibration sensor is investigated by applying different accelerations with various orientations. Due to the fact that wavelength shift is caused by the vibration-induced strain to individual FBG, the maximum shift relies on the distance from fiber core to the neutral plane, as shown in Figure 3.3(a). Typically, the distance for a particular core (i.e. $D_i$) changes with the vibration orientation, signifying that the sensitivity varies periodically with the change of orientation. When the fiber is rotated in different orientations over a range of 0-180°, $D_2$, $D_4$ and $D_6$ are different. Thus, the strain applied in these FBGs would change accordingly with different orientations, which can be distinguished by monitoring the wavelength shifts in the outer cores. Figure 3.7 shows the dependence of vibration sensitivity on the orientation of core 2, 4 and 6 over a range of 0-180° in steps of 10°. Owing to the feature of vibration in one direction, the orientations with π differences are identical within 360° (e.g. 30° and 210°). Therefore, the orientation within 180° covers the entire two-dimensional plane. Figure 3.7(a) demonstrates the measured sensitivities with respect to the various orientations under the condition of $L$ = 66 mm and $f$ = 20 Hz, whereas Figure 3.7(b) shows the results for the case of $L$ = 45.5 mm and $f$ = 40 Hz. As expected, at a certain orientation, the sensitivity is different for each cores, i.e., core 2 and 4. There is a phase shift between the results of core 2 and 4, i.e. 60°, which is the same as the geometrical angle between these two cores and the central core.

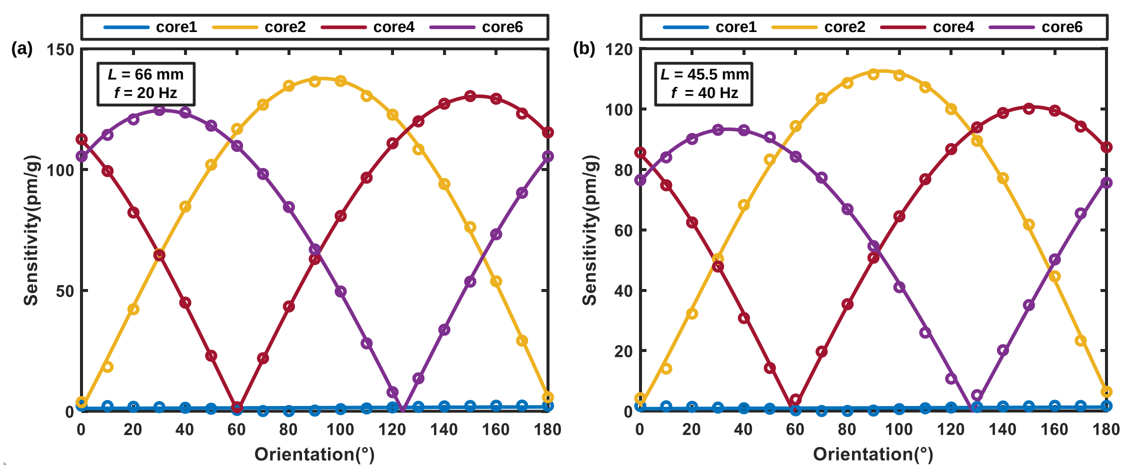


Figure 3.7. Orientation dependence of the sensitivities of FBGs in core 1, 2, 4 and 6 under different conditions. (a) $L$ = 66 mm and $f$ = 20 Hz; (b) $L$ = 45.5 mm and $f$ = 40 Hz.

It is possible that the same wavelength shift can be measured for the cases with different accelerations and orientations. As for an unknown vibration, information on its frequency, acceleration as well as the orientation should be extracted simultaneously from a single accelerometer by detecting the wavelength shifts of the FBGs. It is easy to obtain the frequency by conducting the FFT from the time-domain wavelength shifts. Then the acceleration can be obtained by referring to the calibrated sensitivities in Figure 3.7 if the orientation is known in advance. According to Equation (3.3), vibration orientation $\theta_v$ can be computed from the maximum wavelength shifts of two FBGs and their relative positions. Figure 3.8 shows the results of the orientation discrimination for the scenario of $L = 45.5mm$ and $f = 30Hz$. The fitting line of the experimental results is plotted, together with the measured values under different vibration orientations. It can be seen that the measured orientation values stay consistent with the set values. Different accelerations from 1 g to 10 g at certain orientations are characterized, with the result under 60° shown in the inset. The error bars represent the orientation accuracy, which is defined by the absolute difference between the set values and the reconstructed values. Results show that the vibration direction can be achieved regardless of the acceleration, with accuracy ranges from 0.127 to 2.888° in 0-180° range, depending on the accelerations. From the magnified figure, a relatively low accuracy is found at high accelerations, which may be attributed to the fact that the free-fiber is slightly away from the vibration plane. However, it is insignificant for small accelerations. For a certain orientation value, e.g. 60°, the measured one is supposed to be the same. However, it is noted that there is an offset between the ideal and the measured ones obtained from the fitting line, which is calculated to be 1.75°. The offset value is probably caused when mounting the accelerometer to a certain orientation (e.g. 0°), which can be avoided if the mounting process is precisely controlled.

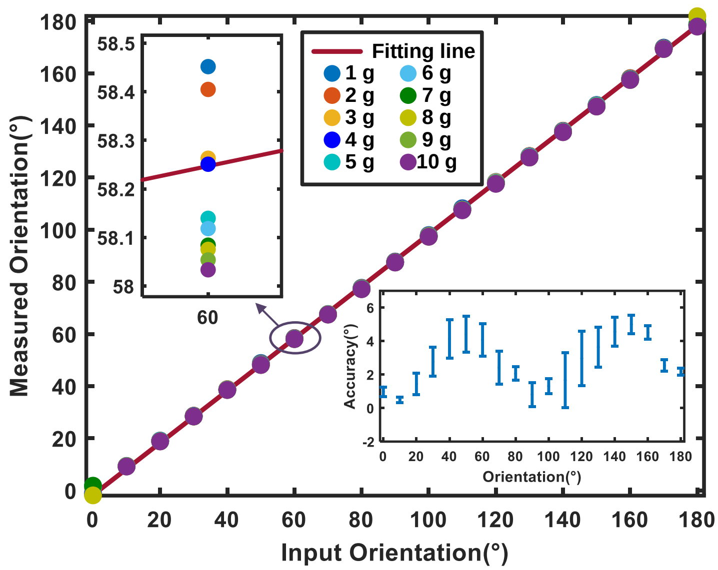


Figure 3.8. Input and measured orientation values under specific orientations from 0 to 180° when $L$ = 45.5 mm and $f$ = 30 Hz. Inset shows the corresponding accuracy ranges.

Besides, the orientation reconstruction performance was also investigated under different sets of the aimed cores when fiber length was set to 66 mm. For example, as shown in Figure 3.9(a), the accuracy ranges from 0.01 to 2.789° for core 2 and core 4 (set 1), and 0.01 to 2.963° for core 2 and core 6 (set 2). Moreover, various accelerations from 1 to 10 g were applied to the sensor under each orientation. Figure 3.9(b) shows the measured orientations under different accelerations when the actual vibration orientation is set to be 20°. It is noted that both groups of the outer cores can distinguish the orientation well, while lacking any obvious difference in the reconstructed orientations under a specific acceleration.

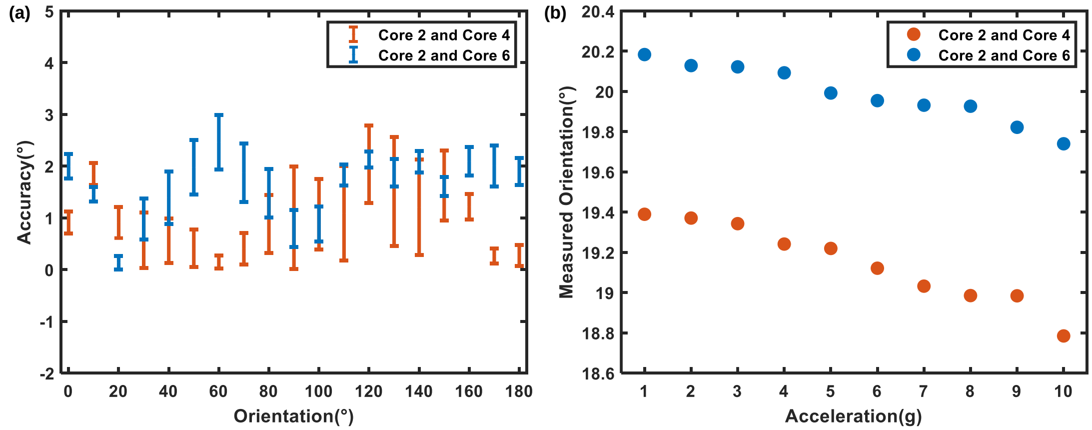

Figure 3.9. (a) Orientation accuracy under different combinations of outer cores when fiber length $L$ = 66 mm. (b) Measured orientations applied with different accelerations when $\theta_v$ = 20° under different combinations of outer cores.

## 3.5 Summary

In this chapter, a short description of the existing structures for both one-dimensional and two-dimensional vibration sensors is presented. Previous research studies, lack detailed information on vibration including the vibration direction, acceleration and frequency when source of vibration is unknown. The proposed two-dimensional vibration sensor is designed to distinguish the value of orientation and acceleration simultaneously, based on the FBGs inscribed in the MCF. A seven-core MCF with 10-mm long FBGs inscribed in the cores is used as an inertial mass to be the accelerometer probe, which is immune to temperature fluctuations since the central core stays on the neutral plane at all times during vibration. The maximum resonance frequency is measured at 149 Hz, which can be optimized by adjusting the free-fiber length and weight. Through monitoring the wavelength shifts of only three cores, including the central and two outer cores which are not aligned in a straight line, vibration orientation can be obtained with an error range of 0.127 to 2.888°, which can be improved when orientation-sensitive factors are considered. Furthermore, different outer cores are chosen for the orientation reconstruction, with errors ranging from 0.01 to 2.789° and 0.01 to 2.963° under different combinations. The similar accuracy makes the sensor more reliable in differentiating the orientation. With the use of this structure, orientation information as well as the acceleration can be obtained in a single fiber concurrently. Furthermore, the compact size of the sensor is beneficial for orientation-sensitive acceleration measurement applications.

# Chapter 4 Two-Dimensional Inclinometer

## 4.1 Overview on Fiber-Optic Inclinometers

Inclinometers (tilt sensors) are important sensing devices widely used in many industrial applications, such as aircraft flight control [111], ground subsidence detection [112], and monitoring of slope deformation [113]. In order to detect tilt angles, various kinds of techniques have been proposed to develop these inclinometers based on mechanical, convection, and magnetics approaches. Although, mechanical inclinometers perform well under small tilt motion detection conditions, the measurement range is limited and the folded pendulum structure is fragile [114]. In contrast, the convective inclinometers have an increased inclination measurement range, but are thermally sensitive, which decreases the accuracy of the sensor [115] and the magnetic inclinometers which are insensitive towards temperature, are restricted to operation in electromagnetic environments [116]. As a result, there is a need to investigate inclinometers based on a different technique to overcome these constraints.

Generally, fiber-optic based tilt detection is carried out through strain measurements in a fiber gauge, which is introduced by an angular deflection of the sensor body from a reference plane or a line. In practice, there are two angles that determine a tilt, namely the azimuthal angle in the axial plane and the inclination angle in the vertical plane. Based on the discrimination of these tilt angles, one-dimensional or two-dimensional inclinometers have been proposed.

One-dimensional inclinometers are only sensitive to the inclination angle. For example, Chen et al. has reported a SMF based tilt sensor with an FBG embedded in an aluminum box to compensate the temperature-induced wavelength shifts [117]. However, the information of the azimuthal angle is unknown. On the contrary, two-dimensional inclinometers are considerably practical as they can measure two tilt angles, simultaneously. The practicality of an inclinometer in a real-world application relies on its capability of retrieving two different angles simultaneously, under a random circumstance where the tilt direction is unknown. Accordingly, several two-dimensional tilt sensors have been demonstrated with different measurement ranges and accuracies. In 2004, Guan et al. reported a pendulum-based inclinometer with two pairs of FBGs, where each pair was assigned to detect inclination in one of the two orthogonal dimensions, through the measurement of their wavelength shifts [118]. The experiment was conducted by changing the inclination in one direction while the other direction remained unchanged. In 2009, Miller et al. implemented a cantilever-based tilt sensor with a MCF, by monitoring bend-induced strain through interferometric interrogation [119]. The sensor showed an inclination-sensitive response over a wide range, and one of the inclinations was able to be calibrated when the other was fixed. In 2016, Chiang et al. introduced a two-dimensional tilt sensor using two etched chirped FBGs [120]. Results of the wavelength response were dependent on the aforementioned two angles, however, the information of tilt is not apparent. As a result, distinguishing inclination and azimuthal angles simultaneously in an inclinometer under an unknown scenario remains challenging. In other words, with the use of a two-dimensional inclinometer, both the inclination and azimuthal angles could be reconstructed under random circumstances.

## 4.2 Principle of the Two-Dimensional Inclinometer

The principle of an FBG-based inclinometer is based on monitoring of the wavelength shifts of the FBGs induced by a tilt. The aimed fiber is the same as the one used in Chapter 2, together with the fabrication process for the FBG inscribed in the fiber. The grating length was 10 mm and a pitch of 1048.16 nm. Schematic illustration of the inclinometer with FBGs inscribed in the MCF is shown in Figure 4.2. During the tilt measurement, the sensor body is shifted away from its original position, in the vertical direction. Two angles, including the azimuthal angle $\varphi$ and the inclination angle $\theta$ contribute towards the tilt measurement together. The former is defined as the angle between the tilt orientation and the neutral plane, while the latter is defined as the angle between the tilt and vertical direction, which are illustrated in Figure 4.1(a) and Figure 4.2, respectively.

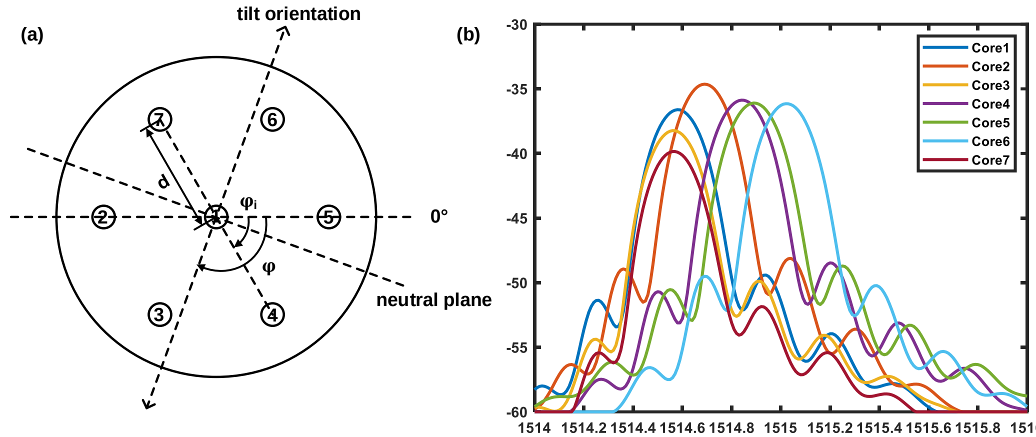


Figure 4.1. (a) Definition of the geometrical parameters from the cross-section of the MCF and (b) reflection spectra of the FBGs inscribed in fiber cores.

After FBG inscription, the MCF was connected to a 1-to-7 fan-out device (YOFC) with the help of a polarization maintaining fiber fusion splicer (Fujikura, LZM-100). As a result, FBGs in each core can be monitored individually during the experiment. An interrogator (Micron Optics, sm130) with a resolution of 1 pm was used to analyze the reflection spectra, which are shown in Figure 4.1(b). In general, the Bragg wavelength of each core is slightly different from each other, due to the non-uniform UV exposure which occurs as a result of the different spatial distribution of the cores [94]. In the experiment, three of the seven cores, including the central core 1 as well as two outer cores 2 and 4 were chosen for the tilt measurement.

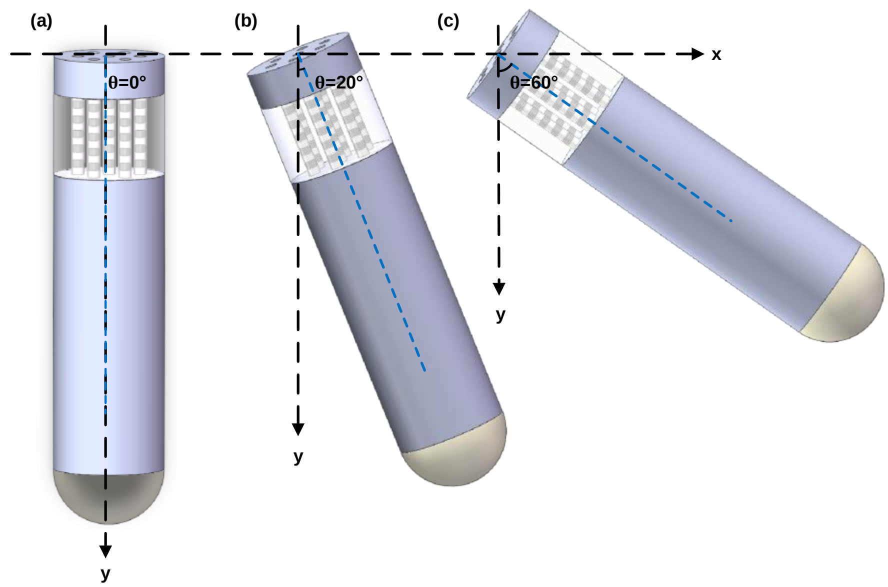


Figure 4.2. Schematic illustration of the inclinometer under different inclinations. (a) $\varphi$ = 0° and $\theta$ = 0°, (b) $\varphi$ = 0° and $\theta$ = 20°, and (c) $\varphi$ = 0° and $\theta$ = 60°.

During the tilt measurement process, the FBGs in all the fiber cores experience different strain induced wavelength shifts. For the outer cores, the Bragg wavelengths show a blue shift when they are compressed, and a red shift when stretched. However, the FBG in the central core is insensitive towards bending since it is in the neutral plane. As a result, the central core can be used for temperature compensation. The wavelength shift $\Delta\lambda$ of an FBG in core $i$ can be described as,

$$\Delta\lambda_i = (1 - p_e)\lambda_i \cdot \frac{d}{R} \cdot \sin(\varphi + \varphi_i), \tag{4.1}$$

where $\lambda_i$ is the Bragg wavelength of core $i$, while $p_e \approx 0.22$, is the effective photo-elastic coefficient. Furthermore, $\varphi_i$ represents the angular position of core $i$ with respect to the neutral plane, and $R$ is the tilt-induced bending radius. The designed inclinometer is based on a cantilever structure, where a small mass is attached to the free end of the sensor body while the other end is fixed. The FBGs are located near the fixed point, as depicted in Figure 4.2. When the fiber is tilted, the free-fiber end moves away from the vertical direction while the other end remains fixed. Under this situation, $R$ is composed of two parts, namely the mass-induced $R_{Mass}$ and free-fiber-induced $R_{Fiber}$, which are described in Equations (4.2) and (4.3), respectively [121],

$$R_{\mathrm{Mass}} = \frac{EI}{mg\sin\theta \cdot \left(x_g - L\right)}, \tag{4.2}$$

$$R_{\mathrm{Fiber}} = \frac{EI}{w \cdot \left(Lx_g - \frac{1}{2}x_g^2 - \frac{1}{2}L^2\right)}. \tag{4.3}$$

$E$ is the Young's modulus of the fiber, and $I$ is the second moment of the cross-sectional area, which is defined as $\pi D^4/64$. $L$ is the length of the free-fiber, and $x_g$ represents the distance between the grating and the fixed point. $w$ is the fiber weight per unit length and $m$ is the weight of the applied mass, while $g$ = 9.8 m/s$^2$ is the gravitational acceleration. As a result, the tilt-induced Bragg wavelength shift in core $i$ can be expressed by Equation (4.4),

$$\Delta\lambda_i = \left(1 - p_e\right)\lambda_i \cdot \left(\frac{d}{R_{\mathrm{Fiber}}} + \frac{d}{R_{Mass}}\right) \cdot \sin\left(\varphi + \varphi_i\right). \tag{4.4}$$

The Bragg wavelength shifts are related to both $\theta$ and $\varphi$. When wavelength shifts in two outer cores are considered, for example, core $i$ and core $j$, the azimuthal angle $\varphi$ can be described as,

$$\varphi = \tan^{-1}\left( \frac{\frac{\Delta\lambda_i}{\lambda_i}\sin\varphi_j - \frac{\Delta\lambda_j}{\lambda_j}\sin\varphi_i}{\frac{\Delta\lambda_j}{\lambda_j}\cos\varphi_i - \frac{\Delta\lambda_i}{\lambda_i}\cos\varphi_j} \right). \tag{4.5}$$

From Equation (4.5) it is apparent that the phase between $\varphi_i$ and $\varphi_j$ can be any value except $\pi$, which means the chosen two cores should not be aligned in a straight line with the central core. Consequently, once the orientation of $\varphi$ is determined, $\theta$ can be obtained via Equations (4.5) and (4.4), which can be deduced as,

$$\theta = \sin^{-1}\left[ \left( \frac{\Delta\lambda_i}{\lambda_i}\frac{1}{1-p_e}\frac{1}{\sin\left(\varphi+\varphi_i\right)} - \frac{d}{R_{Fiber}} \right) \times \frac{EI}{dmg\left(x_g - L\right)} \right]. \tag{4.6}$$

In other words, knowing the value of $\varphi$ and the wavelength shift in a specific core, $\theta$ can be successfully determined. Hence, both $\varphi$ and $\theta$ can be obtained simultanesouly under any tilting condition by detecting the Bragg wavelength shifts, indicating that the inclinometer has the capability of distinguishing the tilt in a two-dimensional range.

## 4.3 Theoretical Model of the Two-Dimensional Inclinometer

Before experimental verification, the performance of the sensor was simulated based on the parameters of the seven-core MCF. The mass weight $m$ chosen in the simulation was 10 $mg$, and $E$ of the MCF was 73 $GPa$. The free-fiber length $L$ was 73 $mm$, with $x_g$ set to 5 $mm$. The simulation results of the Bragg wavelength shifts obtained with respect to the azimuthal angle and inclination angle are shown in

Figure 4.3 and Figure 4.4, respectively where the former indicates the response of the wavelength shift versus $\varphi$ for core 2 and 4, when $\theta$ varies from 0 to 90° in steps of 10°. Figure 4.4(a) and Figure 4.4(b) show the response of the wavelength shift versus $\theta$ for core 2 and 4, when $\varphi$ varies from 0 to 330° in steps of 30°. In this simulation, $\varphi_2$ and $\varphi_4$ are $\pi$ and $5\pi/3$, respectively which is based on the geometric position of core 2 and 4, as illustrated in Figure 4.1(a). However, the angular position is adjustable in real applications by choosing any two cores. This initial angle information can also be verified by the initial phase of the response curves as shown in Figure 4.3.

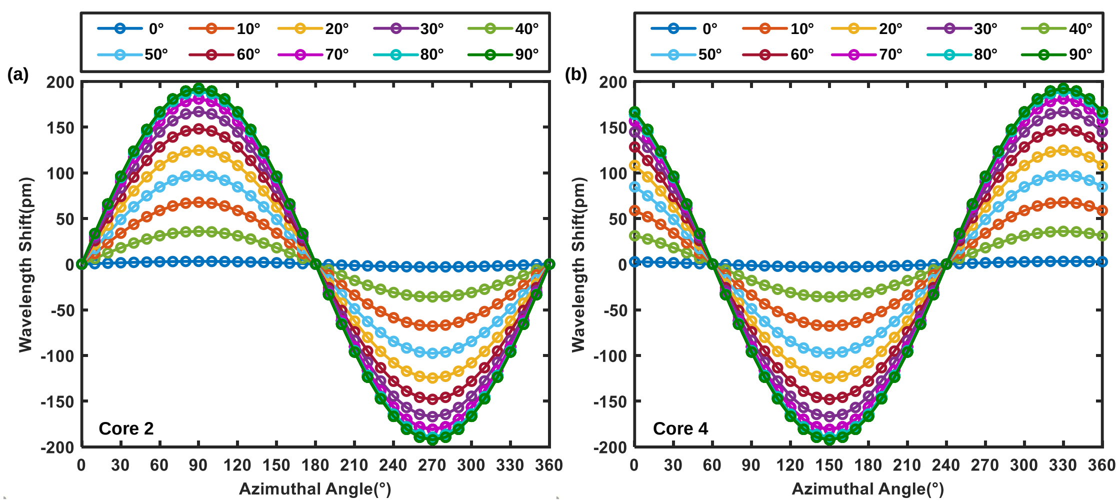


Figure 4.3. Simulation results of wavelength shift versus $\varphi$ for (a) core 2 and (b) core 4 with $\theta$ over a range from 0 to 90° in steps of 10°.

From Figure 4.3, it can be observed that there is a phase difference of 60° in the responses of the two cores, which is identical to their geometric angle with respect to the 0° plane, as shown in Figure 4.1(a). Particularly, the phase of the wavelength shift curve in Figure 4.3(a) is influenced by the angular position of a specific core.

According to Figure 4.3, it is evident that when $\theta$ is 0°, the wavelength shift is zero for all of the azimuthal angles ($\varphi$), representing the initial vertical direction of the inclinometer. For a specific $\varphi$, the wavelength shift increases with increasing $\theta$. Figure 4.4 describes the wavelength shift as a function of $\theta$, which shows a sinusoidal response. It is observed that the inclinometer is less sensitive at large inclination angles. The simulation results demonstrate that the Bragg wavelength shift of the FBGs is dependent on both $\varphi$ and $\theta$, denoting that the two-dimensional inclinometer is sensitive to two angular directions.

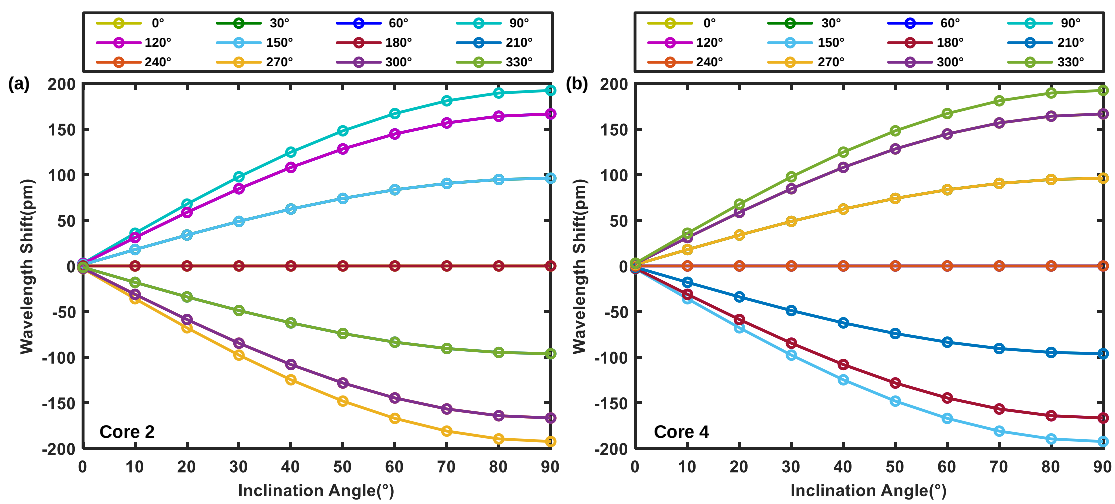

Figure 4.4. Simulation results of wavelength shift versus $\theta$ for (a) core 2 and (b) core 4 with $\varphi$ over a range from 0 to 330° in steps of 30°.

In order to improve the sensitivity of the proposed inclinometer, different parameters of the MCF were investigated to optimize the sensing performance. According to Equation (4.4), it is apparent that the wavelength shift is closely related to three main parameters, i.e. the pitch $d$, Young's modulus $E$ and the weight of the mass $m$. Therefore, the sensitivity can be enhanced by adjusting these parameters. Simulation results of wavelength shift versus the azimuthal angles $\varphi$, under different parameters are summarized in Figure 4.5, under the condition that $\theta$ was fixed at 60° while the other parameters were maintained the same as described in the first paragraph of this section. Figure 4.5(a) describes the response of the wavelength shift with $d$ changing from 10 to 50 $\mu m$, in which the wavelength shift increases when $d$ is increased, signifying that the sensor is more sensitive when the pitch is larger. In order to investigate the effect of the material of the fiber on the sensitivity of the FBG, two materials with different Young's moduli namely, borosilicate and silica glass were taken into account. Results from Figure 4.5(b) demonstrate that as $E$ increases, the FBG is less sensitive, denoting that an inclinometer with a softer material can have a higher sensitivity. In addition, the response of the wavelength shift under different $m$ values varying from 5 to 25 $mg$, is shown in Figure 4.5(c). Evidently, the wavelength drift becomes larger with increasing weight, which is caused by the larger mass-induced strain. After comparing the obtained results of the wavelength shift under the influence of these three parameters at a certain azimuthal angle range, it is revealed that $m$ dominates the wavelength shift response exhibiting the maximum wavelength shift at the same azimuthal angle. The comparison result of the wavelength shift under specific parameters are concluded in Figure 4.5. This indicates that the most effective way to improve the performance of the inclinometer is by increasing the weight of the applied mass.

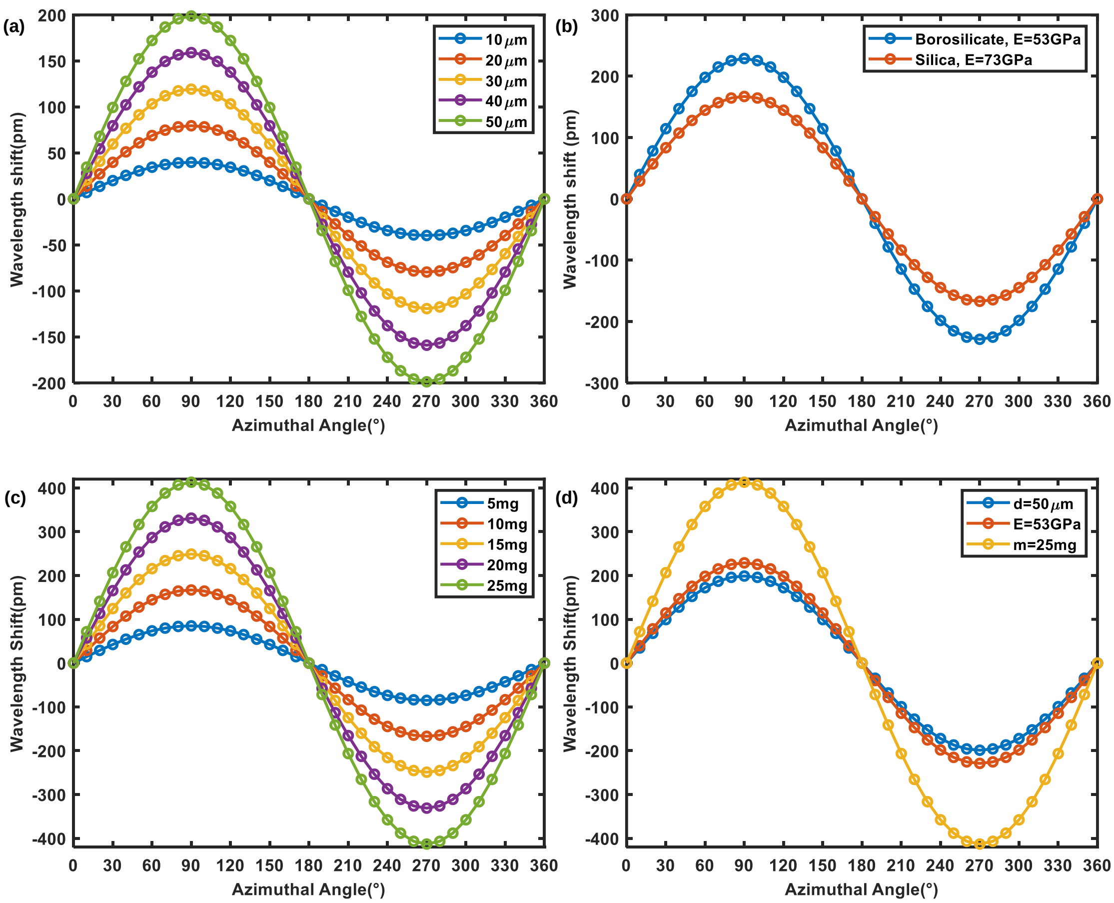


Figure 4.5. Simulation results of wavelength shift versus $\varphi$ with $\theta$ fixed at 60° under varying conditions of (a) pitch $d$, (b) Young's modulus $E$, and (c) weight of mass $m$. (d) Wavelength shift comparison among three parameters.

## 4.4 Characterization of the Two-Dimensional Inclinometer

The schematic setup of the two-dimensional inclinometer is depicted in Figure 4.6, where Figure 4.6(a) illustrates the details of the two-dimensional inclinometer. A fiber rotator (Thorlabs, HFR007) was used to tune the tilt orientation ($\varphi$) in the range from 0 to 360°, while a 6-axis kinematic mount (Thorlabs, K6XS) was used to adjust $\theta$ from 0 to 90°. Based on Figure 4.6(b), the seven-core MCF inscribed with FBGs was firstly spliced to a 1-to-7 fan-out device, and the multiple SMF ends, corresponding to core 1, 2, 4, and 6, were connected to an interrogator with a resolution of 1 pm and a sampling rate of 2000 Hz. As a result, the MCF functioning as a sensing probe can detect a tilt within a two-dimensional range. In this experiment, the used fiber length was 73 mm and the distance between the grating and its fixed point was 5 mm, which are as same as the simulation parameters. The weight of the mass $m$, was 10 mg. During the experiment, tilt measurements were carried out under different azimuthal and inclined orientations in two dimensions.

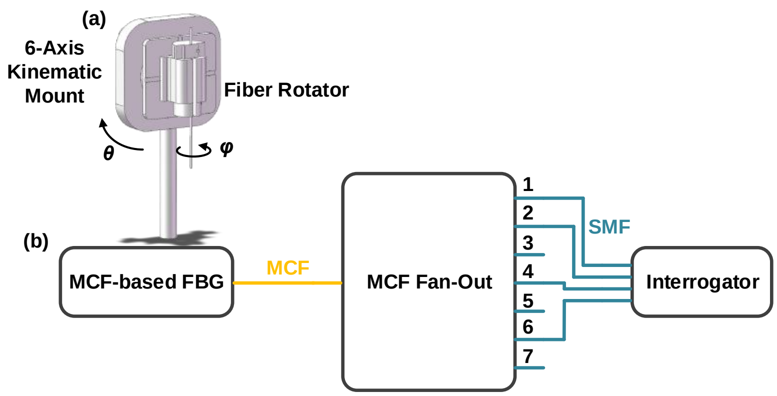


Figure 4.6. (a) Illustration of the tilt sensor, including a fiber rotator and a 6-axis kinematic mount introducing $\varphi$ and $\theta$ respectively, to the MCF inscribed with FBGs. (b) Schematic setup of the two-dimensional inclinometer system used for the tilt measurement.

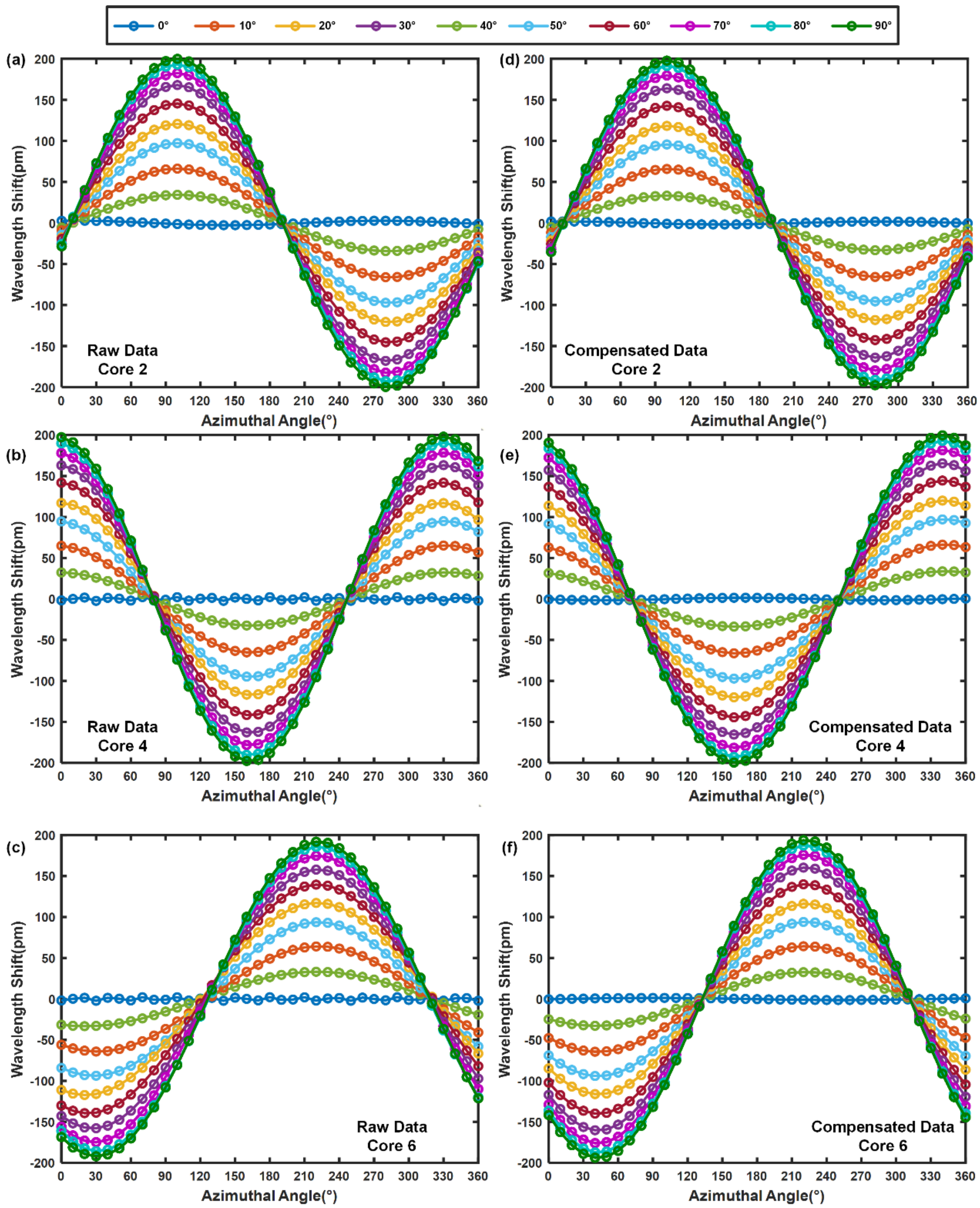


Figure 4.7. Raw data of the Bragg wavelength shifts in (a) core 2, (b) core 4, and (c) core 6, and self-compensated data of the Bragg wavelength shifts in (d) core 2, (e) core 4, and (f) core 6, with $\varphi$ varying from 0 to 360° in steps of 10°, and $\theta$ varying from 0 to 90° in steps of 10°.

The experimental results are shown in the Figure 4.7 and Figure 4.8. Raw data of the Bragg wavelength shifts are shown in Figure 4.7(a)-(c), representing the responses of core 2, 4 and 6, respectively. The azimuthal angle $\varphi$ varies from 0 to 360° in steps of 10°, and the inclination angle $\theta$ varies from 0 to 90° in steps of 10°. Due to the regular variation of the tilt angle, the shape of the wavelength shift curve is sinusoidal. Noticeably, there is a 60° phase shift between two different cores, which is the same with the angular difference of the fiber cores. However, it is clearly observed that the period of each curve in each figure within Figure 4.7(a)-(c) is slightly different, which is caused by the offset of the sensor body during the tilt measurement. Consequently, the response in core 1 can be used for the offset compensation, as shown in Figure 4.7(d)-(f). Considering the results in Figure 4.7(d) and Figure 4.7(e), there is a phase shift in each core when compared with the simulation results in Figure 4.3, e.g., $\pi/18$ for core 2, which can be used to obtain the actual angular position of the fiber core. As a result, in the experiment $\varphi_2$ and $\varphi_4$ are $17\pi/18$ and $29\pi/18$, respectively. Apart from the phase of the wavelength shift curves, the values of the responses are in accordance with that of the simulation results, demonstrating high reliability and good repeatability can be achieved with the proposed inclinometer. The maximum sensitivity of $\varphi$ is 3.24 pm/°, with the fitting range from 150° to 210°, and an $R^2$ value of 0.9989. Similarly, Figure 4.8 illustrates the compensated experimental results of the Bragg wavelength shift as a function of $\theta$, while $\varphi$ varies from 0 to 330° in steps of 30°. A maximum sensitivity of 3.2208 pm/° is obtained, within an angle variation from 0 to 30°, with an $R^2$ value of 0.9991. After accounting for the resolution of the interrogator (1 pm), the resolution of these two angles is 0.31°. It is notable that the sensitivity can be largely improved through enhancing the weight of the mass. Furthermore, other Bragg wavelength shifts detected by core 1, such as temperature fluctuations, can also be compensated which makes the system to be temperature insensitive and more reliable.

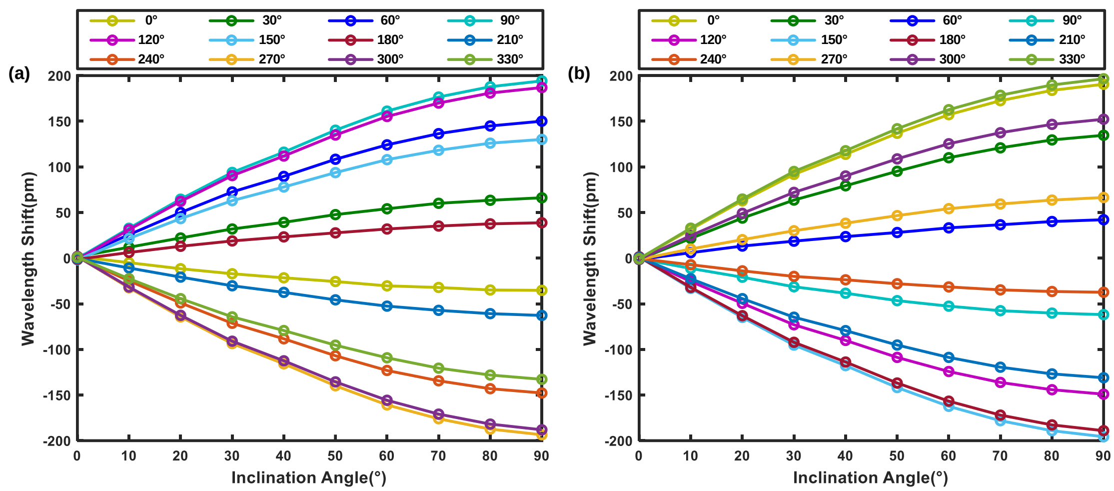


Figure 4.8. Compensated experimental results of wavelength shift versus $\theta$ for (a) core 2 and (b) core 4 with $\varphi$ in the range from 0 to 330° in steps of 30°.

## 4.5 Orientation Discrimination

The main functionality of a two-dimensional inclinometer relies on its capability of angle detection in two dimensions. During measurement, the tilt angle of an FBG-based inclinometer is determined by the wavelength shift of the FBG(s). However, it is possible to obtain the same wavelength shift under two different scenarios. Therefore, distinguishing two different angles simultaneously, is necessary in a tilt measurement. According to Equation (4.5), the azimuthal angle $\varphi$ can be calculated through the maximum wavelength shift of the two FBGs and their relative positions. Figure 4.9 shows the theoretically results of $\varphi$ against the reconstructed ones from the measured wavelength shifts at different input angles using the results in core 2 and 4. It can be observed that the measured orientation values remain consistent with the set values over the range from 0 to ±180°. The (0, -180°) and (0, +180°) ranges are determined by the blue and red wavelength shift of a specific FBG in the fiber core. For example, when the measured $\varphi$ is 40°, this means the actual value can be either 40° or 220°. Nevertheless, with the help of Figure 4.7, it is clear that at 40°, a red shift occurs in the wavelength of the FBGs in both the cores, on the contrary to the conditions at 220° which indicates a blue shift in the wavelength of the FBGs. Therefore, $\varphi$ can be determined unambiguously over the range of 0 to 360°.

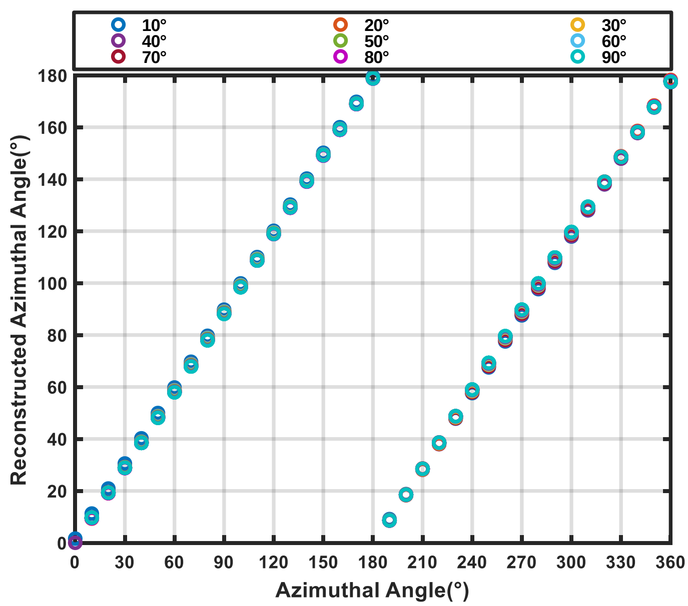


Figure 4.9. Input and measured azimuthal angles at specific orientations from 0 to 360° with the use of wavelength shifts in core 2 and 4.

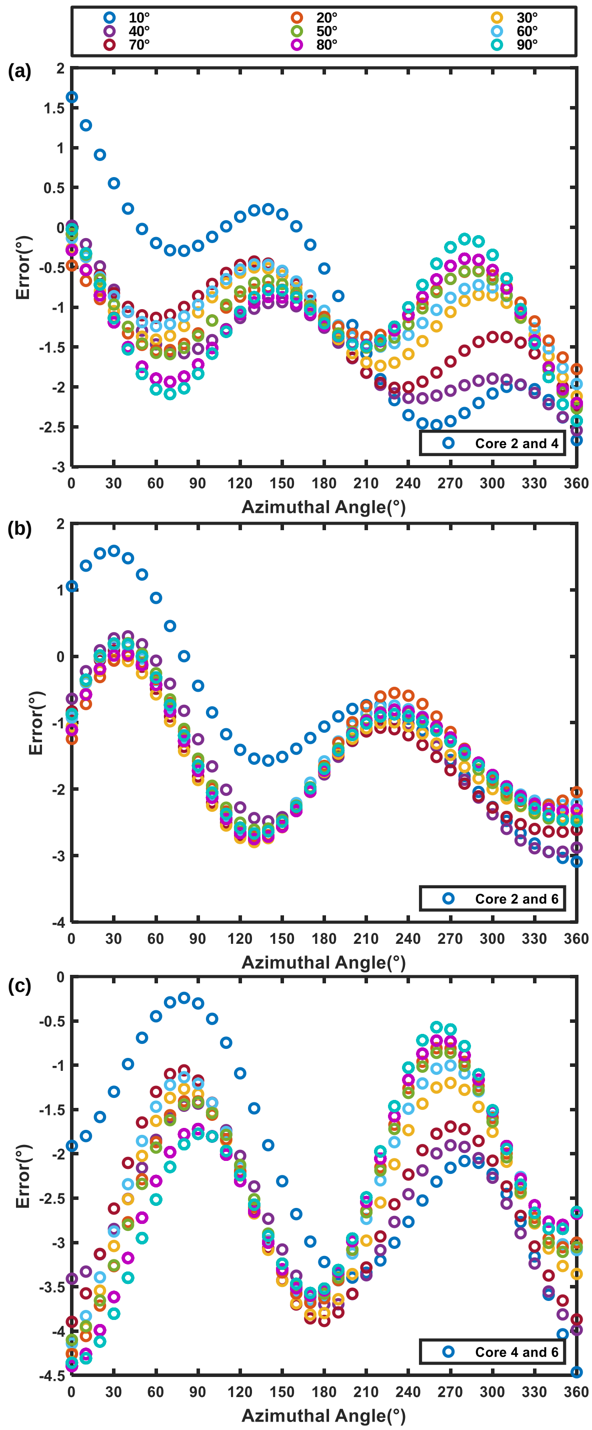


Figure 4.10. Orientation error of azimuthal angle over the range from 0-360°, under three different combinations of the used fiber core, including (a) core 2 and 4, (b) core 2 and 6, and (c) core 4 and 6.

In order to evaluate the performance of the angle reconstruction, the orientation error of $\varphi$ under different $\theta$ values was investigated and is described in Figure 4.10. The measurement error is defined by the difference between the set values and the reconstructed values. Figure 4.10(a)-(c) show the error of azimuthal angle over the range from 0-360° in steps of 10°, under three different combinations of the used fiber core, e.g., core 2 and 4, core 2 and 6, and core 4 and 6, respectively.

The results show that for $\varphi$, the error of the reconstructed angle varies from 0.0056 to 2.668° under the combination of core 2 and 4, while it is 0.0001 to 3.09° when the fiber cores are changed to core 2 and 6, and 0.24 to 4.464° when the fiber cores are 4 and 6. Also, there is a prominent sinusoidal trend in the accuracy at a specific inclination angle, which is caused by the sinusoidal period of the experiment results in Figure 4.7, and the results show that a large error occurs when the sensitivity is relatively low.

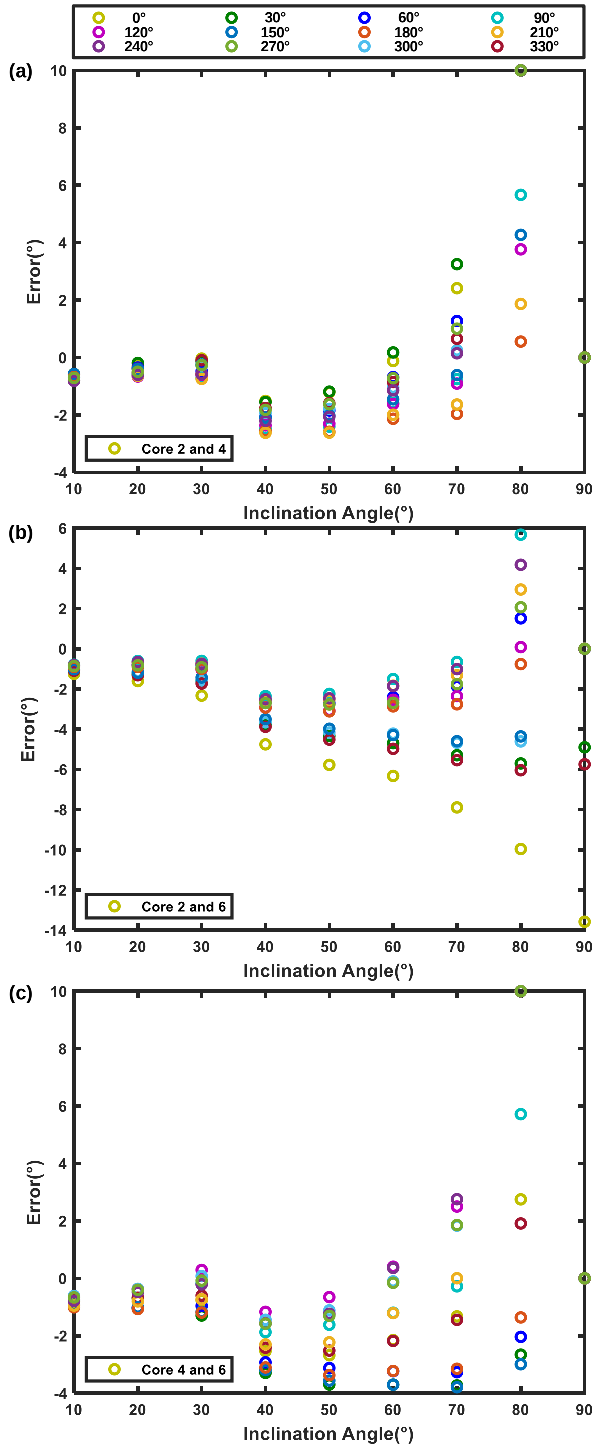


Figure 4.11. Orientation error of inclination angle over the range from 10-90°, under three different combinations of the used fiber core, including (a) core 2 and 4, (b) core 2 and 6, and (c) core 4 and 6.

Once the information of $\varphi$ is retrieved, the value of $\theta$ can be further investigated according to Equation (4.6). The error of $\theta$ is illustrated in Figure 4.11 under three different combinations of the used fiber core, at different $\varphi$ values ranging from 0 to 330° in steps of 30°. It is apparent that inclination angle reconstruction performs well under small inclinations, i.e., 10 to 70°. Large errors occur at large inclination angles due to the relatively low slope in the wavelength shift-inclination angle curve, which corresponds to a relatively small sensitivity. However, this issue can also be resolved through several other methods, such as increasing the weight of the mass, elongating the free-fiber length or by reducing the Young's modulus. The performance can also be improved through changing the parameters of the tilt sensor, such as enhancing the mass weight or increasing the pitch of the fiber. Also, the accuracy in different combinations of the used fiber cores shows consistency. The minimum error in Figure 4.11(a)-(c) is 0.025°, 0.585° and 0.079°, respectively, demonstrating the stable characteristics of the tilt sensor.

## 4.6 Summary

This chapter focuses on the introduction of an FBG-based MCF for two-dimensional inclination measurement. Detection of the actual tilt angle is absent in the existing research of two-dimensional inclination sensors. As a result, the proposed inclinometer is designed with the capability of distinguishing the value of tilt angles in two different planes, including the azimuthal and the inclination angle, under random circumstances. In the design, a 73-mm long seven-core MCF consisting of 10-mm long FBGs inscribed in the cores, together with a free-fiber end mass is utilized as the sensor body of the inclinometer. With the help of the central core, which remains on the neutral plane, the designed sensor is temperature compensated. The achieved sensitivity during the measurement of the angles is 3.24 pm/°, which can be further improved by increasing the weight of the mass, decreasing the Young's modulus, extending the length of the free-fiber, and by varying the pitch of the MCF. Through monitoring the wavelength shifts of three of the seven cores, including the central and two outer cores which are not aligned in a straight line, the azimuthal angle is obtained within the measurement error range of 0.0056 to 2.668° in a 0-360° range, while the minimum error is 0.025° for the inclination angle over a range from 10° to 90°. Furthermore, the sensor is easy to fabricate and has a compact size, allowing it to be incorporated in applications where space is a limitation. The obtained repeatable results of the sensor further ensure its robustness and reliability which is ideal for industrial applications, such as the structural health monitoring and robotic arms.

# Chapter 5 Two-Dimensional Displacement Sensor Assisted with Machine Learning Algorithms

## 5.1 Overview on Displacement Sensors

Displacement is one of the most important parameters in mechanical engineering. The displacement information of objects is crucial in various industrial fields including structural health monitoring [122], biomedical measurement [123] and aerospace applications [124], etc. Due to the capability of precise alignment, displacement sensor is one of the essential methods to achieve accurate positing. Numerous approaches have been proposed to achieve the displacement measurement of different amplitudes with accuracies. However, in order to achieve two-dimensional vector sensing, the direction of displacement turns out to be another essential physical quantity that needs to be measured when developing a position tracking sensor in practical applications, such as robotic arms [125]. It requires the designed sensor to be sensitive to both the amplitude and direction of the applied displacement, simultaneously.

Generally, fiber-optic displacement sensors are developed based on the measurement of deflection induced by fiber bending or stretching. Through monitoring the variation of intensity, wavelength and phase of the optical signal, the displacement performance is analyzed. For example, Dong et al. reported a FBG based displacement sensor with the characteristic of temperature insensitivity [126].

The sensor used an FBG that was glued on the lateral side of a cantilever in a slanted direction, and the displacement was measured by detecting the variation of the bandwidth and the reflected optical power of the FBG. Besides, Rong et al. presented a configuration consisting of the combination of thin-core fiber and FBG for displacement sensing [127]. The structure exploited the core-cladding coupling mechanism, where the coupled intensity was referenced for displacement measurement. Chen et al. proposed a Michelson interferometer based displacement sensor [128]. Through the demodulation of optical path difference between the sensing and reference fiber, the displacement detection was converted to the differential phase measurement. However, the aforementioned sensors can only allow for one dimensional displacement measurement, while the direction information of the displacement was not considered, which hinders it from developing into a position tracking sensor.

In order to obtain the direction information of the displacement, several fiber-optic two-dimensional displacement sensors were reported, with the direction dependency resulted from an asymmetric geometry. For example, Yang et al. introduced a direction-dependent displacement sensor by inscribing gratings in the core and the inner cladding of a multi-cladding fiber [129]. Due to the intensity modulation difference between the two FBGs, displacement induced output optical signal showed direction sensitivity. In addition, Bao et al. demonstrated a displacement sensor by inscribing an eccentric FBG in the core/cladding interface using a depressed-cladding fiber [22], which introduced a cylindrical asymmetry into the fiber. The direction related displacement response was obtained through intensity detection. Although these sensors are displacement direction sensitive, the variation of displacement amplitude in a random direction is unknown. Essentially, all the aforementioned sensors are not able to retrieve the displacement direction and amplitude simultaneously. The displacement sensor response is caused by the displacement induced fiber bending. In order to retrieve the displacement information during the displacement measurement process, the relationship between the displacement and corresponding fiber bending is kept linear, which limits the measurement range within several micrometers (dependent on the length of the tested fiber). In addition, the reconstruction performance is mainly dependent on the accuracy of the corresponding theoretical model, where small variation may result in large error for each retrieval. Moreover, the system error is inevitable during the setup process, which may introduce larger error in each calculation process. To improve the displacement performance, an accurate method for the amplitude and direction reconstruction should be investigated.

## 5.2 Machine Learning in Fiber-Optic Sensors

Recently, different machine learning algorithms have been used to improve estimation accuracy in optical fiber sensors. For example, in distributed optical fiber sensing systems, researchers utilized algorithms such as support vector machine

(SVM), principal component analysis (PCA), artificial neural networks (ANN), convolutional neural network (CNN), etc. to extract the Brillouin gain spectrum (BGS) [130-133], which was usually obtained using Lorentzian curve fitting (LCF) [133]. However, the accuracy of the extraction of BGS with the LCF approach is influenced by the fitting parameters. These machine learning algorithms enhance the sensing performance with an accurate and efficient BGS extraction, producing better performance over the conventional fitting method. In addition to the distributed optical fiber sensing, the point-based optical fiber sensing systems are also benefited from the machine learning tools. For instance, the Gaussian process regression (GPR) was introduced to an FBG-based temperature sensor for accurate temperature calculation [134]. It provided a direct mapping between the temperature and FBG spectrum to improve the detection accuracy, while conventional fitting methods were largely dependent on the quality of the FBG spectrum. In particular, there are researches using machine learning algorithms to distinguish multi-parameters in the point-based sensing systems, such as the discrimination of both the magnitude and location of applied normal force in an FBG-based tactile sensor using neural networks [135], and simultaneous measurement for amplitude and direction of the transverse load in a long-period grating (LPG) -based force sensor, where different regression algorithms were investigated for performance comparison [136]. In this work, we applied machine learning to the FBG-based vector displacement sensor for improvement on the measurement range and accuracy.

Various categories of machine learning algorithms are being applied to improve performance in optical sensors, such as neural networks and regression methods. Among them, random forest is regarded as one of the most precise prediction algorithms for classification and regression, due to its capability of modeling complex variable interactions [137]. It consists of a combination of tree predictors where each tree is generated using a random vector sampled independently from the input vector. Random forest algorithm has many advantages such as high efficiency for large datasets, insensitivity to noise or over-fitting, and fewer parameters when compared with other machine-learning algorithms (e.g., ANN or SVM). However, few studies have employed the random forest regression algorithm in fiber-optic sensing, especially for the vector displacement sensor. In this chapter, we demonstrated that the application of random forest algorithm can enhance the performance of vector displacement sensor substantially.

## 5.3 Theoretical Model of the Two-Dimensional Displacement Sensor

As shown in Figure 5.1(a), the seven-core MCF used to develop the displacement sensor is the same as the description in Chapter 3, with diameters for core $D_0$ and cladding $D$ of ~8 and ~150 μm, respectively. The pitch $d$, the distance between two adjacent cores, is ~42 μm. The fiber was loaded in a hydrogen chamber for 3 days under a pressure of 100 bar at a temperature of ~80 °C to enhance the photosensitivity. Then FBGs were inscribed using a 248 nm KrF excimer laser

(Coherent) based on the phase mask (Ibsen Photonics, 1075.23 nm) and beam scanning technique, with grating length of 10 mm and scanning speed of 0.01 mm/s, respectively. After the FBG inscription, the MCF was spliced to a 1-to-7 fan-out device (YOFC, China) using a polarization maintaining fiber fusion splicer (Fujikura, LZM-100).

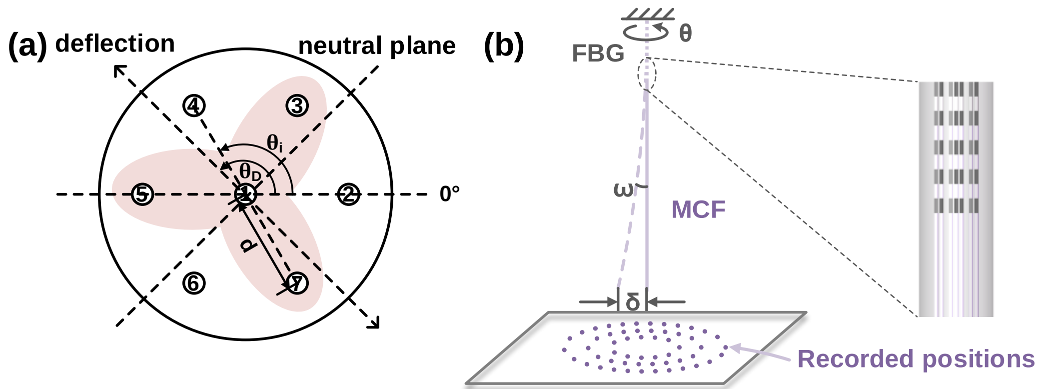


Figure 5.1. (a) Geometrical definition of parameters based on the cross-section of the MCF. (b) Schematic structure demonstration of the FBG and MCF in the displacement sensor design, with the FBGs inscribed in MCF shown in the expanded view.

During the displacement measurement, four of the seven cores, including the central one (i.e., core 1) and three outer ones (i.e., core 3, 5 and 7) are monitored. The applied displacement can be determined by measuring the Bragg wavelength shifts in these cores based on fiber displacement-induced bending. Due to the spatial distribution of the cores, some outer cores are compressed, which introduces a blue shift in the Bragg wavelength while the others are stretched and experienced a red shift. However, core 1 is insensitive to the applied displacement since it lies in the neutral plane, which can be utilized for temperature compensation. As a result, the

Bragg wavelength shift $\Delta\lambda$ in a specific core $i$ can be expressed as [138]

$$\Delta\lambda_i = \left(1 - p_e\right)\lambda_i \cdot \frac{d}{R} \cdot \sin\left(\theta_D + \theta_i\right), \tag{5.1}$$

where $p_e$ representing the effective photo-elastic coefficient is ~0.22 [139], and $\lambda_i$ is the Bragg wavelength of core $i$. When displacement is applied to the MCF, the displacement angle is defined by $\theta_D$ as shown in Figure 5.1(a), where $\theta_i$ indicates the corresponding angular position of each core $i$ with respect to the 0° plane. In addition, *R* represents the displacement-induced bending radius. The designed sensor is based on a cantilever structure, as is shown in Figure 5.1(b), with the displacement $\delta$ applied on the free-fiber end and the other end kept fixed. The discrete points in Figure 5.1(b) represent the recorded displacements, which are the projections of the free-fiber end with different directions and amplitudes. Based on the bending effect at a single FBG group at a short section along the fiber, and using the mechanical model between the displacement-induced bending radius and displacement amplitude, the displacement of an object on a plane can be monitored. The FBGs are located along the sensor body, with the structure shown in the expanded view. During measurement, the free-fiber end is shifted away from its origin position due to the applied displacement. As a result, the displacement-induced bending radius at a given position along the fiber length is defined as [140]

$$R\left(x\right) = \frac{EI}{M\left(x\right)} = \frac{EI}{-F\left(L - x\right)}, \tag{5.2}$$

where $E$ and $I$ are the Young's modulus and the moment of inertia respectively, and $M(x)$ indicates the bending moment at a specific position, which is related to the position $x$, free fiber length $L$ and the applied force $F$ at the free fiber end. Under this situation, the displacement $\delta$ can be expressed by [140]

$$\delta = \frac{FL^3}{3EI}. \tag{5.3}$$

Based on Equations (5.2) and (5.3), the relationship between displacement and bending radius is obtained as follows

$$\delta = \frac{L^3}{3R(x)(x-L)}, \tag{5.4}$$

which indicates that the displacement is dependent on the free fiber length $L$ and position $x$.

As a result, when Bragg wavelength shifts in two of the outer cores are considered, such as core $i$ and $j$, the displacement angle $\theta_D$ can be deduced by Equation (5.5),

$$\theta_D = \tan^{-1}\left(\frac{\frac{\Delta\lambda_i}{\lambda_i}\sin\theta_j - \frac{\Delta\lambda_j}{\lambda_j}\sin\theta_i}{\frac{\Delta\lambda_j}{\lambda_j}\cos\theta_i - \frac{\Delta\lambda_i}{\lambda_i}\cos\theta_j}\right), \tag{5.5}$$

where the denominator should be non-zero, meaning the phase between $\theta_i$ and $\theta_j$ can be any value except $\pi$. In other words, core $i$ and $j$ should not be aligned in a straight line with the central one to determine the displacement direction. Once $\theta_D$

is determined, the displacement amplitude is obtained via substituting Equation (5.4) to Equation (5.1), which can be expressed as

$$\delta = \frac{L^3}{3(1-p_e)\cdot\frac{\lambda_i}{\Delta\lambda}\cdot d\sin(\theta_D+\theta_i)(x-L)}. \tag{5.6}$$

Consequently, by measuring the Bragg wavelength shifts in different cores, $\theta_D$ and $\delta$ can be reconstructed from a random position, meaning that the proposed sensor has the capability of determining the direction and amplitude of the displacement simultaneously in the two-dimensional plane.

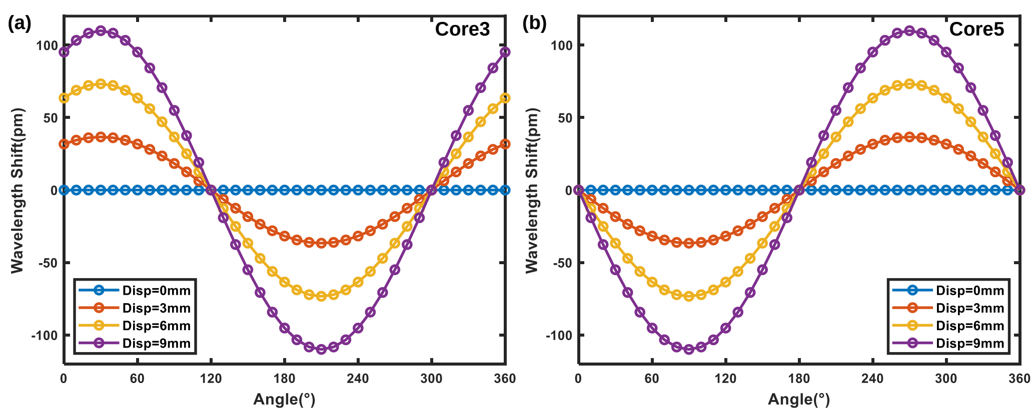


Figure 5.2. Simulation results of wavelength shift versus displacement direction varying from 0 to 360° in steps of 10° for (a) core 3 and (b) core 5, with displacement amplitude fixed at 0, 3, 6, and 9 mm.

In order to evaluate the performance before the experimental demonstration, the proposed sensor was firstly investigated theoretically. The free fiber length $L$ was set to be 111 mm, with the displacement direction changing from 0 to 360°. In the proposed sensor structure illustrated in Figure 5.1(b), the displacement distance determines the shifted angle $\omega$ of the sensing fiber at the fixed point, which was limited to less than 5° to keep a linear response between the displacement and the Bragg wavelength shift. The responses for Bragg wavelength shift in core 3 and core 5 with displacement direction varying from 0 to 360° in steps of 10° are represented in Figure 5.2, when displacement is fixed at 0, 3, 6, and 9 mm, respectively. It is obvious that there is a sinusoidal response for wavelength shift under different directions, and the shift amplitude increases when the applied displacement amplitude is larger. The initial phases of the sinusoidal curves in Figure 5.2 are related to the angular position of the specific core, i.e. $\pi/3$ for core 3, and $\pi$ for core 5. When comparing the phases of the curves in Figure 5.2(a) and Figure 5.2(b), there is an obvious $2\pi/3$ shift, corresponding to the angular difference between these two cores. Besides, the relationship between Bragg wavelength shift and the applied displacement of core 3 is indicated in Figure 5.3, with the displacement amplitude changing from 0 to 9 mm in steps of 1 mm, and the displacement direction varying from 0 to 330° in steps of 30°. It is worth mentioning that the slopes of the curves in Figure 5.3 represent the sensitivities of sensor at each displacement direction, which is also dependent on the fiber length. In order to quantify the dependency, the sensitivity-length response under a specific displacement direction, such as 90° is described in Figure 5.4. It indicates that a higher sensitivity can be achieved when shorten the free fiber length. In addition, it is pointed out that the location of FBG on the sensing fiber has an impact on the sensitivity of the sensor, due to the non-uniform displacement-induced bending radius along the fiber length. As a result, different strains are generated at distinct positions of the sensing fiber. Here, we define the fixed point with a position of 0. The inset in Figure 5.4 illustrates the displacement sensitivity for various FBG positions along the free fiber with a total length of 111 mm. The results denote that the FBG inscribed at the fixed point experiences the maximum strain during the displacement measurement.

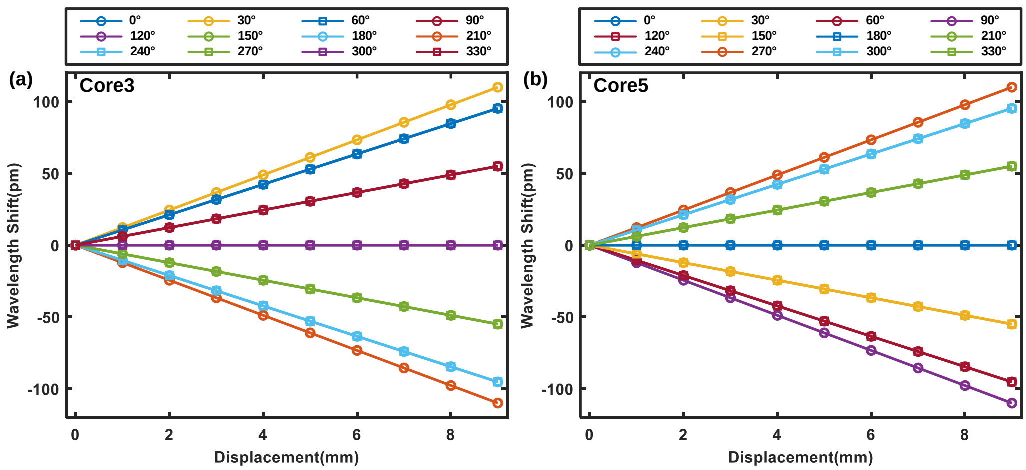


Figure 5.3. Simulation results of wavelength shift versus displacement amplitude changing from 0 to 9 mm in steps of 1 mm for (a) core 3 and (b) core 5, with displacement direction varying from 0 to 330° in steps of 30°.

The simulation result gives a guidance on the adjustment of parameters for the sensor development, including the choice of the fiber length, detectable distance for the displacement and the FBG position, in order to be applied in the real application. Evidently, there is a trade-off between the detectable range and the sensor sensitivity, which can be optimized during the application.

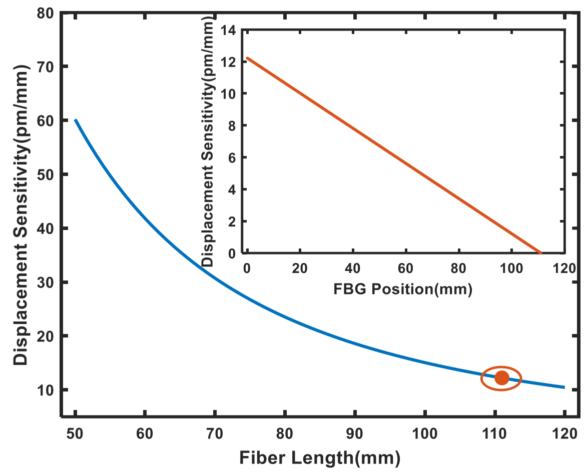


Figure 5.4. Simulation results of displacement sensitivity as a function of different free fiber length. Inset shows the displacement sensitivity response with respect to the position of FBG along the fiber length.

## 5.4 Two-Dimensional Displacement Sensor under Random Forest

### 5.4.1 Principle of Random Forest Regression

Random forest is an effective tool in prediction, which is a combination of tree predictors for classification and regression. As defined in [141], the random forest is a classifier consisting a aggregation of tree-shaped classifiers $\{h(x,\Theta_k), k=1,2,...\}$, where $\{\Theta_k\}$ are independent random vectors and each tree votes for the most popular label at input $x$. Random forest regression is an ensemble machine learning algorithm [141], where tree predictor $h(x,\Theta)$ takes on numerical values instead of class labels. It uses a large set of regression trees as base learners to constitute a forest for data training and predication [142].

Regression trees are run in parallel without interaction, where each of them grows on an individual bootstrap sample derived from the initial training data. Different from the node that uses the best splitting among all variables in standard trees, in random forest, each node is split based on the best from a randomly chosen subset of the predictors [143]. The best split at each node in a tree represents a binary test against the variable of the chosen predictor. The variables at each node are selected to minimize the residual sum of squares of both branches. The reason behind is its outperformance when compared to many other predictions and its robustness against overfitting and underfitting [141, 144].

To get an ensemble model with strong generalization, the regression tree in the model is set as uncorrelated as possible [141]. Random forest uses bagging [145], a parallel ensemble model to increase the diversity of trees. Bagging is the acronym of the "bootstrap aggregating". For example, in a learning set $\mathrm{T}$ that comprises data $\{(x_n, y_n), n=1,2,...,N\}$, the procedure that forming replicate data sets $\{\mathrm{T}_k\}$ which consisting of $N$ cases, drawn at random but with replacement from $\mathrm{T}$ is called bagging [145]. Each case in $\mathrm{T}$ may appear zero or multiple times in any particular $\mathrm{T}_k$, while about one-third of $\mathrm{T}$ are left in each set $\mathrm{T}_k$, what is called the out-of-bag (OOB) estimators. In random forest, there are two reasons to use bagging. One is the usage of bagging is able to enhance the accuracy when random features are utilized. The other is using OOB estimators to continuously estimate the error of the ensembled trees, as well as the strength of individual trees in the forest and correlation between trees [141]. In random forest regression, number of variables (*m*) used at each node for tree generation and the number of trees ($k$) are two user-defined parameters [141]. Usually, the results is insensitive to number of variables at each node, and therefore $k$ is the only user-defined parameter.

For an initial dataset with $N$ samples, a bootstrap sample is created by randomly selecting $N$ samples from the initial dataset with replacement (selected sample is returned to the initial dataset after one sampling, making it possible to be chosen during the next sampling). Prediction is constructed based on averaging the separate decisions from each tree in the forest. This characteristic makes random forest more robust when there is slight variation in input data, which enhances both the prediction accuracy and stability [145]. In random forest regression, the output values are numerical. Since the training set is independently selected from the random vector, the random forest predictor is obtained through average over $k$ of the trees $\left\{h\left(x,\Theta_k\right)\right\}$.

### 5.4.2 Random Forest-based Displacement Sensor

In this work, a Python-based random forest regression algorithm from the scikit-learn library was adopted for modelling. Since wavelength shifts of four of the seven cores were monitored during the measurement, a dataset constituting 8325 samples with four input variables was used. Two dependent variables, including the direction and amplitude of the displacement were correspondingly used as outputs. Flow chart of the random forest algorithm used for this sensor is illustrated in Figure

5.5, with a tree number *k* chosen as 100.

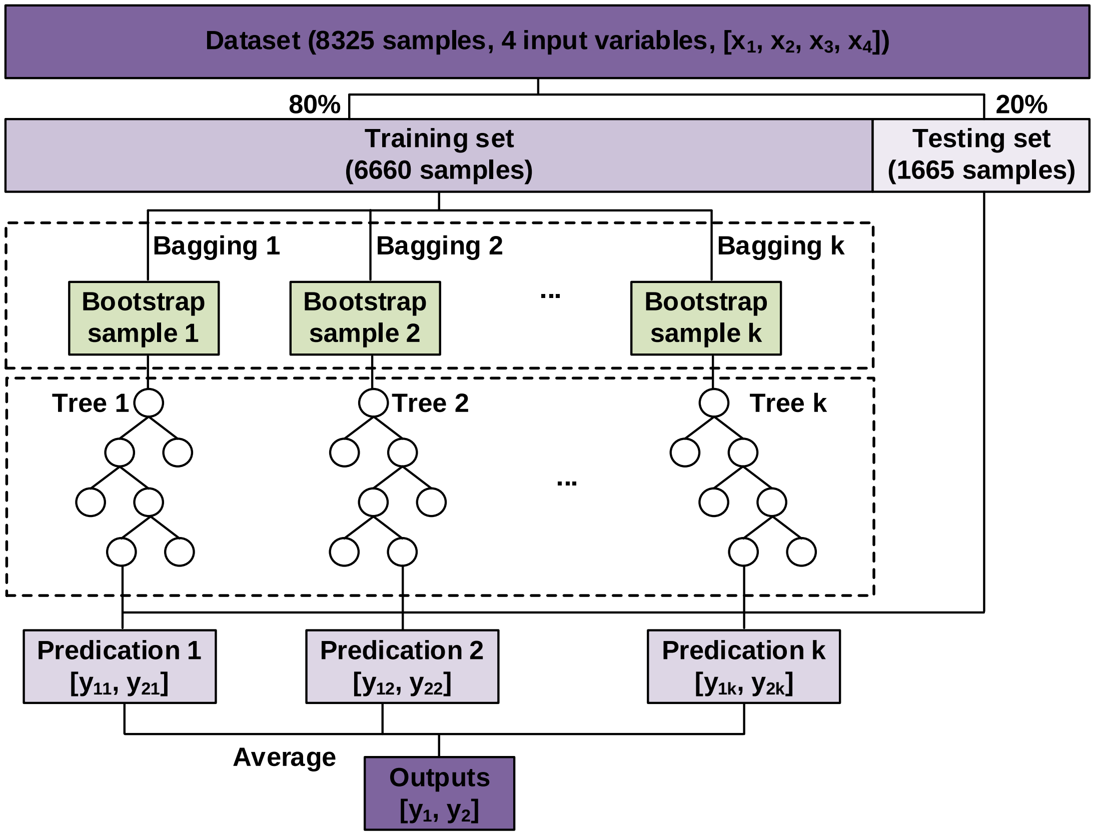


Figure 5.5. Flow chart of random forest algorithm in displacement sensor.

To ensure better fitting of the model, the input data was preprocessed. Ideally, the central core should always stay in the neutral plane during the measurement. However, there was an inevitable offset during the experiment. In addition, the central one was aimed for temperature compensation, representing the information it carried independent from the other three. As a result, we subtracted the response of the central core from the rest of the input variables, meaning the sensor is still temperature-insensitive based on the random forest reconstruction. After preprocessing dataset, 80% of the dataset was randomly divided for training, while the left 20% was for testing.

## 5.5 Experiment Setup of the Two-Dimensional Displacement Sensor

Schematic of the experimental setup is illustrated in Figure 5.6. The seven-core MCF inscribed with FBGs was mounted to a fiber rotator (Thorlabs, HFR007). Displacement was applied to the free end of the sensing fiber, and the other end was spliced to a 1-to-7 fan-out device. The MCF was clamped on the fiber rotator with the FBG-inscribed section free to bend. In order to interrogate the FBGs in different cores of the MCF, an interrogator (Micron Optics, sm130) with 1 pm resolution was connected to the SMFs of the fan-out device, such as core 1, 3, 5, and 7. Only the FBGs in four cores were measured, which was limited by our interrogator having four channels. Length of the free fiber was kept as 111 mm, with a displacement amplitude range of 0 to 45 mm, and the fiber rotator was used to change the direction within 360°. During the measurement, the displacement amplitude was varied by 1 mm and the direction was changed with a step of 10°.

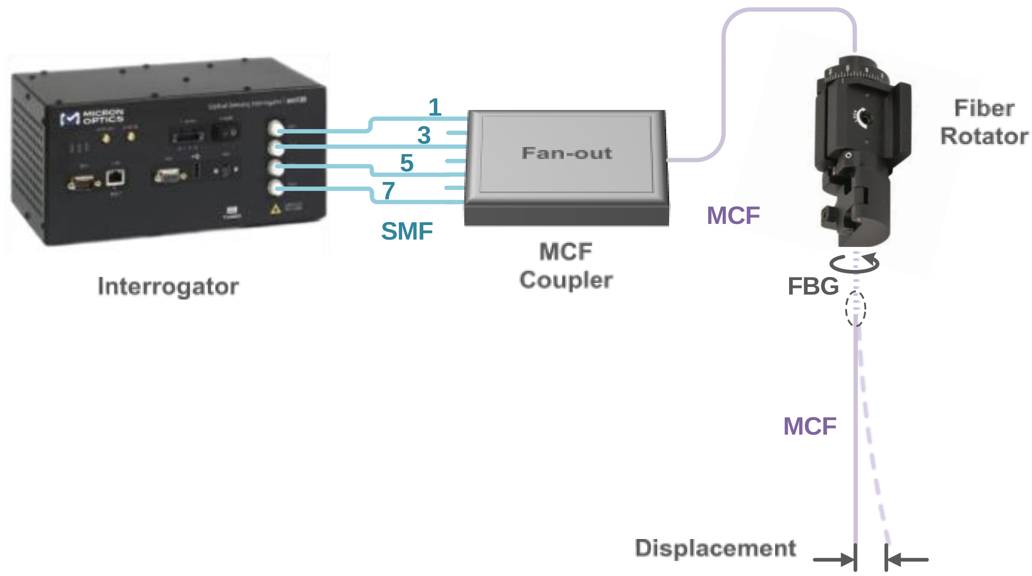


Figure 5.6. Schematic experimental setup for the two-dimensional vector displacement sensor.

During the experiment, FBG responses in core 1, 3, 5, and 7 were recorded, including a central core and three outer cores which were arranged in a regular triangle shape. The measured responses of the Bragg wavelength shift in core 3 and core 5 were recorded in Figure 5.7(a) and Figure 5.7(b), representing the experimental results in terms of displacement direction and amplitude, respectively. Moreover, Figure 5.8(a)-(c) give the Bragg wavelength shift as a function of applied displacement amplitude for three outer cores under different directions in the linear range (1 to 9 mm in steps of 1 mm), with the dots in different shapes representing the experimental data, and the lines indicating the fitting curves (an average fitting $R^2$ of 0.9995). The full range of the displacement amplitude was from 0 to 45 mm during the measurement, and the relationship became nonlinear with increasing amplitude. Therefore, the wavelength response of core 3 in the full range (1 to 45 mm in steps of

2 mm) is shown in Figure 5.8(d) for demonstration, where dots represent the experimental results and lines are connecting curves. The theoretical model is not applicable for large displacements because the response becomes nonlinear.

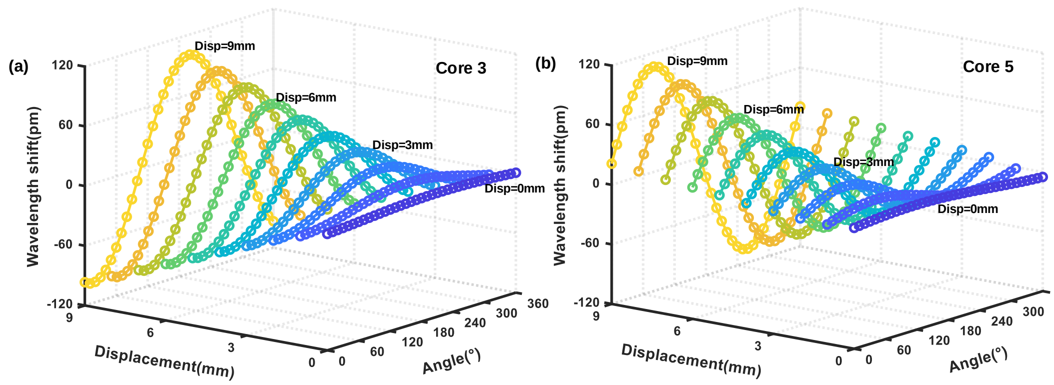


Figure 5.7. Experimental results of wavelength shift versus displacement direction in the two-dimensional range in (a) core 3 and (b) core 5 with displacement amplitude changing from 0 to 9 mm in steps of 1 mm.

In addition, the displacement sensitivities were recorded based on the slopes of the fitting lines in Figure 5.8(a)-(c), which were displayed in a polar coordinate as shown in Figure 5.9. An ‘8’-shaped sensitivity response was observed, indicating a strong direction dependence. For a specific core, such as core 3, the sensitivities are divided into the positive and negative parts, corresponding to the situation of stretching and compressing the FBGs during the measurement, respectively. The positive range for core 3 is recorded as 110°-200°-290°, while it is 290°-20°-110° for the negative sensitivity. Moreover, there is a 120° phase shift among the sensitivity response for individual cores, which is the same with their angular position difference as shown in Figure 5.1(a). The maximum positive sensitivities are obtained as 11.47, 12.31, and 11.73 pm/mm for core 3, 5, and 7 individually, corresponding to the displacement directions of 200°, 80°, 320°. There is a slight variation among the obtained sensitivity values, which is caused by the difference in the inscribed sensor depth during the fabrication process [63].

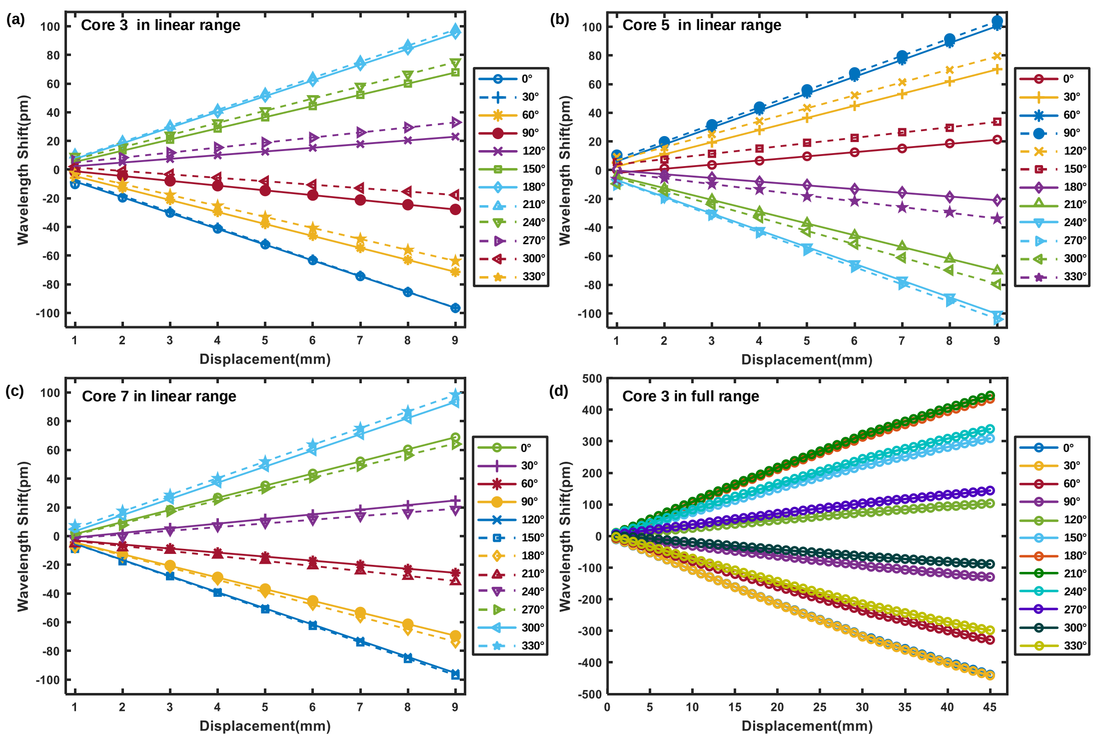


Figure 5.8. Experimental results of wavelength shift versus displacement amplitude in linear range of (a) core 3, (b) core 5, (c) core 7, and wavelength response of (d) core 3 in full range. The displacement direction varies from 0 to 330° in steps of 30°, with the dots indicating the experimental results while the lines in (a)-(c) representing the fitting ones, and (d) representing the connecting curves.

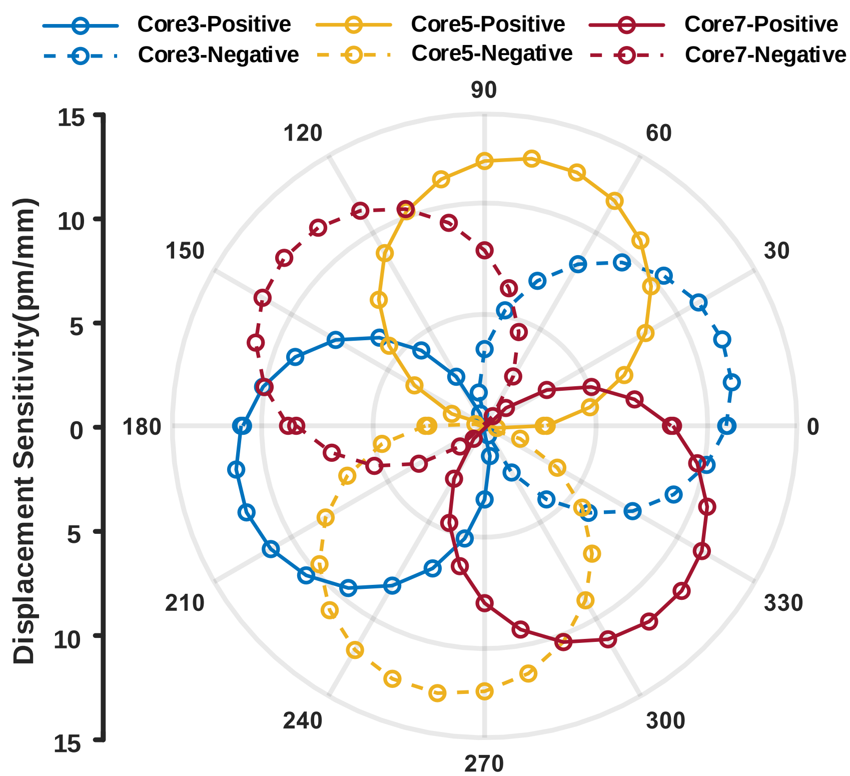


Figure 5.9. Experimental results of sensitivity-direction response in core 3, 5 and 7, with displacement direction changing from 0 to 360° in steps of 10°.

## 5.6 Displacement Reconstruction

### 5.6.1 Theoretical Model

Equation (5.5) indicates that the displacement direction can be retrieved through monitoring the Bragg wavelength shifts in two of the outer cores, which are not aligned in a straight line with the central core, while the direction is independent on the displacement amplitude. In addition, due to the hexagonal structure of the arrangement for the seven-core MCF, there is one fiber core which locates at the central of the cladding, which can be utilized for the compensation of fiber mechanical offset and temperature change, as it is located in the neutral axis and thus is not affected by the fiber bending. Therefore, a combination of three cores is enough to reconstruct the displacement information based on the theoretical model. Here, two of the four outer cores are chosen, such as core 3 and core 5 (combination 1), core 3 and core 7 (combination 2), or core 5 and core 7 (combination 3), to retrieve the displacement direction, with the absolute error plotted in Figure 5.10, which is defined as the absolute difference between the set direction and the measured one. Mean absolute errors (MAEs), defined as

$$MAE = \frac{1}{N}\sum_{i=1}^{N}\left(\left|y_i - \hat{y}_i\right|\right), \tag{5.7}$$

of different combinations for direction are 3.23°, 3.52° and 2.43°, respectively, where $y_i$ and $\hat{y}_i$ are the true and prediction value. Also, the root mean squared errors (RMSEs) are calculated, which is defined as

$$RMSE = \sqrt{MSE} = \sqrt{\frac{1}{N}\sum_{i=1}^{N}\left(y_i - \hat{y}_i\right)^2}. \tag{5.8}$$

The RMSEs under each combination are 10.3°, 9.95°, and 9.3°. Based on Figure 5.10, there are three characteristics of the direction error. First is the direction error found to be direction sensitive. A regular sinusoidal shape is observed in error maps, which is related to the sensitivity dependency of displacement direction, meaning there is a relatively smaller error under the direction with high sensitivity. Secondly, the error gets smaller when the displacement gets larger, which may be caused by the little variation under small displacement. Finally, there is a 120° phase shift between different combinations, which is matched with the sensitivity curve properly.

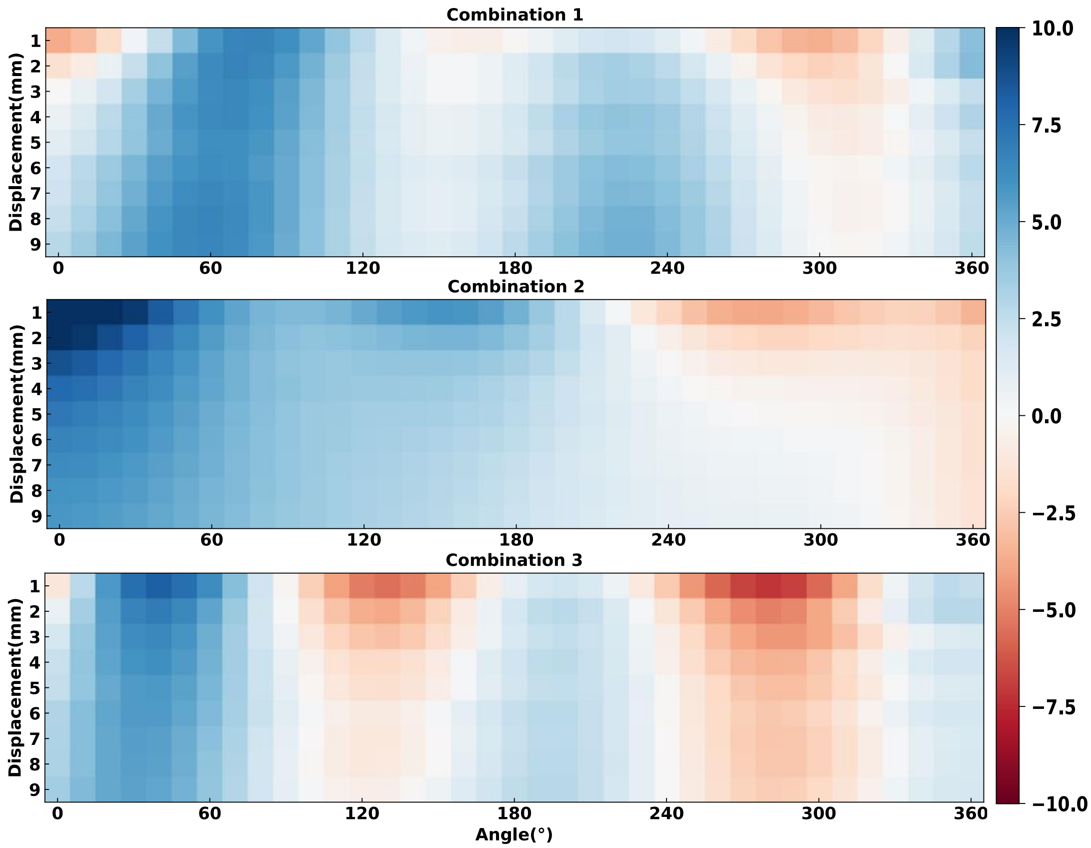


Figure 5.10. Absolute errors of displacement direction based on different combinations of the outer cores using theoretical model, with the direction and displacement ranges of 0-360° and 1-9 mm, respectively.

After the determination of the displacement direction, the amplitude can be calculated with the help of Equation (5.6). The displacement amplitude is obtained based on the combination of the reconstructed displacement direction and the angular position of one of the cores used in the direction calculation process. Hence, there are in total six combinations for the amplitude reconstruction. In addition, we only consider the linear range for reconstruction using the theoretical model. The displacement amplitude is set to change from 0 to 9 mm. Different from the direction, the amplitude is highly dependent on the value of the measured direction, meaning the errors introduced from the direction would have a negative impact on the reconstruction of the amplitude owing to the propagation of error. Figure 5.11 summarizes the displacement amplitude error based on different combinations, with each combination for direction calculation having two branches (a and b). MAEs are 12.67, 14.63, 9.7, 9.92, 11.58, and 8.29 mm for combination 1(a) to 3(b), while RMSEs are 29.3, 40.7, 18.74, 21.54, 24.45 and 16.12 mm, respectively. It is clear that the errors are too large for meaningful retrieval. However, there is still a sinusoidal trend in the amplitude error map, where a small error happens under a high direction sensitivity with an interval of 180°, which is similar to the performance of the direction.

The poor performance of the amplitude retrieval based on the theoretical model could be caused by several factors, including the unprecise model, system error and the errors carried from the direction. In addition, the limited range is another disadvantage for the application of the displacement sensor. Overall, the retrieval performance based on the theoretical model greatly depends on the quality of the theoretical model, while little variation may cause large errors during the retrieval process.

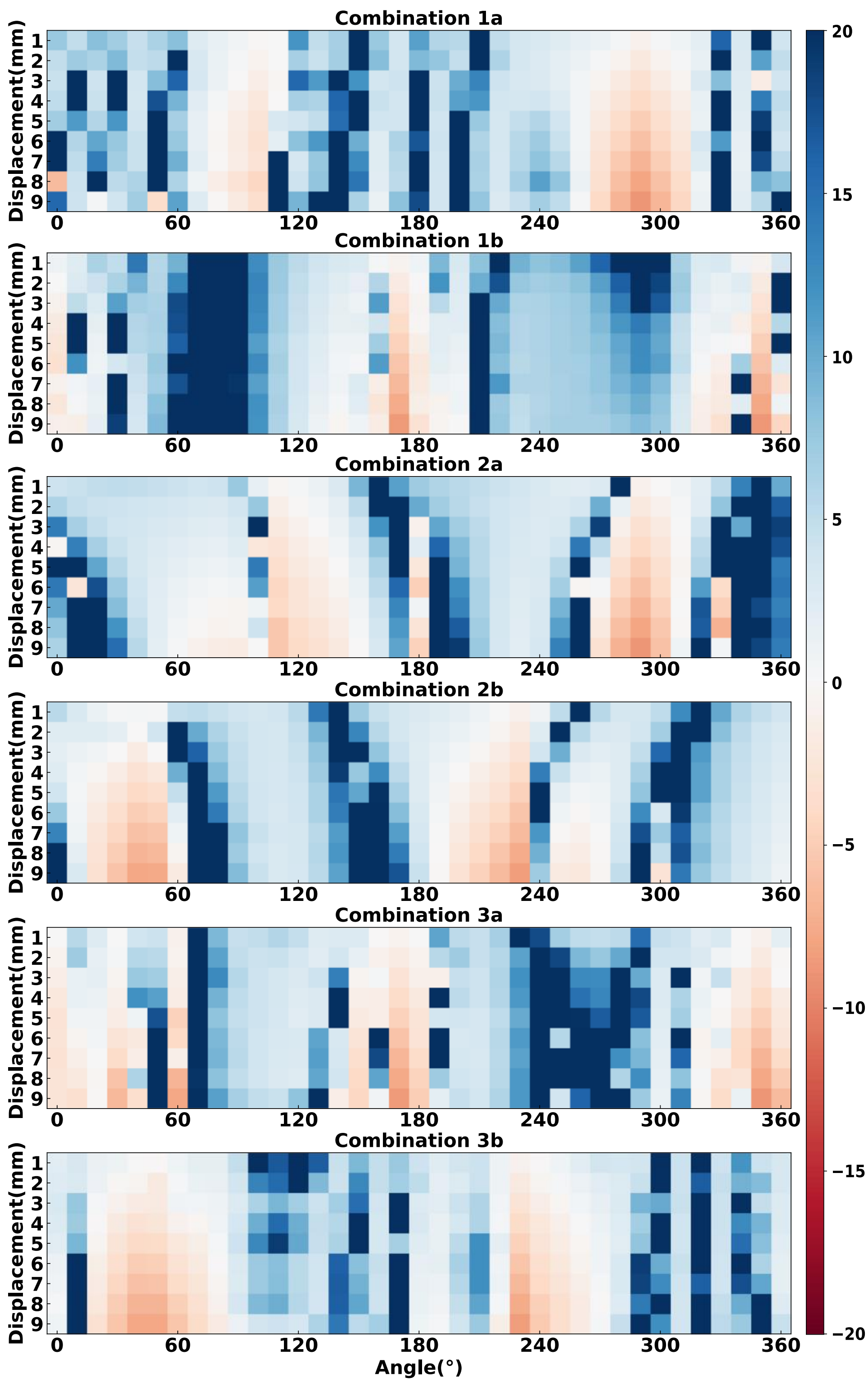


Figure 5.11. Absolute errors of displacement amplitude based on different combinations of the outer cores using theoretical model, with the direction and displacement ranges of 0-360° and 1-9 mm, respectively.

### 5.6.2 Random Forest Model

To assess the effectiveness of random forest regression, coefficient of determination (score) $R^2$ is used to evaluate the performance, which is defined as

$$R^2 = 1 - \frac{\sum (y_i - \hat{y}_i)^2}{\sum (y_i - \bar{y}_i)^2}, \tag{5.9}$$

where $y_i$ and $\hat{y}_i$ are the true and prediction value, and $\bar{y}_i$ indicates the mean of label. The best is 1.0, and we get a score of 0.997, reflecting the good accuracy obtained with random forest algorithm.

Similar to the evaluation of the theoretical model, the retrieval performance is also investigated for random forest, and the absolute error maps of the two parameters are shown in Figure 5.12. Since the algorithm concerns only about the training data, the linearity is no longer a restriction during the retrieval process. The calculation range for amplitude is extended to 0-45 mm, while the direction range remains unchanged. MAEs of direction and amplitude are 1.22° and 0.14 mm, respectively.

On the one hand, for the direction reconstruction, it is evident that the absolute error is smaller when increasing the displacement amplitude, which is similar to the performance of theoretical model. However, there remains no longer characteristic of direction sensitivity. With the increase of the amplitude, the direction retrieval becomes stable at most time, however it becomes failure at very few points, which can be solved through enlarging size of the database. When comparing with the results obtained from theoretical model, the overall performance for the direction is enhanced by 60% with the random forest algorithm. On the other hand, there is a great enhancement in the retrieval of displacement amplitude, including the enlarged measurement range and decreased error. Since random forest predicts the amplitude based on averaging the predictions of trees, which is not a linear process compared to the theoretical model, where the linearity restriction disappears. As a result, the measurement range is enlarged by 5 times, which can be further enhanced through adjusting length of the fiber. In addition, the measurement error is reduced by 98% when comparing with the results from theoretical model, representing a perfect performance for the amplitude retrieval.

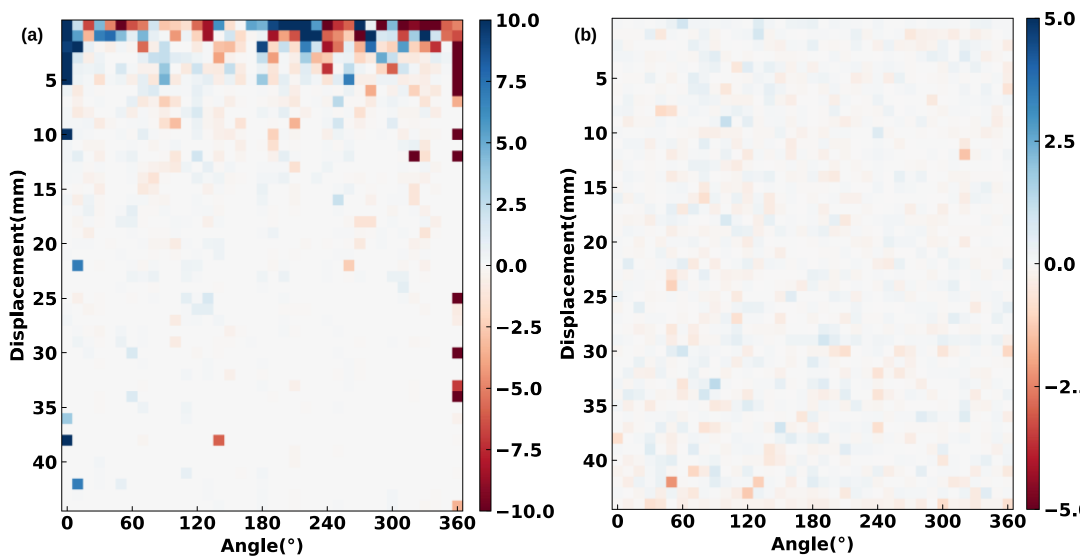


Figure 5.12. Absolute errors of displacement (a) direction and (b) amplitude using random forest, with the direction and displacement ranges of 0-360° and 1-45 mm, respectively.

It is possible that a model obtains a high score based on the existing labels, but fail on prediction when meeting unseen data, which is kind of overfitting. Therefore, a cross-validation is adopted to avoid it, called a *n*-fold cross-validation, where the training set is divided to $n$ smaller sets. The model is trained based on the left ($n$-1) of folds, while the result is validated on the remaining part of the data. In this work, a 5-fold cross-validation is adopted, with the description shown in Figure 5.13.

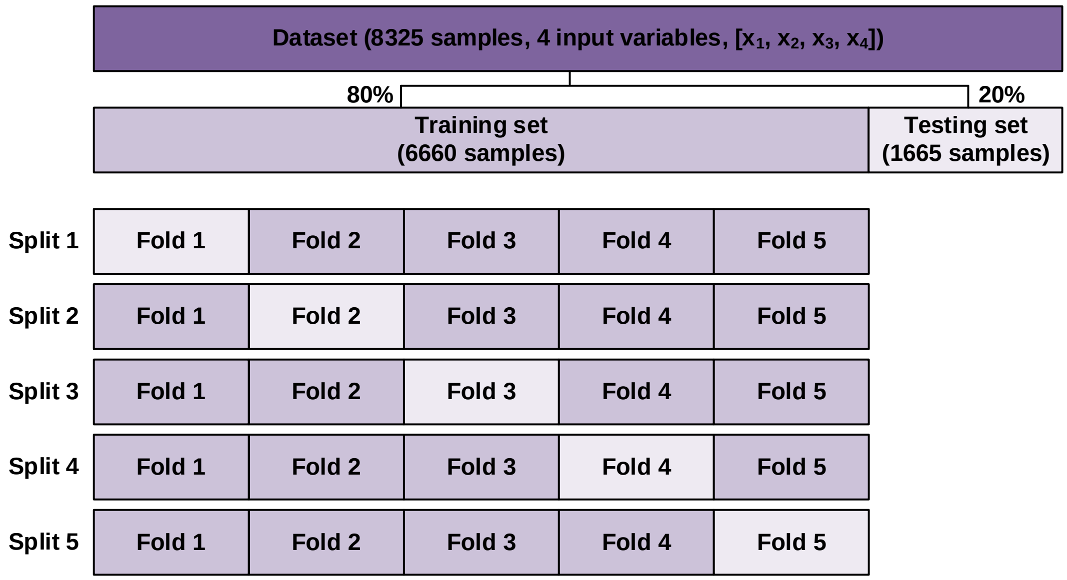


Figure 5.13. Procedure of 5-fold cross-validation.

Table 5.1 collects the results of 5-fold cross-validation, including the score, MAEs of direction and amplitude, as well as RMSEs of the model.

Table 5.1. Results of 5-fold cross-validation

| | **Score** | **Direction** | | **Amplitude** | |
|---|---|---|---|---|---|
| | | MAEs | RMSEs | MAEs | RMSEs |
| **Split 1** | 0.996 | 1.29° | 7.49° | 0.22 mm | 0.58 mm |
| **Split 2** | 0.996 | 1.39° | 8.25° | 0.2 mm | 0.34 mm |
| **Split 3** | 0.992 | 1.64° | 13.36° | 0.19 mm | 0.37 mm |
| **Split 4** | 0.998 | 1.27° | 7° | 0.19 mm | 0.33 mm |
| **Split 5** | 0.993 | 1.69° | 12.63° | 0.21 mm | 0.42 mm |

Furthermore, Table 5.2 summaries the comparison results of the reconstructed displacement information under two models, including the measurement range, and MAEs of displacement direction and amplitude.

Table 5.2. Comparison between reconstructed results using two models

| | Theoretical model | | Random Forest model |
|---|---|---|---|
| **Range** | 0-9 mm | | 0-45 mm |
| **MAEs of direction** | Combination 1 | 3.23° | 1.22° |
| | Combination 2 | 3.52° | |
| | Combination 3 | 2.43° | |
| | Average | 3.06° | |
| **MAEs of amplitude** | Combination 1a | 12.67 mm | 0.14 mm |
| | Combination 1b | 14.63 mm | |
| | Combination 2a | 9.7 mm | |
| | Combination 2b | 9.92 mm | |
| | Combination 3a | 11.58 mm | |
| | Combination 3b | 8.29 mm | |
| | Average | 11.13 mm | |

## 5.7 Summary

In this chapter, the design of an FBG-based MCF two-dimensional displacement measurement is discussed, where the sensing performance is investigated under both theoretical model and machine learning model. Development of the two-dimensional fiber-optic displacement sensor is overviewed, indicating a limited measurement range and an absence characteristic of obtaining actual displacement information. The proposed sensor is capable of getting the direction and amplitude of the displacement in a two-dimensional range, with its performance assisted by the random forest, one of the most popular machine learning algorithms. Theoretical model of the displacement sensor is investigated, with an optimized sensing parameter based on the simulation results. Attention is put to highlight the characteristics of random forest, as well as the model used to develop the displacement sensor. Displacement measurements are conducted, followed by the reconstruction performance under both theoretical and random forest models. Results indicate that a much better performance is provided by random forest model, with an enhanced measurement range (from 0 to 45 mm) and a reduced measurement error. MAEs of direction and amplitude reconstruction are decreased by 60% and 98%, separately by using the random forest model. The application of random forest in the FBG-based two-dimensional displacement sensor enhanced the performance in both accuracy and measurement range. It also showed the potential for the machine learning methods to be applied in point-based optical sensing areas, especially for multi-parameter sensing.

# Chapter 6 Conclusion and Future Work

## 6.1 Conclusion

The contribution of this thesis is concentrated on the fabrication of the multi-core fiber (MCF)-based fiber Bragg gratings (FBGs), and the application of them for measurements of acceleration, inclination and displacement. Theoretical models are investigated to reconstruct the actual information, while machine learning algorithms are also introduced to improve the sensing performance.

Several lasers, including two excimer lasers (193 and 248 nm) and one solid-state laser (213 nm) were utilized to inscribe FBGs in MCFs. Factors that compromise the uniformity of these FBGs in MCFs were investigated. Theoretical models of using MCF-based FBGs or FBG arrays for two or three-dimensional sensing were proposed.

An orientation-sensitive two-dimensional vibration sensor was proposed, based on FBGs inscribed in a silica seven-core MCF, with temperature insensitivity. Vibration information, including vibration orientation, frequency as well as acceleration, were obtained simultaneously through monitoring of the wavelength shifts of three of the seven cores, including the central core and two outer cores which were not aligned in a straight line. Performance of the proposed vibration sensor in terms of free-fiber length, frequency, acceleration and vibration orientation were experimentally investigated. A sensitivity which is strongly dependent on the orientation was achieved, with a best orientation accuracy of 0.127° over a range of 0-180°. In order to verify the stability of the performance, different sets of chosen outer cores were utilized to achieve the orientation retrieval. Moreover, the resonance frequency and the sensitivity can be optimized through adjusting the length and weight of the free fiber. The ease of fabrication as well as the versatility of the proposed sensor makes it potentially useful in dynamic monitoring for industrial applications.

An all-fiber two-dimensional inclination sensor is also reported, with the capability of measuring the azimuthal angle and the inclination angle, simultaneously, through the usage of the FBG inscribed MCF. The sensor performance was theoretically optimized and experimentally investigated. Excellent agreement between simulated and experimental results was achieved. Through detection of the wavelength shifts of the FBGs inscribed in the central core and two outer cores of a silica seven-core MCF, a minimum error of 0.0056° for the azimuthal angle, and 0.025° for the inclination angle, were obtained. The detection range of the former ranges from 0 to 360°, while the latter ranges from 0 to 90°. Meanwhile, the FBG in the central core can be used for temperature-compensation since it remains in the neutral plane of the fiber under bending conditions. The proposed fiber sensor is easy to fabricate and robust, increasing its potential in practical applications.

In addition, a two-dimensional vector displacement sensor is described based on a similar structure, with the capability of obtaining the displacement direction and amplitude, simultaneously. The reconstruction performance was investigated under both a theoretical model and a random forest algorithm. The displacement direction ranges from 0 to 360°, while the measurable amplitude range relates to the choice of the reconstruction method. For the performance based on theoretical model, the displacement amplitude range was dependent on the length of the fiber. It was performed under a linear range (from 0 to 9 mm). Meanwhile, the measurement error was greatly compromised by the model quality and the system's error. However, the random forest model outperforms the theoretical model with an enhanced measurement range (from 0 to 45 mm) and a reduced measurement error for displacement. Mean absolute errors (MAEs) of direction and amplitude reconstruction decreased by 60% and 98%, separately by using the random forest model. The application of random forest in the FBG-based two-dimensional displacement sensor enhances the performance in both the accuracy and range. It also shows the potential for the machine learning methods to be applied in point-based optical sensing areas, especially for multi-parameter sensing.

## 6.2 Future Work

As well as the interest of inscribing FBGs in MCF, there are other kinds of gratings, such as phase-shifted fiber Bragg grating (PSFBG), tilted fiber Bragg grating (TFBG), chirped fiber Bragg grating (CFBG) and long-period grating (LPG) that can be inscribed. For example, the PSFBG has a narrower linewidth compared with the uniform FBG, suitable for the application where a higher sensitivity is need. Apart from these different types of gratings, lasers such as the femtosecond laser is also a promising candidate for the MCF-based grating inscription. Since the femtosecond laser can be focused on individual cores of the MCF, it is possible to fabricate different grating structures on them.

In regards of sensing applications, two-dimensional vector sensing parameters, including twist and force are able to be detected with the use of these FBG inscribed MCFs, while three-dimensional shape sensing can be considered as another popular research area for these MCFs. Also, design and fabrication of different kinds of MCFs, such as air-hole-assisted MCFs and polymer-based MCFs are of great value, which can be applied for multi-dimensional sensing in various disciplines.

In the characterization of the grating inscription, manufacturing of the MCF coupler which provides the possibility to monitor individual cores in the MCF is of tremendous importance. Development of these MCF couplers with high efficiency can bring huge convenience for the application of MCFs in multi-dimensional sensing.

Machine learning algorithms can be further extended to be applied in multi-dimensional sensing area. Utilization and optimization of machine learning algorithms in point-based optical sensing is yet to be fully investigated, where the algorithms have superiority over traditional methods, especially when the accuracy of theoretical models are low.

# Reference


[1] Q. Rong, and X. Qiao, "FBG for oil and gas exploration," Journal of Lightwave Technology **37**, 2502-2515 (2018).

[2] Y. Weng, X. Qiao, T. Guo, M. Hu, Z. Feng, R. Wang, and J. Zhang, "A robust and compact fiber Bragg grating vibration sensor for seismic measurement," IEEE Sensors Journal **12**, 800-804 (2011).

[3] P. F. Yuan, H. Meng, L. Yu, and L. Zhang, "Robotic multi-dimensional printing based on structural performance," in *Robotic fabrication in architecture, art and design 2016*(Springer, 2016), pp. 92-105.

[4] S. G. Khan, G. Herrmann, T. Pipe, and C. Melhuish, "Adaptive multi-dimensional compliance control of a humanoid robotic arm with anti-windup compensation," in *2010 IEEE/RSJ International Conference on Intelligent Robots and Systems*(IEEE2010), pp. 2218-2223.

[5] G. Wild, and S. Hinckley, "Acousto-ultrasonic optical fiber sensors: Overview and state-of-the-art," IEEE Sensors Journal **8**, 1184-1193 (2008).

[6] M. A. Riza, Y. I. Go, S. W. Harun, and R. R. Maier, "FBG sensors for environmental and biochemical applications—A review," IEEE Sensors Journal **20**, 7614-7627 (2020).

[7] B. Lee, "Review of the present status of optical fiber sensors," Optical Fiber Technology **9**, 57-79 (2003).

[8] K. O. Hill, Y. Fujii, D. C. Johnson, and B. S. Kawasaki, "Photosensitivity in optical fiber waveguides: Application to reflection filter fabrication," Applied Physics Letters **32**, 647-649 (1978).

[9] Z. Yong, C. Zhan, J. Lee, S. Yin, and P. Ruffin, "Multiple parameter vector bending and high-temperature sensors based on asymmetric multimode fiber Bragg gratings inscribed by an infrared femtosecond laser," Optics Letters **31**,

1794-1796 (2006).

[10] W. Lin, Y. Miao, H. Zhang, B. Liu, Y. Liu, B. Song, and J. Wu, "Two-dimensional magnetic field vector sensor based on tilted fiber Bragg grating and magnetic fluid," Journal of Lightwave Technology **31**, 2599-2605 (2013).

[11] T. Guo, L. Shang, F. Liu, C. Wu, B.-O. Guan, H.-Y. Tam, and J. Albert, "Polarization-maintaining fiber-optic-grating vector vibroscope," Optics Letters **38**, 531-533 (2013).

[12] B. H. Lee, Y. H. Kim, K. S. Park, J. B. Eom, M. J. Kim, B. S. Rho, and H. Y. Choi, "Interferometric fiber optic sensors," Sensors **12**, 2467-2486 (2012).

[13] S. Zhang, W. Zhang, S. Gao, P. Geng, and X. Xue, "Fiber-optic bending vector sensor based on Mach-Zehnder interferometer exploiting lateral-offset and up-taper," Optics Letters **37**, 4480-4482 (2012).

[14] J. Villatoro, V. P. Minkovich, and J. Zubia, "Photonic crystal fiber interferometric vector bending sensor," Optics Letters **40**, 3113-3116 (2015).

[15] H. Gong, D. Wang, M. Xiong, C.-L. Zhao, and K. Ni, "Optical fiber hollow ellipsoid for directional bend sensing with a large bending range," Optical Materials Express **7**, 1767-1776 (2017).

[16] P. Chen, X. Shu, and K. Sugden, "Compact assembly-free vector bend sensor based on all-in-fiber-core Mach-Zehnder interferometer," Optics Letters **43**, 531-534 (2018).

[17] Y. Li, S. Pu, Y. Zhao, R. Zhang, Z. Jia, J. Yao, Z. Hao, Z. Han, D. Li, and X. Li, "All-fiber-optic vector magnetic field sensor based on side-polished fiber and magnetic fluid," Optics Express **27**, 35182-35188 (2019).

[18] G. Liu, Q. Sheng, W. Hou, and M. Han, "Optical fiber vector flow sensor based on a silicon Fabry-Perot interferometer array," Optics Letters **41**, 4629-4632 (2016).

[19] E. Udd, W. Schulz, J. Seim, E. Haugse, A. Trego, P. Johnson, T. Bennett, D. Nelson, and A. Makino, "Multidimensional strain field measurements using fiber optic grating sensors," in *SPIE's 7th Annual International Symposium on Smart Structures and Materials*(SPIE2000).

[20] D. Zhao, X. Chen, K. Zhou, L. Zhang, I. Bennion, W. N. MacPherson, J. S. Barton, and J. D. Jones, "Bend sensors with direction recognition based on long-period gratings written in D-shaped fiber," Applied Optics **43**, 5425-5428 (2004).

[21] X. Chen, C. Zhang, D. J. Webb, R. Suo, G. Peng, and K. Kalli, "Optical bend sensor for vector curvature measurement based on Bragg grating in eccentric core polymer optical fibre," in *20th International Conference on Optical Fibre Sensors*(International Society for Optics and Photonics2009), p. 750327.

[22] W. Bao, Q. Rong, F. Chen, and X. Qiao, "All-fiber 3D vector displacement (bending) sensor based on an eccentric FBG," Optics Express **26**, 8619-8627 (2018).

[23] T. Guo, L. Shang, Y. Ran, B.-O. Guan, and J. Albert, "Fiber-optic vector vibroscope," Optics Letters **37**, 2703-2705 (2012).

[24] 24. Y.-P. Li, W.-G. Zhang, S. Wang, L. Chen, Y.-X. Zhang, B. Wang, T.-Y. Yan, X.-Y. Li, and W. Hu, "Bending vector sensor based on a pair of opposite tilted long-period fiber gratings," IEEE Photonics Technology Letters **29**, 224-227 (2016).

[25] Q. Zhou, W. Zhang, L. Chen, Z. Bai, L. Zhang, L. Wang, B. Wang, and T. Yan, "Bending vector sensor based on a sector-shaped long-period grating," IEEE Photonics Technology Letters **27**, 713-716 (2015).

[26] Y.-P. Wang, and Y.-J. Rao, "A novel long period fiber grating sensor measuring curvature and determining bend-direction simultaneously," IEEE Sensors Journal **5**, 839-843 (2005).

[27] D. Feng, W. Zhou, X. Qiao, and J. Albert, "Compact optical fiber 3D shape sensor based on a pair of orthogonal tilted fiber Bragg gratings," Scientific Reports **5**, 1-7 (2015).

[28] D. Feng, X. Qiao, and J. Albert, "Off-axis ultraviolet-written fiber Bragg gratings for directional bending measurements," Optics Letters **41**, 1201-1204 (2016).

[29] D. J. Richardson, J. M. Fini, and L. E. Nelson, "Space-division multiplexing in optical fibres," Nature Photonics **7**, 354-362 (2013).

[30] P. J. Winzer, D. T. Neilson, and A. R. Chraplyvy, "Fiber-optic transmission and networking: the previous 20 and the next 20 years [Invited]," Optics Express **26**, 24190 (2018).

[31] Y. Amma, Y. Sasaki, K. Takenaga, S. Matsuo, J. Tu, K. Saitoh, M. Koshiba, T. Morioka, and Y. Miyamoto, "High-density multicore fiber with heterogeneous core arrangement," in *Optical Fiber Communications Conference and Exhibition (OFC)*(Optical Society of America, Los Angeles, CA, USA, 2015), p. Th4C.4.

[32] T. Hayashi, T. Nakanishi, K. Hirashima, O. Shimakawa, F. Sato, K. Koyama, A. Furuya, Y. Murakami, and T. Sasaki, "125-µm-Cladding eight-core multi-core fiber realizing ultra-high-density cable suitable for O-band short-reach optical interconnects," Journal of Lightwave Technology **34**, 85-92 (2016).

[33] K. Takenaga, Y. Sasaki, N. Guan, S. Matsuo, M. Kasahara, K. Saitoh, and M. Koshiba, "Large effective-area few-mode multicore fiber," IEEE Photonics Technology Letters **24**, 1941-1944 (2012).

[34] K. Shibahara, D. Lee, T. Kobayashi, T. Mizuno, H. Takara, A. Sano, H. Kawakami, Y. Miyamoto, H. Ono, M. Oguma, Y. Abe, T. Matsui, R. Fukumoto, Y. Amma, T. Hosokawa, S. Matsuo, K. Saitoh, M. Yamada, and T. Morioka, "Dense SDM (12-core × 3-mode) transmission over 527 km with 33.2-ns

mode-dispersion employing low-complexity parallel MIMO frequency-domain equalization," Journal of Lightwave Technology **34**, 196-204 (2016).

[35] R. Ryf, R. J. Essiambre, S. Randel, A. H. Gnauck, P. J. Winzer, T. Hayashi, T. Taru, and T. Sasaki, "MIMO-based crosstalk suppression in spatially multiplexed 3×56-Gb/s PDM-QPSK signals for strongly coupled three-core fiber," IEEE Photonics Technology Letters **23**, 1469-1471 (2011).

[36] T. Mizuno, K. Shibahara, H. Ono, Y. Abe, Y. Miyamoto, F. Ye, T. Morioka, Y. Sasaki, Y. Amma, K. Takenaga, S. Matsuo, K. Aikawa, K. Saitoh, Y. Jung, D. J. Richardson, K. Pulverer, M. Bohn, and M. Yamada, "32-Core dense SDM unidirectional transmission of PDM-16QAM signals over 1600 km using crosstalk-managed single-mode heterogeneous multicore transmission line," in *Optical Fiber Communication Conference Postdeadline Papers*(Optical Society of America, Anaheim, California, 2016), p. Th5C.3.

[37] J. Sakaguchi, W. Klaus, J. M. D. Mendinueta, B. J. Puttnam, R. S. Luis, Y. Awaji, N. Wada, T. Hayashi, T. Nakanishi, T. Watanabe, Y. Kokubun, T. Takahata, and T. Kobayashi, "Realizing a 36-core, 3-mode fiber with 108 spatial channels," in *Optical Fiber Communications Conference and Exhibition (OFC)*(OSA, Los Angeles, CA, USA, 2015), p. Th5C.2.

[38] D. Soma, K. Igarashi, Y. Wakayama, K. Takeshima, Y. Kawaguchi, N. Yoshikane, T. Tsuritani, I. Morita, and M. Suzuki, "2.05 Peta-bit/s super-nyquist-WDM SDM transmission using 9.8-km 6-mode 19-core fiber in full C band," in *2015 European Conference on Optical Communication (ECOC)*(IEEE2015), pp. 1-3.

[39] L. Yuan, J. Yang, and Z. Liu, "A compact fiber-optic flow velocity sensor based on a twin-core fiber Michelson interferometer," IEEE Sensors Journal **8**, 1114-1117 (2008).

[40] F. Peng, J. Yang, X. Li, Y. Yuan, B. Wu, A. Zhou, and L. Yuan, "In-fiber

integrated accelerometer," Optics Letters **36**, 2056-2058 (2011).

[41] A. Zhou, Y. Zhang, G. Li, J. Yang, Y. Wang, F. Tian, and L. Yuan, "Optical refractometer based on an asymmetrical twin-core fiber Michelson interferometer," Optics Letters **36**, 3221-3223 (2011).

[42] R. Chu, C. Guan, Y. Bo, J. Liu, J. Shi, J. Yang, P. Ye, P. Li, J. Yang, and L. Yuan, "Graphene decorated twin-core fiber Michelson interferometer for all-optical phase shifter and switch," Optics Letters **45**, 177 (2020).

[43] F. Tan, S. Chen, W. Lyu, Z. Liu, C. Yu, C. Lu, and H.-Y. Tam, "Non-invasive human vital signs monitoring based on twin-core optical fiber sensors," Biomedical Optics Express **10**, 5940 (2019).

[44] A. V. Newkirk, J. E. Antonio-Lopez, A. Velazquez-Benitez, J. Albert, R. Amezcua-Correa, and A. Schulzgen, "Bending sensor combining multicore fiber with a mode-selective photonic lantern," Optics Letters **40**, 5188-5191 (2015).

[45] J. Villatoro, A. Van Newkirk, E. Antonio-Lopez, J. Zubia, A. Schülzgen, and R. Amezcua-Correa, "Ultrasensitive vector bending sensor based on multicore optical fiber," Optics Letters **41**, 832 (2016).

[46] C. Li, T. Ning, C. Zhang, J. Li, C. Zhang, X. Wen, H. Lin, and L. Pei, "All-fiber multipath Mach-Zehnder interferometer based on a four-core fiber for sensing applications," Sensors and Actuators A: Physical **248**, 148-154 (2016).

[47] C. Li, T. Ning, J. Li, C. Zhang, C. Zhang, H. Lin, and L. Pei, "Fiber-optic laser sensor based on all-fiber multipath Mach-Zehnder interferometer," IEEE Photonics Technology Letters **28**, 1908-1911 (2016).

[48] Z. Zhao, M. Tang, S. Fu, S. Liu, H. Wei, Y. Cheng, W. Tong, P. P. Shum, and D. Liu, "All-solid multi-core fiber-based multipath Mach-Zehnder interferometer for temperature sensing," Applied Physics B **112**, 491-497 (2013).

[49] L. Duan, P. Zhang, M. Tang, R. Wang, Z. Zhao, S. Fu, L. Gan, B. Zhu, W. Tong, D. Liu, and P. P. Shum, "Heterogeneous all-solid multicore fiber based multipath Michelson interferometer for high temperature sensing," Optics Express **24**, 20210 (2016).

[50] L. Gan, R. Wang, D. Liu, L. Duan, S. Liu, S. Fu, B. Li, Z. Feng, H. Wei, W. Tong, P. Shum, and M. Tang, "Spatial-division multiplexed Mach-Zehnder interferometers in heterogeneous multicore fiber for multiparameter measurement," IEEE Photonics Journal **8**, 1-8 (2016).

[51] R. M. Silva, M. S. Ferreira, J. Kobelke, K. Schuster, and O. Frazao, "Simultaneous measurement of curvature and strain using a suspended multicore fiber," Optics Letters **36**, 3939-3941 (2011).

[52] G. Salceda-Delgado, A. Van Newkirk, J. E. Antonio-Lopez, A. Martinez-Rios, A. Schülzgen, and R. Amezcua Correa, "Compact fiber-optic curvature sensor based on super-mode interference in a seven-core fiber," Optics Letters **40**, 1468 (2015).

[53] J. Villatoro, E. Antonio-Lopez, A. Schulzgen, and R. Amezcua-Correa, "Miniature multicore optical fiber vibration sensor," Optics Letters **42**, 2022-2025 (2017).

[54] H. Zhang, Z. Wu, P. P. Shum, X. Q. Dinh, C. W. Low, Z. Xu, R. Wang, X. Shao, S. Fu, W. Tong, and M. Tang, "Highly sensitive strain sensor based on helical structure combined with Mach-Zehnder interferometer in multicore fiber," Scientific Reports **7** (2017).

[55] F. Tan, Z. Liu, J. Tu, C. Yu, C. Lu, and H.-Y. Tam, "Torsion sensor based on inter-core mode coupling in seven-core fiber," Optics Express **26**, 19835 (2018).

[56] G. M. Flockhart, W. N. MacPherson, J. S. Barton, J. D. Jones, L. Zhang, and I. Bennion, "Two-axis bend measurement with Bragg gratings in multicore

optical fiber," Optics Letters **28**, 387-389 (2003).

[57] A. Fender, E. J. Rigg, R. R. Maier, W. N. MacPherson, J. S. Barton, A. J. Moore, J. D. Jones, D. Zhao, L. Zhang, I. Bennion, S. McCulloch, and B. J. Jones, "Dynamic two-axis curvature measurement using multicore fiber Bragg gratings interrogated by arrayed waveguide gratings," Applied Optics **45**, 9041-9048 (2006).

[58] A. Fender, W. N. MacPherson, R. R. J. Maier, J. S. Barton, D. S. George, R. I. Howden, G. W. Smith, B. J. S. Jones, S. McCulloch, X. Chen, R. Suo, L. Zhang, and I. Bennion, "Two-axis temperature-insensitive accelerometer based on multicore fiber Bragg gratings," IEEE Sensors Journal **8**, 1292-1298 (2008).

[59] W. N. MacPherson, G. M. H. Flockhart, R. R. J. Maier, J. S. Barton, J. D. C. Jones, D. Zhao, L. Zhang, and I. Bennion, "Pitch and roll sensing using fibre Bragg gratings in multicore fibre," Measurement Science and Technology **15**, 1642-1646 (2004).

[60] W. N. MacPherson, M. Silva-Lopez, J. S. Barton, A. Moore, J. Jones, D. Zhao, L. Zhang, I. Bennion, N. Metje, and D. Chapman, "Tunnel monitoring using multicore fibre displacement sensor," Measurement Science and Technology **17**, 1180 (2006).

[61] D. Barrera, I. Gasulla, and S. Sales, "Multipoint two-dimensional curvature optical fiber sensor based on a nontwisted homogeneous four-core fiber," Journal of Lightwave Technology **33**, 2445-2450 (2015).

[62] H. Zhang, Z. Wu, P. P. Shum, R. Wang, X. Q. Dinh, S. Fu, W. Tong, and M. Tang, "Fiber Bragg gratings in heterogeneous multicore fiber for directional bending sensing," Journal of Optics **18**, 085705 (2016).

[63] M. Hou, K. Yang, J. He, X. Xu, S. Ju, K. Guo, and Y. Wang, "Two-dimensional vector bending sensor based on seven-core fiber Bragg gratings," Optics Express **26**, 23770-23781 (2018).

[64] R. G. Duncan, M. E. Froggatt, S. T. Kreger, R. J. Seeley, D. K. Gifford, A. K. Sang, and M. S. Wolfe, "High-accuracy fiber-optic shape sensing," in Sensor Systems and Networks: Phenomena, Technology, and Applications for NDE and Health Monitoring. International Society for Optics and Photonics, 2007.

[65] J. P. Moore, and M. D. Rogge, "Shape sensing using multi-core fiber optic cable and parametric curve solutions," Optics Express **20**, 2967-2973 (2012).

[66] C. R. S, and E. D. P, "FBG-based shape sensing tubes for continuum robots," in *2014 IEEE International Conference on Robotics and Automation (ICRA)*(2014), pp. 3531-3537.

[67] P. S. Westbrook, K. S. Feder, T. Kremp, T. F. Taunay, E. Monberg, J. Kelliher, R. Ortiz, K. Bradley, K. S. Abedin, D. Au, and G. Puc, "Integrated optical fiber shape sensor modules based on twisted multicore fiber grating arrays," (SPIE2014), pp. 89380H-89380H-89387.

[68] P. S. Westbrook, T. Kremp, K. S. Feder, W. Ko, E. M. Monberg, H. Wu, D. A. Simoff, T. F. Taunay, and R. M. Ortiz, "Continuous multicore optical fiber grating arrays for distributed sensing applications," Journal of Lightwave Technology **35**, 1248-1252 (2017).

[69] F. Khan, A. Denasi, D. Barrera, J. Madrigal, S. Sales, and S. Misra, "Multi-core optical fibers with Bragg gratings as shape sensor for flexible medical instruments," IEEE Sensors Journal **19**, 5878-5884 (2019).

[70] Z. Zhao, M. A. Soto, M. Tang, and L. Thévenaz, "Distributed shape sensing using Brillouin scattering in multi-core fibers," Optics Express **24**, 25211 (2016).

[71] A. Zafeiropoulou, A. Masoudi, L. Cooper, and G. Brambilla, "Distributed shape sensing with a multicore fibre based on BOTDR technique," in *Optical Fiber Sensors* (Optical Society of America2018), p. ThE15.

[72] Ł. Szostkiewicz, M. A. Soto, Z. Yang, A. Dominguez-Lopez, I. Parola, K.

Markiewicz, A. Pytel, A. Kołakowska, M. Napierała, T. Nasiłowski, and L. Thevenaz, "High-resolution distributed shape sensing using phase-sensitive optical time-domain reflectometry and multicore fibers," Optics Express **27**, 20763 (2019).

[73] P. J. Lemaire, R. Atkins, V. Mizrahi, and W. Reed, "High pressure $H_2$ loading as a technique for achieving ultrahigh UV photosensitivity and thermal sensitivity in $GeO_2$ doped optical fibres," Electronics Letters **29**, 1191-1193 (1993).

[74] D. Williams, B. Ainslie, J. Armitage, R. Kashyap, and R. Campbell, "Enhanced UV photosensitivity in boron codoped germanosilicate fibres," Electronics Letters **29**, 45-47 (1993).

[75] E. Dianov, K. Golant, V. Mashinskv, O. Medvedkov, I. Nikolin, O. Sazhin, and S. Vasiliev, "Highly photosensitive nitrogen-doped germanosilicate fibre for index grating writing," Electronics Letters **33**, 1334-1336 (1997).

[76] X.-C. Long, and S. Brueck, "Composition dependence of the photoinduced refractive-index change in lead silicate glasses," Optics Letters **24**, 1136-1138 (1999).

[77] Y. Wang, L. Phillips, C. Yelleswarapu, T. George, A. Sharma, S. Burgett, and P. Ruffin, "Enhanced growth rate for Bragg grating formation in optical fibers with titania-doped outer cladding," Optics Communications **163**, 185-188 (1999).

[78] F. Bilodeau, B. Malo, J. Albert, D. C. Johnson, K. O. Hill, Y. Hibino, M. Abe, and M. Kawachi, "Photosensitization of optical fiber and silica-on-silicon/silica waveguides," Optics Letters **18**, 953-955 (1993).

[79] A. Donko, M. Beresna, Y. Jung, J. Hayes, D. J. Richardson, and G. Brambilla, "Point-by-point femtosecond laser micro-processing of independent core-specific fiber Bragg gratings in a multi-core fiber," Optics Express **26**,

2039 (2018).

[80] R. R. Gattass, and E. Mazur, "Femtosecond laser micromachining in transparent materials," Nature Photonics **2**, 219-225 (2008).

[81] G. D. Marshall, R. J. Williams, N. Jovanovic, M. J. Steel, and M. J. Withford, "Point-by-point written fiber-Bragg gratings and their application in complex grating designs," Optics Express **18**, 19844-19859 (2010).

[82] Z. Liu, Z. F. Zhang, H.-Y. Tam, and X. Tao, "Multifunctional smart optical fibers: materials, fabrication, and sensing applications," Photonics **6**, 48 (2019).

[83] A. Martinez, I. Y. Khrushchev, and I. Bennion, "Thermal properties of fibre Bragg gratings inscribed point-by-point by infrared femtosecond laser," Electronics Letters **41**, 176-178 (2005).

[84] B. H. Kim, T.-J. Ahn, D. Y. Kim, B. H. Lee, Y. Chung, U.-C. Paek, and W.-T. Han, "Effect of $CO_2$ laser irradiation on the refractive-index change in optical fibers," Applied Optics **41**, 3809-3815 (2002).

[85] I.-L. Bundalo, K. Nielsen, C. Markos, and O. Bang, "Bragg grating writing in PMMA microstructured polymer optical fibers in less than 7 minutes," Optics Express **22**, 5270-5276 (2014).

[86] X. Cheng, D. S. Gunawardena, C.-F. J. Pun, J. Bonefacino, and H.-Y. Tam, "Single nanosecond-pulse production of polymeric fiber Bragg gratings for biomedical applications," Optics Express **28**, 33573-33583 (2020).

[87] Y. Qiu, Y. Sheng, and C. Beaulieu, "Optimal phase mask for fiber Bragg grating fabrication," Journal of Lightwave Technology **17**, 2366 (1999).

[88] Y. Lai, K. Zhou, K. Sugden, and I. Bennion, "Point-by-point inscription of first-order fiber Bragg grating for C-band applications," Optics Express **15**, 18318-18325 (2007).

[89] T. Erdogan, "Fiber grating spectra," Journal of Lightwave Technology **15**, 1277-1294 (1997).

[90] K. O. Hill, and G. Meltz, "Fiber Bragg grating technology fundamentals and overview," Journal of Lightwave Technology **15**, 1263-1276 (1997).

[91] A. D. Kersey, M. A. Davis, H. J. Patrick, M. LeBlanc, K. P. Koo, C. G. Askins, M. A. Putnam, and E. J. Friebele, "Fiber grating sensors," Journal of Lightwave Technology **15**, 1442-1463 (1997).

[92] S.-s. Min, C. Trinh, S. Leon-Saval, N. Jovanovic, P. Gillingham, J. Bland-Hawthorn, J. Lawrence, T. A. Birks, M. M. Roth, and R. Haynes, "Multicore fibre Bragg grating developments for OH suppression," in *Modern Technologies in Space-and Ground-based Telescopes and Instrumentation II*(International Society for Optics and Photonics2012), p. 84503L.

[93] E. Lindley, S.-S. Min, S. Leon-Saval, N. Cvetojevic, N. Jovanovic, J. Bland-Hawthorn, J. Lawrence, I. Gris-Sanchez, T. Birks, and R. Haynes, "Core-to-core uniformity improvement in multi-core fiber Bragg gratings," in *Advances in Optical and Mechanical Technologies for Telescopes and Instrumentation*(International Society for Optics and Photonics2014), p. 91515F.

[94] E. Lindley, S.-S. Min, S. Leon-Saval, N. Cvetojevic, J. Lawrence, S. Ellis, and J. Bland-Hawthorn, "Demonstration of uniform multicore fiber Bragg gratings," Optics Express **22**, 31575-31581 (2014).

[95] R. Idrisov, M. Becker, M. Rothhardt, J. Bierlich, and H. Bartelt, "Optimisation of fibre Bragg gratings inscription in multicore fibres," in *Optical Fiber Sensors*(Optical Society of America2018), p. WF64.

[96] R. Idrisov, M. Rothhardt, and H. Bartelt, "In-plane wavelength multiplexing of fibre Bragg gratings in a multicore optical fibre," in *Fourth International Conference on Applications of Optics and Photonics*(International Society for Optics and Photonics2019), p. 112072O.

[97] T. Hayashi, T. Taru, O. Shimakawa, T. Sasaki, and E. Sasaoka, "Design and

fabrication of ultra-low crosstalk and low-loss multi-core fiber," Optics Express **19**, 16576-16592 (2011).

[98] V. A. Toponogov, *Differential geometry of curves and surfaces* (Springer, 2006).

[99] A. Bertolini, R. DeSalvo, F. Fidecaro, M. Francesconi, S. Marka, V. Sannibale, D. Simonetti, A. Takamori, and H. Tariq, "Mechanical design of a single-axis monolithic accelerometer for advanced seismic attenuation systems," Nuclear Instruments and Methods in Physics Research Section A: Accelerators, Spectrometers, Detectors and Associated Equipment **556**, 616-623 (2006).

[100] C.-W. Tan, and S. Park, "Design of accelerometer-based inertial navigation systems," IEEE Transactions on Instrumentation and Measurement **54**, 2520-2530 (2005).

[101] J. W. Borinski, C. D. Boyd, J. A. Dietz, J. C. Duke, and M. R. Home, "Fiber optic sensors for predictive health monitoring," in *2001 IEEE Autotestcon Proceedings. IEEE Systems Readiness Technology Conference.(Cat. No. 01CH37237)*(IEEE2001), pp. 250-262.

[102] X. Wang, Y. Guo, L. Xiong, and H. Wu, "High-frequency optical fiber Bragg grating accelerometer," IEEE Sensors Journal **18**, 4954-4960 (2018).

[103] C. Fu, W. Zhu, W. Deng, F. Xu, N. Wang, L. Zou, and F. Xue, "Measuring the orientation of the flexural vibrations of a cantilevered microwire with a micro-lens fiber-optic interferometer," Applied Physics Letters **113**, 243101 (2018).

[104] W. Bao, X. Qiao, and Q. Rong, "Fiber-optic vector accelerometer using orthogonal Bragg grating inscription over innermost cladding of a multi-clad fiber," Journal of Lightwave Technology **37**, 2706-2712 (2018).

[105] G. A. Cranch, and P. J. Nash, "High-responsivity fiber-optic flexural disk accelerometers," Journal of Lightwave Technology **18**, 1233 (2000).

[106] J. Villatoro, E. Antonio-Lopez, J. Zubia, A. Schülzgen, and R. Amezcua-Correa, "Interferometer based on strongly coupled multi-core optical fiber for accurate vibration sensing," Optics Express **25**, 25734-25740 (2017).

[107] Q. Rong, T. Guo, W. Bao, Z. Shao, G.-D. Peng, and X. Qiao, "Highly sensitive fiber-optic accelerometer by grating inscription in specific core dip fiber," Scientific Reports **7**, 1-9 (2017).

[108] J. Li, G. Wang, J. Sun, R. R. J. Maier, W. Macpherson, D. P. Hand, and F. Dong, "Micro-machined optical fiber side-cantilevers for acceleration measurement," IEEE Photonics Technology Letters **29**, 1836-1839 (2017).

[109] R. P. Linessio, K. de Morais Sousa, T. da Silva, C. A. Bavastri, P. F. da Costa Antunes, and J. C. C. da Silva, "Induction motors vibration monitoring using a biaxial optical fiber accelerometer," IEEE Sensors Journal **16**, 8075-8082 (2016).

[110] Q. Rong, X. Qiao, T. Guo, W. Bao, D. Su, and H. Yang, "Orientation-dependent fiber-optic accelerometer based on grating inscription over fiber cladding," Optics Letters **39**, 6616-6619 (2014).

[111] X. Dong, L. Hu, L. Shao, Y. Wang, and J. Zheng, "Temperature‐insensitive 2D fiber Bragg grating tilt sensor," Microwave and Optical Technology Letters **55**, 344-346 (2013).

[112] M. Maheshwari, Y. Yang, D. Upadrashta, and T. Chaturvedi, "A rotation independent in-place inclinometer/tilt sensor based on fiber Bragg grating," IEEE Transactions on Instrumentation and Measurement, **68**, 2943-2953 (2018).

[113] H. Xu, F. Li, W. Zhao, S. Wang, Y. Du, and C. Bian, "A high precision fiber Bragg grating inclination sensor for slope monitoring," Journal of Sensors **2019** (2019).

[114] F. Acernese, R. Canonico, R. De Rosa, G. Giordano, R. Romano, and F. Barone,

"Mechanical monolithic tiltmeter for low frequency measurements," in *Sensors and Smart Structures Technologies for Civil, Mechanical, and Aerospace Systems 2013* (International Society for Optics and Photonics2013), p. 86923J.

[115] Y. C. Choi, J. C. Choi, and S. H. Kong, "A MEMS tilt sensor with expanded operating range and improved sensitivity," Japanese Journal of Applied Physics **53**, 06JM12 (2014).

[116] L. Rovati, and S. Cattini, "Contactless two-axis inclination measurement system using planar flux-gate sensor," IEEE Transactions on Instrumentation and Measurement **59**, 1284-1293 (2010).

[117] H.-J. Chen, L. Wang, and W. F. Liu, "Temperature-insensitive fiber Bragg grating tilt sensor," Applied Optics **47**, 556-560 (2008).

[118] B.-O. Guan, H.-Y. Tam, and S.-Y. Liu, "Temperature-independent fiber Bragg grating tilt sensor," IEEE Photonics Technology Letters **16**, 224-226 (2004).

[119] G. A. Miller, C. G. Askins, and G. A. Cranch, "Interferometric interrogation of a multicore fiber, two-axis inclinometer," in *20th International Conference on Optical Fibre Sensors*(International Society for Optics and Photonics2009), p. 75032R.

[120] J.-S. Chiang, H.-Y. Chang, N.-H. Sun, and W.-F. Liu, "High sensitive two-dimension tilted-meter based on chirped fiber Bragg gratings," IEEE Sensors Journal **16**, 8477-8482 (2016).

[121] R. T. Fenner, and J. N. Reddy, *Mechanics of solids and structures* (CRC Press, 2012).

[122] H.-F. Pei, J. Teng, J.-H. Yin, and R. Chen, "A review of previous studies on the applications of optical fiber sensors in geotechnical health monitoring," Measurement **58**, 207-214 (2014).

[123] H. A. Rahman, S. W. Harun, M. Yasin, and H. Ahmad, "Fiber-optic salinity sensor using fiber-optic displacement measurement with flat and concave

mirror," IEEE Journal of Selected Topics in Quantum Electronics **18**, 1529-1533 (2012).

[124] M. Nicolas, R. Sullivan, and W. Richards, "Large scale applications using FBG sensors: Determination of in-flight loads and shape of a composite aircraft wing," Aerospace **3** (2016).

[125] H. Xie, H. Liu, Y. Noh, J. Li, S. Wang, and K. Althoefer, "A fiber-optics-based body contact sensor for a flexible manipulator," IEEE Sensors Journal **15**, 3543-3550 (2015).

[126] X. Dong, X. Yang, C.-L. Zhao, L. Ding, P. Shum, and N. Q. Ngo, "A novel temperature-insensitive fiber Bragg grating sensor for displacement measurement," Smart Materials and Structures **14**, N7-N10 (2005).

[127] Q. Rong, X. Qiao, J. Zhang, R. Wang, M. Hu, and Z. Feng, "Simultaneous measurement for displacement and temperature using fiber Bragg grating cladding mode based on core diameter mismatch," Journal of Lightwave Technology **30**, 1645-1650 (2012).

[128] K. Chen, M. Guo, Y. Yang, K. Liu, W. Cai, and Q. Yu, "A fiber-optic displacement sensor based on high-precision differential phase measurement," Journal of Lightwave Technology **36**, 4046-4050 (2018).

[129] T. Yang, X. Qiao, Q. Rong, and W. Bao, "Orientation-dependent displacement sensor using an inner cladding fiber Bragg grating," Sensors (Basel) **16** (2016).

[130] H. Wu, L. Wang, N. Guo, C. Shu, and C. Lu, "Brillouin optical time-domain analyzer assisted by support vector machine for ultrafast temperature extraction," Journal of Lightwave Technology **35**, 4159-4167 (2017).

[131] A. K. Azad, F. N. Khan, W. H. Alarashi, N. Guo, A. P. T. Lau, and C. Lu, "Temperature extraction in Brillouin optical time-domain analysis sensors using principal component analysis based pattern recognition," Optics Express **25**, 16534-16549 (2017).

[132] A. K. Azad, L. Wang, N. Guo, H.-Y. Tam, and C. Lu, "Signal processing using artificial neural network for BOTDA sensor system," Optics Express **24**, 6769-6782 (2016).

[133] Y. Chang, H. Wu, C. Zhao, L. Shen, S. Fu, and M. Tang, "Distributed Brillouin frequency shift extraction via a convolutional neural network," Photonics Research **8**, 690-697 (2020).

[134] M. S. Djurhuus, S. Werzinger, B. Schmauss, A. T. Clausen, and D. Zibar, "Machine learning assisted fiber Bragg gating-based temperature sensing," IEEE Photonics Technology Letters **31**, 939-942 (2019).

[135] L. Massari, E. Schena, C. Massaroni, P. Saccomandi, A. Menciassi, E. Sinibaldi, and C. M. Oddo, "A machine-learning-based approach to solve both contact location and force in soft material tactile sensors," Soft Robotics **7**, 409-420 (2020).

[136] F. Barino, F. Delgado, M. A. Jucá, T. V. Coelho, and A. B. dos Santos, "Comparison of regression methods for transverse load sensor based on optical fiber long-period grating," Measurement **146**, 728-735 (2019).

[137] X. Zhou, X. Zhu, Z. Dong, and W. Guo, "Estimation of biomass in wheat using random forest regression algorithm and remote sensing data," The Crop Journal **4**, 212-219 (2016).

[138] J. Cui, Z. Liu, D. S. Gunawardena, Z. Zhao, and H.-Y. Tam, "Two-dimensional vector accelerometer based on Bragg gratings inscribed in a multi-core fiber," Optics Express **27**, 20848-20856 (2019).

[139] X. Dong, Y. Liu, Z. Liu, and X. Dong, "Simultaneous displacement and temperature measurement with cantilever-based fiber Bragg grating sensor," Optics Communications **192**, 213-217 (2001).

[140] J. Gere, *Mechanics of Materials* (Cengage Learning, 2003).

[141] L. Breiman, "Random Forests," Machine Learning **45**, 5-32 (2001).

[142] M. Kuhn, and K. Johnson, *Applied predictive modeling* (Springer, 2013).

[143] A. Liaw, and M. Wiener, "Classification and regression by randomForest," R News **2**, 18-22 (2002).

[144] N. Altman, and M. Krzywinski, "Points of Significance: Ensemble methods: bagging and random forests," (Nature Publishing Group, 2017).

[145] L. Breiman, "Bagging predictors," Machine Learning **24**, 123-140 (1996).